Fall 10-1-2021

Pairwise hydrodynamic interactions of permeable particles and flow-induced structuring in dilute suspensions

Rodrigo Bento Reboucas
Yale University Graduate School of Arts and Sciences, rodrigobentoo@gmail.com

Abstract

Pairwise Hydrodynamic Interactions of Permeable Particles and Flow-Induced Structuring in Dilute Suspensions

Rodrigo Bento Reboucas

2021

The study of particle-level interactions in suspension flows enables a better understanding and control of systems where suspensions play a key role. Examples include the physiology of blood flow microcirculation, flow-induced segregation of polydisperse suspensions, particle aggregation in marine environments, and filtration processes, to name a few. In these systems, a detailed description of the hydrodynamic interactions between the particles and between the particles and fluid boundaries characterize the evolution of the suspension microstructure. Typically, the characteristic size of the particles is small compared to the imposed flow length scale, and hence low-Reynolds-number conditions usually apply. In the dilute regime, pair-interactions between smooth, rigid and spherical particles yield symmetric particle trajectories with zero net cross-flow displacements and thus no structuring. However, short-range phenomena including material specific forces, e.g., electrostatic repulsion and van der Waals attraction, and physical properties of the particles, e.g., particle permeability, surface roughness, and interface mobility, break the symmetry of particle trajectories resulting in net particle displacements and hence particle structuring.

This thesis contains a detailed analysis of the near-contact motion of permeable particles in the limit of weak surface permeability where Darcy's law is used to describe the flow in the permeable medium. A full set of resistance and mobility functions that relates particle motion to forces, torques, and stresslets acting on the particles are calculated. Results show that non-zero values of particle permeability qualitatively alter the near-contact particle motion, removing the classical lubrication

resistance between approaching smooth impermeable spheres that prevents particle contact under the action of a finite force without the need for nonhydrodynamic interparticle forces (van der Waals attraction). Particle permeability also qualitatively alters the tangential motion of particles, providing access to non-singular rolling motion of particles along walls. This analysis may help to predict the capacity for crossflow filtration devices. Analytical closed-form expressions are derived for binary collision rates for permeable particles in Brownian motion, gravity sedimentation, uniaxial straining, and shear flow. Here, the solution of the analogous problem of binary collision rates of particles with small-amplitude surface roughness provide accurate approximations for the collision rates of permeable particles for all aggregation mechanisms considered herein. Finally, a pairwise hydrodynamic theory is presented for flow-induced particle distributions in dilute polydisperse suspensions. Diffusive fluxes and a drift velocity in non-homogeneous shear flows are obtained from a Boltzmann-like master equation. A boundary-layer analysis in regions of vanishing shear rates (e.g., centerline of a channel flow) overcomes the failure of the current theories that predict aphysical singular behavior. The analysis presented herein yields non-singular particle distributions that qualitatively resemble experimental results in the literature. Results for bidisperse suspensions show that size segregation occurs in Poiseuille flow leading to relative enrichment of larger or smaller species at the centerline, depending on the size ratio, relative number densities, and physical properties of the particles.

Pairwise Hydrodynamic Interactions of Permeable Particles and Flow-Induced Structuring in Dilute Suspensions

A Dissertation
Presented to the Faculty of the Graduate School
of
Yale University
in Candidacy for the Degree of
Doctor of Philosophy

By
Rodrigo Bento Reboucas

Dissertation Director: Michael Loewenberg

December 2021

Contents

Acknowledgements

My journey as a graduate student at Yale was full of great memories, friendship, hard work, and joy. I am extremely grateful for all those people who took part of this amazing experience. First, I would to thank my graduate advisor, Prof. Loewenberg, for all the support, constant help, patience, and care for the past five years. I have a very vivid and fond memory of the day I met him for the first time, when, after a few minutes of casual chat, he was at the chalk board writing some scaling analysis about particle interactions; I'm very glad that this routine has not changed ever since! Thank you very much for teaching me how to become a better researcher and for showing me the "art" of careful mathematical analysis. I enjoyed working with you very much and thank you for encouraging me to pursue a career in academia. I hope I can continue learning from you in the years to come. Also, thank you for the delicious sourdough breads that gave me the extra energy needed in final stages of my PhD!

I would like to thank my thesis Committee members, Prof. de la Mora and Prof. Haji-Akbari for inspiring discussions on fluid mechanics during regular committee meetings, graduate classes, and informal corridor conversations. It was a great pleasure to interact with you. I'm grateful to Dr. A. Z. Zinchenko for the use of his bispherical coordinate code for computing pair mobilities of hard spheres, and to Prof. Miksis for accepting the invitation to be the external reader of this thesis. I also would like to thank my master's advisor, Prof. Marcio Carvalho, and under-

graduate advisor, Prof. Taygoara Oliveira, for leading me with skillful hands into the realm of research. Special thanks to Prof. Oliveira who inspired me to pursue a career in fluid dynamics! Looking into the future, I would like to thank Prof. Vlahovska for taking me as a postdoctoral researcher in her research group. I'm grateful that my academic trajectory has crossed paths with such great minds along the way, including amazing colleagues, friends and many Professors who helped shape my perception of rigorous academic research. I would like to thank my colleague and friend, Ivan Rosa de Siqueira, for many productive years working together; for great discussions on fluid mechanics and for setting the pace of high-level engagement in research since our early undergraduate days at the University of Brasilia.

I would like to thank all my friends and colleagues from Yale who contributed to an amazing graduate life experience. Special thanks to Ming and Luisja for our weekly coffee breaks - I will miss that! My lab mates: Joe, Rostacia, and Fernanda for fruitful discussions about research. Thanks to Sebastian and Aya for our many lunch hours together! And thanks to Sarwar, Marko, Tom, Nikita, Jorge, and all other friends, colleagues and staff members from the School of Engineering and Applied Science. Thank you Cara Gibilisco, Ben McManus, and Ellen Lelasher for all the help with administrative tasks.

I would like thank my dear friends and family members from Brazil who I miss very much. Especially, my mother-in-law for all her support and care; and my cousin, Rafael, who encouraged me to apply for a PhD in the US and for a lifetime of friendship! Most importantly, I would like to thank my beloved parents and sister for being my save haven, for all the love and care during my entire life! It is impossible to put into words how grateful and lucky I am to have you in my life. Special acknowledgement to my sister and her boyfriend who are expecting a baby soon - can't wait to meet you in person, Levi! Finally, a huge thanks to the person who carries many roles including, but not limited to, being my wife, my best friend, my

partner, and the love of my life. Thank you for all your love and support!

I'm grateful for the financial support from the National Science Foundation CBET grant no. 1603806 and from the Coordenação de Aperfeiçoamento de Pessoal de Nível Superior - Brasil (Capes) - Finance code 001.

List of Figures

List of Tables

Chapter 1

Introduction

Particle suspensions are present in a broad range of natural phenomena and constitute an essential part of industrial applications. Examples encompass blood flow in the microcirculation [1], sensation of food and digestion [2, 3], flow-induced demixing in polydisperse suspensions [4, 5], particle filtration processes [6], and particle aggregation in wastewater treatment [7,8] and in marine environments [9]. Understanding the role of suspensions in these systems require knowledge of the hydrodynamic interactions between the particles and between the particles and fluid boundaries. Typically, particles are suspended in a fluid subjected to an imposed flow and the physical properties of the particles characterize the evolution of the suspension microstructure.

In general, the characteristic size of the suspended particles is small compared to the imposed flow length scale, and hence low-Reynolds-number conditions usually apply. Highly-ordered particle structure is verified in non-colloidal suspensions where Brownian motion is negligible. Under dilute conditions, particle pair-interactions are uncorrelated on the particle scale yielding symmetric (time-reversible) trajectories for smooth, impermeable, and rigid spheres. This is a consequence of the linearity of the Stokes equations leading to zero cross-flow net displacements of the particles including the limit of vanishing separations between their surfaces. In this limit, classical

lubrication resistance hinders particle relative motion preventing contact configurations under the action of a finite force. Short-range phenomena including material specific forces, e.g., electrostatic repulsion and van der Waals attraction, and physical phenomena, e.g., small amplitude surface asperities, weak surface permeability, and interface mobility, break the symmetry of particle trajectories yielding non-zero net particle displacements. Herein, we assume cross-flow net displacements of particles as the dominant mechanism for particle transport and hence flow-induced structuring.

In order to calculate particle transport and study the stability of particle suspensions, knowledge of particle motion is key. Under Stokes regime, particle motion is fully specified by a linear relation between forces, torques, and stresslets acting on the particles and their respective velocities and rates of strain (for deformable particles). This relationship is defined by mobility functions when moments on the particles are specified, or by resistance functions when particle velocities are known. Those functions depend on particle geometry, particle physical properties, and interparticle separation [10]. Due to the radial symmetry of spherical particles, resistance and mobility functions can be analyzed in two modes of interactions: axisymmetric motion along the line-of-centers and asymmetric motion perpendicular to the line-of-centers. Analytical and numerical schemes for calculating these functions are available in the specialized literature [11]. For a given pair interaction, integration of particle velocities yields deterministic particle trajectories as quadratures of mobility functions.

In this thesis, we study dilute suspensions of spherical particles with short-range symmetry-breaking mechanisms that lead to particle structuring. Examples include permeable particles with weak surface permeability, rough particles with small surface asperities, and clean high-surface-tension drops. Typically, a boundary-layer problem is set by a separation of characteristic length scales in two regions: (i) inner region where particle surface phenomena qualitatively alters the near-contact motion of the particles, and (ii) outer flow region where a classical description of smooth, rigid

spheres applies.

Chapters 2 and 3 present a complete set of resistance and mobility functions for the near-contact motion of permeable particles in the asymptotic limit of weak permeability. The permeable medium is treated as a semi-infinite domain where Darcy's law is used to describe fluid flow. Lubrication analyses for the axisymmetric problem (Chapter 2) and asymmetric problem (Chapter 3) yield non-local integral equations for the radial pressure distribution in the gap between the particles. In both problems, non-zero particle permeability qualitatively alters the near-contact motion, removing the classical singular lubrication force and resulting in particle contact in finite times under the action of a finite force. In Chapter 2, the formulation allows for particles with distinct particle radii, permeabilities, and slip coefficients, including permeable and impermeable particles and spherical drops. In Chapter 3, we show that permeability additively affects the transverse lubrication resistances and that a particle in contact with a permeable half-space rolls without slipping under the action of a tangential constant force; particles in contact with an impermeable half-space roll with slipping under the same conditions.

In Chapter 4, binary collision rates are calculated for permeable particles undergoing (i) Brownian motion, (ii) gravity sedimentation, (iii) uniaxial straining flow and (iv) shear flow. Darcy's law is used to describe the flow inside the permeable particles and no-slip boundary conditions are applied at particle surfaces. A leading-order asymptotic solution of the problem is developed for the weak permeability regime. The resulting collision rates are given by quadrature of the pair mobility functions for permeable particles in the near-contact lubrication region and size-ratio-dependent parameters obtained from standard hard-sphere pair mobility functions. Collision rates in shear flow vanish below a critical permeability value that increases with diminishing size ratio. The analogous problem of pair collision rates of particles with small-amplitude surface roughness is also analyzed. We show that the formulas for the

collision rates of rough particles provide accurate analytical approximations for the collision rates of permeable particles for all four aggregation mechanisms considered.

In Chapter 5, we develop a pairwise hydrodynamic theory for flow-induced particle distributions in polydisperse suspensions in flows of the form $\mathbf{v} = v(y)\mathbf{e}_x$, including simple shear and planar Poiseuille flow. Coupled diffusive fluxes and a drift velocity are extracted from a Boltzmann-like master equation. A boundary layer is shown to form in regions where the shear rate vanishes and the thickness is set by the radius of the upstream collision cross-section for pair interactions. An analysis of this region yields a linearly vanishing drift velocity and non-vanishing diffusivities at the point where the shear rate vanishes thus circumventing the source of the singular particle distribution predicted by the usual diffusive flux model. Outside of the boundary layer, the stationary particle distribution has a universal power-law form. Trajectories for particles with symmetry-breaking contact interactions (e.g., rough particles, emulsion drops, permeable particles) are analytically integrated to yield particle displacements in terms of quadratures of mobility functions for spherical particles. This analytical displacement results are used in the calculation of particle distributions in planar Poiseuille flows. Our results illustrate the nonsingular particle distributions that result from the boundary layer analysis. Results for bidisperse suspensions show that relative enrichment of larger or smaller species is possible, depending on the size ratio, relative number densities, and the physical properties of the particles.

The introduction of each chapter presents a detailed literature review of each topic studied herein.

Chapter 2

Near-contact approach of two permeable spheres

2.1 Introduction

Interest in the hydrodynamics of particles with permeable media is motivated by particle filtration processes, where suspended particles interact with a porous filter or frit or with a porous cake of captured particles [12–14]. Permeable particles formed by flocculation of smaller particles and drops arise in applications such as waste water treatment [7, 8]. In other applications, permeable particles are used to enhance mass transport in packed bed [15] and fluidized catalytic reactors [16], and in chromatography columns [17,18]. The design and construction of equipment for these applications requires an understanding of the hydrodynamic interactions of suspended permeable particles.

Fluid flow in a homogeneous, permeable material is usually described using Darcy's law [19]. According to Darcy's law, the fluid velocity is proportional to the pressure gradient with proportionality k/μ, where μ is the viscosity of the fluid, and k is the permeability of the material that typically scales with the square of the pore size.

Darcy's law is appropriate when the length scale set by velocity gradients is much larger than the pore-scale. Typically, this situation is realized in materials with a high solid-phase volume fraction, e.g., flow through a packing of solid particles where the pore-scale is set by the particle size. Brinkman's equation, by contrast, is an appropriate description for permeable materials with very dilute solid networks where the pore scale tends to set the length scale of velocity gradients [20–22]. An example of the latter is flow through a dilute fibrous packing where the pore scale, and scale of velocity gradients, are set by the distance between fibers, not their diameter.

Early works that relied on Darcy's law assumed that no-slip boundary conditions apply at the interface between the permeable material and the free fluid region [23, 24]. There have been several investigations of the appropriate boundary conditions at this interface [25–30]. No-slip and slip-velocity boundary conditions are most frequently used. According to the slip-velocity boundary condition proposed by Beavers & Joseph [25] and by Saffman [26], the tangential velocity on the boundary of a permeable material is proportional to the tangential stress.

A significant amount of work has focused on analyses of suspended spherical particles moving toward thin, permeable layers as a model for particle capture in filtration [31–36]. In these studies, it was assumed that the fluid velocity normal to the permeable layer is proportional to the local pressure difference across the layer with proportionality k'/μ, where k' is the permeance, a characteristic property of the layer. Radial flow within the permeable layer was neglected. An important finding in the foregoing studies is that permeable boundaries provide a cut-off for the lubrication resistance allowing contact under the action of a finite force. This is in contrast to the case for impermeable boundaries where contact is prevented by the singular lubrication resistance.

Hydrodynamic interactions between impermeable particles with permeable half-spaces [37, 38]; permeable particles and impermeable walls [39–41]; between two per-

meable particles [42–44]; and between permeable particles with impermeable cores [45, 46] have been studied. A few of these works used Brinkman's equation to describe the flow inside the permeable medium [39, 45, 46], the remainder used Darcy's law; comparisons show that similar results were obtained [45]. Several studies considered the axisymmetric near-contact motion of the particles. The results demonstrate non-singular lubrication resistance [37–39, 41], as seen for particles interacting with thin permeable layers discussed in the preceding paragraph. However, the bispherical-coordinate calculations and the collocation method used for these studies converge slowly for near-contact configurations and become singular at contact. Calculations using tangent-sphere coordinates can provide the contact force but are limited to zero gap width [37].

The lubrication analysis presented herein provides a bridge between prior studies by providing efficient calculations for the lubrication resistance of near-contact and contact configurations of permeable particles. The flow in the permeable medium is governed by Darcy's law; no-slip and slip-velocity boundary conditions are considered on the boundary of the permeable medium. The formulation allows for arbitrary ratios of particle radii, permeabilities, and slip coefficients. Accordingly, the analysis encompasses pairwise near-contact configurations of permeable and impermeable particles, and configurations of permeable particles with spherical drops. The zero-size-ratio limit describes the interactions of particles and drops with permeable half-spaces and fluid interfaces. Scaling arguments for the lubrication problem are presented in Section §2, and the governing equations are derived in §3. Section §4 contains analytical and numerical results. The lubrication resistance and contact force are compared with previous calculations in §5.

2.2 Lubrication Scaling

The scaling argument presented below for the lubrication flow between spherical particles explains the qualitative effect of particle permeability.

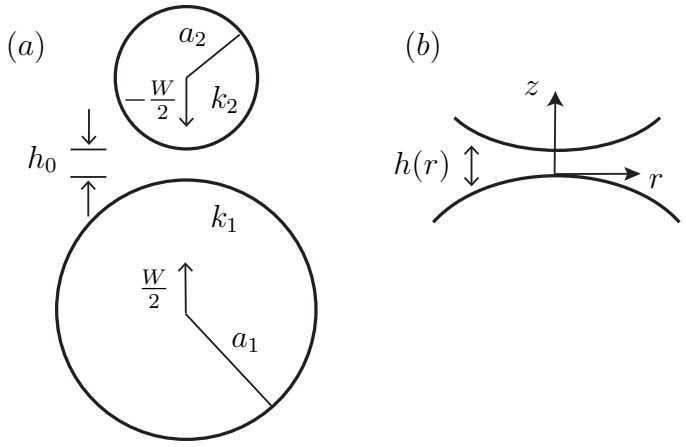

Figure 2.1: Schematic showing (a) two particles with radii and permeabilities a_i and k_i (i=1,2), respectively, with velocities $\pm\frac{1}{2}W$, and separated by a gap h_0; (b) profile of near-contact region between the particles showing cylindrical coordinate system.

Lubrication theory is used to describe the axisymmetric near-contact motion between two permeable spheres in a fluid with viscosity μ. A cylindrical coordinate system (r, z) is invoked with z-coordinate coinciding with the symmetry axis, and radial coordinate r is distance from the axis, as shown in figure 2.1. The spheres are separated by a gap h_0, and $W = -dh_0/dt$ is the magnitude of the relative velocity of the spheres.

The gap width h_0 sets the length scale for gradients of the fluid velocity in the z-direction, and W sets the scale for the magnitude of the fluid velocity in the z-direction. A distinct lateral length scale L describes variations of the fluid velocity in the radial direction,

$$a \gg L \gg h_0 \,. \tag{2.1}$$

Under this assumption, the radial velocity scale is WL/h_0 according to the continuity

equation, and, by the Navier-Stokes equations, the characteristic pressure in the gap is given by

$$p_c \sim \mu W a^3 L^{-4} \,. \tag{2.2}$$

Close to the symmetry axis, the profile of the gap between spherical particles is approximately parabolic,

$$h = h_0 + \frac{r^2}{2a} \,, \tag{2.3}$$

where a_1 and a_2 are the sphere radii, and a is the reduced radius ($a^{-1} = a_1^{-1} + a_2^{-1}$). This geometry suggests the lateral length scale

$$L_0 = (h_0 a)^{1/2} \,, \tag{2.4}$$

which lies in the range (2.1) required for lubrication theory and for the order of approximation of expansion (2.3), provided that $(h_0/a)^{1/2} \ll 1$. For impermeable spheres, the appropriate lateral lubrication length scale is L_0.

The time scale for the near-contact motion is

$$t_0 = \frac{h_0}{W} \,. \tag{2.5}$$

A second time scale enters the near-contact motion between permeable spheres given by $t_k = h_0/j$, where j is the magnitude of the flux according to Darcy's law, $j = k\nabla\hat{p}/\mu$, and $\nabla\hat{p}$ is the intraparticle pressure gradient. Inside the permeable particles, pressure variations are the same order of magnitude in the radial and axial directions, and by the continuity of the pressure across the particle surface, $\nabla\hat{p} \sim p_c/L$, where p_c is the characteristic pressure in the gap between the particles. Combining these estimates with the scaling (2.2) and taking $L = L_0$ for the lateral length scale, yields the second time scale,

$$t_k = t_0 K^{-1} \left(\frac{L_0}{a}\right)^5 \,. \tag{2.6}$$

Here, $K = k/a^2$ is the dimensionless permeability. This result can be re-written as

$$\frac{t_k}{t_0} = \left(\frac{L_0}{L_k}\right)^5 , \tag{2.7}$$

thereby defining a second lateral length scale,

$$L_k = aK^{1/5} . \tag{2.8}$$

Herein, small permeabilities,

$$K^{1/5} \ll 1 \tag{2.9}$$

are assumed so that L_k lies in the required range (2.1). (Moreover, L_k exceeds the pore scale, $aK^{1/2}$, as required for the use of Darcy's law.)

The ratio of the above time or length scales defines a parameter q that characterizes the near-contact motion of permeable spheres,

$$q = (t_k/t_0)^{2/5} = (L_0/L_k)^2 = \frac{h_0}{a} K^{-2/5} . \tag{2.10}$$

The shortest of the two time scales, and correspondingly the longest of the two length scales, controls the near-contact motion. For $q \gg 1$, near-contact motion results primarily by fluid flow from the gap between the particles; for $q \ll 1$, near-contact motion results primarily from fluid flow into the permeable particles. The cross-over between these regimes occurs for $q = O(1)$.

The last expression on the right side of Eq. (2.10), obtained by inserting Eqs. (2.4) and (2.8), indicates that the parameter q can be interpreted as a re-scaled gap width, i.e., h_0/a normalized by $K^{2/5}$. This interpretation indicates that particle permeability becomes important for $h_0/a < K^{2/5}$. Under the assumption of small permeabilities (2.9), this transition occurs within the lubrication regime.

Given that the force driving the near-contact motion is balanced by the pressure

in the lubrication region, $F \sim p_c L^2$, and using Eq. (2.2) yields

$$F \sim \mu W a^3 L^{-2}\,, \tag{2.11}$$

where $L = \max(L_0, L_k)$. Taking $L = L_0$ recovers the classical singular lubrication resistance that characterizes the near-contact motion of impermeable spheres,

$$F \sim \mu W a^2 h_0^{-1}\,, \tag{2.12}$$

and thus $W \sim F(\mu a)^{-1}(h_0/a)$, indicating that the gap decays exponentially in time under the action of a constant force but contact does not occur. Ultimately, however, when the gap between the particles diminishes so that $\max(L_0, L_k) = L_k$, the non-singular, gap-independent force is

$$F \sim \mu a W K^{-2/5}\,, \tag{2.13}$$

according to Eqs. (2.8) and (2.11). Here, $W \sim F(\mu a)^{-1} K^{2/5}$, indicating that the relative velocity between permeable spheres approaches a constant value under the action of a constant force and contact occurs in finite time.

2.3 Lubrication Formulation

Here, a lubrication formulation is presented for the near-contact motion of two permeable particles. The formulation accounts for the fluid flux j into the particles described by Darcy's law with the Beavers-Joseph boundary condition to account for the slip at the interface of a permeable medium. The particle size ratio is arbitrary; hence the limiting case of a particle approaching a half-space is recovered. As shown

below, it is convenient to define the mean permeability

$$k = \frac{1}{2}(k_1 + k_2) \tag{2.14}$$

to accommodate particles with distinct permeabilities. Accordingly, the dimensionless mean permeability is defined

$$K = k/a^2 \,. \tag{2.15}$$

Two sets of dimensionless lubrication variables are defined corresponding to the choice of characteristic length: (a) classical lubrication variables for impermeable spheres defined in terms of the length scale L_0,

$$\bar{r} = \frac{r}{L_0}\,, \qquad \bar{z} = \frac{za}{L_0^2}\,, \qquad \bar{v} = \frac{vL_0}{Wa}\,, \qquad \bar{w} = \frac{w}{W}\,, \qquad \bar{p} = \frac{pL_0^4}{\mu W a^3}\,, \qquad \bar{j} = \frac{j}{W}q^{5/2}\,, \tag{2.16}$$

and (b) permeable-sphere lubrication variables defined in terms of the length scale L_k,

$$\tilde{r} = \frac{r}{L_k}\,, \qquad \tilde{z} = \frac{za}{L_k^2}\,, \qquad \tilde{v} = \frac{vL_k}{Wa}\,, \qquad \tilde{w} = \frac{w}{W}\,, \qquad \tilde{p} = \frac{pL_k^4}{\mu W a^3}\,, \qquad \tilde{j} = \frac{j}{W}\,. \tag{2.17}$$

Here, (r, z) is the cylindrical coordinate system defined in figure 2.1; v and w are the corresponding radial and axial components of the fluid velocity in the lubrication region. The dimensionless axial velocity is unaffected by the characteristic length because it is nondimensionalized by relative velocity of the particles, W. The parameter q is defined by Eq. (2.10). The dimensionless intraparticle flux $\bar{j}$ or $\tilde{j}$ in Eqs. (3.3)-(2.17) is obtained using the characteristic magnitude,

$$j \sim \frac{k}{\mu}\frac{p_c}{L}\,, \tag{2.18}$$

where p_c is given by Eq. (2.2) and L is given by L_0 or L_k, respectively.

2.3.1 Formulation in classical lubrication variables

The formulation is presented here in terms of the classical lubrication variables for impermeable spheres (3.3). The resulting leading-order lubrication equation that governs the pressure in the near-contact region between permeable particles is

$$2\,q^{-5/2}\,\bar{j}[\bar{p}] - 1 = \frac{1}{\bar{r}}\frac{d}{d\bar{r}}\left[\bar{r}\frac{d\bar{p}}{d\bar{r}}\frac{\bar{h}^3}{12}\,g\left(\frac{\hat{\alpha}_1}{q\bar{h}}, \frac{\hat{\alpha}_2}{q\bar{h}}\right)\right], \qquad \left.\frac{d\bar{p}}{d\bar{r}}\right|_{\bar{r}=0} = 0\,, \quad \lim_{\bar{r}\to\infty}\bar{p}(\bar{r}) = 0\,, \tag{2.19}$$

where the dimensionless form of the gap profile (2.3) is

$$\bar{h} = 1 + \frac{\bar{r}^2}{2}\,, \tag{2.20}$$

and $2\bar{j}$ is the total flux of fluid into the particles. The following paragraphs extend the description of the terms appearing in (2.19).

The tangential fluid velocity on the permeable particle surfaces obeys the Beavers-Joseph slip-velocity boundary condition $v_s = \alpha k^{1/2}\mu^{-1}\tau$ where τ is the tangential stress on the particle surface, and α is the slip coefficient [25,26]. The slip parameters $\hat{\alpha}_i$ $(i = 1, 2)$ that appear in Eq. (2.19) are defined as

$$\hat{\alpha}_i = \alpha_i K_i^{1/2} K^{-2/5}\,, \tag{2.21}$$

where α_i and $K_i = k_i/a^2$, respectively, are the slip coefficient and dimensionless permeability of particle i, and K is the dimensionless mean permeability (3.36). The radial velocity profile is derived in Appendix A.2, where it is shown that the term multiplying $\bar{r}$ in the square brackets on the right side of Eq. (2.19) is the radial flux (A.2.5) recast in dimensionless variables (3.3). The function g, derived in Appendix A.2, accounts for velocity slip on the particle surfaces and is given by

$$g(x_1, x_2) = \frac{1 + 4x_1 + 4x_2 + 12x_1x_2}{1 + x_1 + x_2}\,. \tag{2.22}$$

For particles with equal slip parameters, $\hat{\alpha}_2 = \hat{\alpha}_1$, Eq. (2.22) reduces to

$$g = 1 + 6x_1 \,. \tag{2.23}$$

The total flux of fluid into the particle surfaces is given by Darcy's law,

$$2\,j = \frac{k_1}{\mu}\frac{\partial \hat{p}_1}{\partial n} + \frac{k_2}{\mu}\frac{\partial \hat{p}_2}{\partial n}\,, \tag{2.24}$$

where $\hat{p}_1$ and $\hat{p}_2$ are the intraparticle pressure fields that satisfy Laplace's equation, the gradients are evaluated on the particle surfaces, and n is in the outward normal direction. Continuity of the pressure field across the particle surfaces imposes the length scale L on the intraparticle pressure fields. Given that $L \ll a$, the intraparticle pressures decay quadratically to zero away from the particle surfaces according to Eq. (A.1.5). Thus, to leading order, the intraparticle pressure fields obey Laplace's equation in a semi-infinite region.

Moreover, the intraparticle pressure fields $\hat{p}_1$ and $\hat{p}_2$ are equal because they are forced only by the radial pressure distribution in the gap and pressure variations across the gap (i.e., z-direction) are negligible according to the lubrication approximation. Thus, Eq. (2.24) simplifies to

$$j = \frac{k}{\mu}\frac{\partial \hat{p}}{\partial n}\,, \tag{2.25}$$

indicating that the total intraparticle flux depends only on the mean permeability (2.14).

As shown in Appendix A.1, the pressure gradient at the particle surfaces can be expressed as a boundary integral of radial pressure variations in the gap between the particles. Inserting the result given by Eqs. (A.1.8)-(A.1.10) into Eq. (2.25) and

non-dimensionalizing, yields the flux,

$$\bar{j}[\bar{p}](\bar{r}) = -\int_0^\infty \frac{1}{r'}\frac{d}{dr'}\left(r'\frac{d\bar{p}}{dr'}\right)\phi(r'/\bar{r})\,dr'\,. \tag{2.26}$$

This result demonstrates the non-local character of the lubrication problem for permeable particles, i.e., the local flux into the particles depends on the pressure distribution over the entire lubrication region.

Inserting Eq. (2.26) into Eq. (2.19) defines an integro-differential equation for the pressure in the lubrication region between the particles. The classical description for impermeable spheres is recovered for $q \to \infty$ but the formulation is singular for $q \to 0$, corresponding to particles in contact. An alternate formulation that is non-singular for particles in contact is obtained using the permeable-sphere lubrication variables.

2.3.2 Formulation in permeable sphere lubrication variables

In terms of permeable-sphere lubrication variables (2.17), Eqs. (2.19) and (2.26) become

$$2\,\tilde{j}[\tilde{p}] - 1 = \frac{1}{\tilde{r}}\frac{d}{d\tilde{r}}\left[\tilde{r}\frac{d\tilde{p}}{d\tilde{r}}\frac{\tilde{h}^3}{12}\,g\left(\frac{\hat{\alpha}_1}{\tilde{h}},\frac{\hat{\alpha}_2}{\tilde{h}}\right)\right]\,, \qquad \left.\frac{d\tilde{p}}{d\tilde{r}}\right|_{\tilde{r}=0} = 0\,, \quad \lim_{\tilde{r}\to\infty}\tilde{p}(\tilde{r}) = 0\,, \tag{2.27}$$

and

$$\tilde{j}[\tilde{p}](\tilde{r}) = -\int_0^\infty \frac{1}{r'}\frac{d}{dr'}\left(r'\frac{d\tilde{p}}{dr'}\right)\phi(r'/\tilde{r})\,dr'\,. \tag{2.28}$$

In these variables, the parameter q appears only in the dimensionless gap profile,

$$\tilde{h} = q + \frac{\tilde{r}^2}{2}\,. \tag{2.29}$$

The solution for particles in contact is obtained by setting $q = 0$.

2.3.3 Near-contact motion of a spherical drop and a permeable particle

The lubrication formulation for the near-contact motion between a spherical drop with a fully-mobile interface and a particle with permeability k_1 and slip coefficient α_1 is obtained in the limit $\alpha_2 \to \infty$ [47]. In this limit, Eq. (2.22) reduces to

$$g = 4(1 + 3x_1)\,, \qquad \text{drop}\,. \tag{2.30}$$

Given that the drop is impermeable, $k = \frac{1}{2}k_1$. Accordingly, the dimensionless lubrication formulations (2.19) and (2.27) for this problem are

$$2\,q^{-5/2}\,\bar{j}[\bar{p}] - 1 = \frac{1}{\bar{r}}\frac{d}{d\bar{r}}\left[\bar{r}\frac{d\bar{p}}{d\bar{r}}\frac{\bar{h}^3}{3}\left(1 + 3\frac{\hat{\alpha}_1}{q\bar{h}}\right)\right]\,, \qquad \left.\frac{d\bar{p}}{d\bar{r}}\right|_{\bar{r}=0} = 0\,, \quad \lim_{\bar{r}\to\infty}\bar{p}(\bar{r}) = 0\,, \tag{2.31}$$

and

$$2\,\tilde{j}[\tilde{p}] - 1 = \frac{1}{\tilde{r}}\frac{d}{d\tilde{r}}\left[\tilde{r}\frac{d\tilde{p}}{d\tilde{r}}\frac{\tilde{h}^3}{3}\left(1 + 3\frac{\hat{\alpha}_1}{\tilde{h}}\right)\right]\,, \qquad \left.\frac{d\tilde{p}}{d\tilde{r}}\right|_{\tilde{r}=0} = 0\,, \quad \lim_{\tilde{r}\to\infty}\tilde{p}(\tilde{r}) = 0\,, \tag{2.32}$$

where $\bar{h}$, $\bar{j}$, $\tilde{j}$ and $\tilde{h}$ are given by Eqs. (2.20), (2.26), (2.28) and (2.29), respectively.

Although these equations differ from Eqs. (2.19), (2.26) and (2.27), (2.28), their solutions can be derived from the latter for the case of two permeable particles with equal slip parameters using the following transformation,

$$L_k \to 2^{2/5}L_k'\,, \qquad p \to \frac{1}{4}p'\,, \qquad \hat{\alpha}_1 \to 2^{1/5}\hat{\alpha}'\,. \tag{2.33}$$

Under this transformation, the dimensionless variables and parameters undergo the transformations,

$$\bar{r} \to \bar{r}'\,, \qquad \bar{h} \to \bar{h}'\,, \qquad \bar{p} \to \frac{1}{4}\bar{p}'\,, \tag{2.34}$$

$$\tilde{r} = 2^{-2/5}\tilde{r}' , \qquad \tilde{h} = 2^{-4/5}\tilde{h}' , \qquad \tilde{p} \to 2^{-2/5}\tilde{p}' , \tag{2.35}$$

$$q \to 2^{-4/5} q' . \tag{2.36}$$

Inserting transformations (2.33)-(2.36) into Eqs. (2.31)-(2.32) yields Eqs. (2.19) and (2.27), with g given by Eq. (2.23), that describe the near-contact motion of two particles with parameters q' and $\hat{\alpha}_1 = \hat{\alpha}_2 = \hat{\alpha}'$.

Embedded in formula (2.30) are three assumptions: (i) surface tension gradients, i.e., Marangoni stresses, are absent; (ii) tangential stresses in the gap dominate viscous stresses associated with the fluid flow inside the drop; and (iii) capillary pressure dominates the lubrication pressure (2.2) so that drop deformation is negligible. Respectively, the latter two assumptions require $\lambda\mu W L^{-1} \ll \mu W h_0^{-1}$ and $\mu W a^3 L^{-4} \ll \gamma a^{-1}$, where γ is the coefficient of interfacial tension, $\lambda\mu$ is the drop-phase viscosity, and $L = \max(L_0, L_k)$. Given definitions (2.4) and (2.8), these restrictions impose upper bounds on the viscosity ratio, λ, and Bond number, $Bo = F/(\gamma a)$,

$$\lambda \ll (a/h_0)^{1/2} \max\left[1, q^{-1/2}\right] , \qquad Bo \ll K^{2/5} \max\left[1, q^2\right] . \tag{2.37a,b}$$

Under conditions described by Eq. (2.37a), the system is independent of viscosity ratio. Provided that $Bo \ll K^{2/5}$, the neglect of drop deformation is uniformly valid in gap. This contrasts with the usual near-contact motion of drops with impermeable surfaces where deformation always becomes important at sufficiently small gaps.

2.4 Results

The results presented in Sections 2.4.1-2.4.4 are for the case of no-slip boundary conditions on the surfaces of permeable particles. Under no-slip conditions, only the mean permeability (2.14) enters the problem and the behavior of the system is characterized by a single parameter, q. The effect of velocity slip at the surface

of permeable particles is considered in Section 2.4.5. Extension of the results to describe the lubrication resistance for drops and permeable particles is presented in Section 2.4.6.

2.4.1 Limiting asymptotic results

Large and small values of q

Large q describes conditions where the effect of permeability on near-contact motion is weak. For $q \gg 1$, Eq. (2.19) can be solved by a regular perturbation to obtain an expansion for the pressure in integer powers of $q^{-5/2}$,

$$\bar{p}(\bar{r}, q) = \bar{p}^{(0)}(\bar{r}) + q^{-5/2}\, \bar{p}^{(1)}(\bar{r}) + O(q^{-5})\,, \tag{2.38}$$

and

$$\bar{j}(\bar{r}) = \bar{j}^{(0)}(\bar{r}) + O(q^{-5/2})\,. \tag{2.39}$$

The leading-order pressure distribution is

$$\bar{p}^{(0)}(\bar{r}) = \frac{3}{\bar{h}^2(\bar{r})}\,, \tag{2.40}$$

corresponding to impermeable spheres, and the leading-order intraparticle flux is derived from it,

$$\bar{j}^{(0)}(\bar{r}) = -\int_0^\infty \frac{1}{r'}\frac{d}{dr'}\left(r'\frac{d\bar{p}^{(0)}}{dr'}\right)\phi(r'/\bar{r})\, dr'\,. \tag{2.41}$$

The first-order perturbation problem for the pressure distribution is

$$\frac{1}{\bar{r}}\frac{d}{d\bar{r}}\left[\bar{r}\frac{d\bar{p}^{(1)}}{d\bar{r}}\frac{\bar{h}^3}{12}\right] = 2\,\bar{j}^{(0)}(\bar{r})\,, \qquad \left.\frac{d\bar{p}^{(1)}}{d\bar{r}}\right|_{\bar{r}=0} = 0\,, \quad \lim_{\bar{r}\to\infty}\bar{p}^{(1)}(\bar{r}) = 0\,, \tag{2.42}$$

where $\bar{j}^{(0)}(\bar{r})$ is given by Eq.(2.41). Solving this boundary value problem and inte-

grating by parts yields,

$$\bar{p}^{(1)}(\bar{r}) = 12\left[\int_{\bar{r}}^{\infty} u(r')\bar{j}^{(0)}(r')r'dr' + u(\bar{r})\int_{0}^{\bar{r}} \bar{j}^{(0)}(r')r'dr'\right], \tag{2.43}$$

where

$$u(\bar{r}) = \frac{2\bar{h}(\bar{r})+1}{2\bar{h}^2(\bar{r})} + \log\left(\frac{\bar{h}(\bar{r})-1}{\bar{h}(\bar{r})}\right). \tag{2.44}$$

Small q describes conditions where the intraparticle flux qualitatively affects near-contact motion. For $q \ll 1$, the pressure has an expansion in integer powers of q that can be derived by solving Eq. (2.27) with a regular perturbation,

$$\tilde{p}(\tilde{r}, q) = \tilde{p}^{(0)}(\tilde{r}) + O(q), \tag{2.45}$$

where $\tilde{p}^{(0)}(\tilde{r})$ is obtained by solving Eq. (2.27) with $q = 0$, corresponding to particles in contact.

Far-field pressure and intraparticle flux

By the analysis presented in Appendix A.3, the far-field flux and pressure distributions are

$$\bar{j}(\bar{r}) = -3\,\bar{f}(q)\,\bar{r}^{-3} + O(\bar{r}^{-5}), \tag{2.46}$$

$$\bar{p}(\bar{r}) - \bar{p}^{(0)}(\bar{r}) = -\frac{576}{7}\bar{f}(q)\,\bar{r}^{-7}q^{-5/2} + O(\bar{r}^{-9}\log\bar{r}), \tag{2.47}$$

where $\bar{p}^{(0)}(\bar{r})$ is the pressure distribution corresponding to impermeable spheres (2.40), and $\bar{f}$ is the dimensionless lubrication resistance (2.51a) that depends on the pressure distribution over the entire lubrication region, reflecting the intrinsically non-local character of the problem.

Near-field intraparticle flux

The intraparticle flux is largest near the symmetry axis, $r \ll \max(L_0, L_k)$. For $q \gg 1$, the near-field intraparticle flux is

$$2\bar{j}(\bar{r}) = \frac{9\pi}{2\sqrt{2}} - O(\bar{r}^2 q^{-7/2}) \,, \tag{2.48}$$

which is obtained by inserting the leading-order pressure profile (2.40) and the Green's function expansion (A.1.14) into boundary integral (2.26). For $q \ll 1$, the near-field flux is obtained by expanding Eq. (2.27) to yield

$$2\tilde{j}(\tilde{r}) = 1 - O(\tilde{r}^6) - O(q^3) \,. \tag{2.49}$$

This result indicates that fluid near the symmetry axis flows into the particles rather than radially out of the gap between them.

2.4.2 Pressure and Flux Distributions

The pressure and intraparticle flux distributions in the lubrication region are depicted in figures 2.2 and 2.3. These results were obtained by numerical solution of Eqs.(2.19) and (2.27). The large-q expansions (2.38)-(2.39) are shown for the case $q = 5$.

The inset of figure 2.2 shows that the pressure field is insensitive to particle permeability in the far-field, consistent with Eq. (2.47). The maximum intraparticle flux observed in figure 2.3(a) for $q \to \infty$ agrees with the prediction value (2.48), and the intraparticle flux profile corresponding to $q = 0$ in figure 2.3(b) shows a broad region where fluid enters the permeable particle, consistent with Eq. (2.49). The results in figure 2.3 show regions of negative flux, i.e., fluid flux emerging from the particle interior. This observation is consistent with zero net flux into the particles (i.e., $\int_0^\infty j(r) r dr = 0$), a consequence of the intraparticle pressure field obeying Laplace's

equation, as shown in Appendix A.1. Non-monotonic flux distributions have been found in similar problems [48].

2.4.3 Lubrication and Contact Force

Integrating the pressure distribution obtained by solving Eq. (2.19) or (2.27) yields the hydrodynamic force, F,

$$\frac{F}{6\pi\mu a W} = \left(\frac{a}{L}\right)^2 f(q)\,, \tag{2.50}$$

where f is the dimensionless resistance coefficient corresponding to characteristic length L. Resistance coefficients $\bar{f}$ and $\tilde{f}$, corresponding to classical and permeable-sphere lubrication length scales L_0 and L_k, respectively, are defined

$$\bar{f}(q) = \frac{1}{3}\int_0^\infty \bar{p}\,\bar{r}\,d\bar{r}\,, \qquad \tilde{f}(q) = \frac{1}{3}\int_0^\infty \tilde{p}\,\tilde{r}\,d\tilde{r}\,. \tag{2.51a,b}$$

The resistance coefficients are related, $\bar{f} = q\tilde{f}$, according to Eqs. (2.10) and (2.50). Figure 2.4 shows the resistance coefficients as functions of q; dashed lines depict the limiting formulas given below.

Inserting the pressure distribution for impermeable spheres (2.40) into Eq. (2.51a) yields $\bar{f} = 1$, corresponding to the classical Reynolds lubrication force $F_0 = 6\pi\mu a^2 W/h_0$. Retaining the next term in the large-q expansion (2.38) yields

$$\bar{f}(q) = 1 - \, c\,q^{-5/2} + O(q^{-5})\,, \tag{2.52}$$

where $c \doteq 1.8402$. According to definition (2.10), the result implies that the lubrication force between particles is reduced in proportion to their mean permeability, i.e., $\bar{f} = 1 - c\,k a^{1/2} h_0^{-5/2}$.

Integrating the solution of Eq. (2.27) in formula (2.51b) yields

$$\tilde{f}(q) = \tilde{f}_c^{(0)} - Dq + O(q^2) \tag{2.53}$$

for $q \ll 1$, where $\tilde{f}_c^{(0)}$ is the contact resistance,

$$\tilde{f}_c^{(0)} \doteq 0.7507\,, \tag{2.54}$$

corresponding to $q = 0$, and $D \doteq 0.224$ is the first-order correction. By contrast to the singular lubrication force between impermeable spheres, the lubrication force between permeable spheres with mean dimensionless permeability K attains a finite maximum value at contact,

$$F_c = 6\pi\mu a W K^{-2/5} \tilde{f}_c^{(0)}\,, \tag{2.55}$$

consistent with the scaling (2.13).

Permeable and Impermeable Particles

The near-contact motion between a particle with permeability k_1 and an impermeable particle ($k_2 = 0$) is interesting because it describes the capture of impermeable particles at the interface of a porous medium (e.g., filter thicker than L_k) and the near-contact motion of a permeable particle towards an impermeable wall. This case is encompassed by the above results given that only the mean permeability $k = \frac{1}{2}k_1$ enters the formulation under no-slip boundary conditions.

2.4.4 Contact time

Here, the contact time is calculated for two permeable particles under the action of a constant force along their centerline. The contact time t_c for two particles brought

together from an arbitrary surface-to-surface separation h_∞ has two contributions,

$$\bar{t}_c = \bar{t}_\infty + \bar{t}_0 \,, \tag{2.56}$$

where the overbar denotes time normalized by the Stokes time $6\pi\mu a^2/F$. The time $\bar{t}_\infty$ represents the time required to bring the particles from the initial separation h_∞ to a gap h_0 that lies in the range

$$K^{2/5} \ll \frac{h_0}{a} \ll 1 \,, \tag{2.57}$$

and $\bar{t}_0$ is the time required for the gap to decrease from h_0 to contact in the lubrication regime. For h_0 in the range (2.57), $q_0 = (h_0/a)K^{-2/5} \gg 1$, thus $\bar{t}_\infty$ is insensitive to particle permeability and can be accurately approximated by the time required for impermeable spheres to move from their initial separation h_∞ to a separation h_0. Accordingly,

$$\bar{t}_\infty = C_\infty - \log(h_0/a) \,, \tag{2.58}$$

where C_∞ is determined by the hydrodynamics of impermeable spheres and depends only on the initial separation. By contrast, $\bar{t}_0$ is sensitive to the particle permeability. Taking $W = -dh_0/dt$ and integrating Eq. (2.50) yields

$$\bar{t}_0(q_0) = \int_0^{q_0} \frac{\bar{f}(q)}{q}\, dq \,. \tag{2.59}$$

This calculation can be re-written to isolate the dependence on q_0, given that $q_0 \gg 1$ and $\bar{f} \to 1$ for large q. Rewriting Eq. (2.59) and combining with Eqs. (2.56), (2.58), and (2.10) yields a formula for the contact time

$$\bar{t}_c = C_\infty - \log\left(C_0 K^{2/5}\right) + O(K) \,, \tag{2.60}$$

where

$$C_0 = \exp\left[-\int_0^1 \frac{\bar{f}(q)}{q}\,dq - \int_1^\infty \frac{\bar{f}(q)-1}{q}\,dq\right] \doteq 0.7224\,. \tag{2.61}$$

Accordingly, the contact time between permeable spheres under the action of a constant force is finite, consistent with the discussion below Eq. (2.13).

Rough particles

The contact time for impermeable spheres with small amplitude roughness $\delta \ll a$ is

$$\bar{t}_c = C_\infty - \log(\delta/a)\,, \tag{2.62}$$

where C_∞ depends only on the initial separation, h_∞, as defined above. This result is obtained by assuming that hydrodynamic interactions are identical to smooth spheres, except that contact occurs at a finite separation, δ [49, 50]. This simple model for roughness describes particles with a sparse coating of asperities [51].

An equivalent roughness, $\delta_{\rm eq}$, can be defined as the roughness amplitude that yields the same contact time for rough and permeable spheres under the action of a constant force. Equating the contact time predicted by Eqs. (2.60) and (2.62) for permeable and rough particles, respectively, yields

$$\delta_{\rm eq}/a = C_0\,K^{2/5}\,, \tag{2.63}$$

where C_0 has the numerical value given in Eq. (2.61).

2.4.5 Effect of Velocity Slip

Here, the effect of velocity slip at the surfaces of the permeable particles is explored. Extensions of the large-q and far-field expansions for finite slip are presented in Sections 2.4.5 and 2.4.5. The effect of slip on the contact force and contact time are

presented in Sections 2.4.5 and 2.4.5. The connection to the problem of impermeable particles with slip-velocity boundary conditions is discussed in Section 2.4.5.

Large-q expansion with finite slip

Solving Eq. (2.19) by a regular perturbation for $q \gg 1$ with finite slip requires an expansion of Eq. (2.22) for small values of its arguments. The resulting expansion is

$$\bar{p}(\bar{r}, q, \hat{\alpha}_1, \hat{\alpha}_2) = \bar{p}_0(\bar{r}, q) + \bar{p}_\alpha(\bar{r}, q, \hat{\alpha}_1, \hat{\alpha}_2)\,, \tag{2.64}$$

where $\bar{p}_0(\bar{r}, q)$ is the expansion Eq. (2.38) for no-slip conditions, and $\bar{p}_\alpha(\bar{r}, q, \hat{\alpha}_1, \hat{\alpha}_2)$ is the expansion

$$\bar{p}_\alpha(\bar{r}, q, \hat{\alpha}_1, \hat{\alpha}_2) = q^{-1}\,\bar{p}_\alpha^{(1)}(\bar{r}, \hat{\alpha}_1, \hat{\alpha}_2) + q^{-2}\bar{p}_\alpha^{(2)}(\bar{r}, \hat{\alpha}_1, \hat{\alpha}_2) + q^{-3}\,\bar{p}_\alpha^{(3)}(\bar{r}, \hat{\alpha}_1, \hat{\alpha}_2) + O(q^{-4})\,, \tag{2.65}$$

where

$$\bar{p}_\alpha^{(1)}(\bar{r}, \hat{\alpha}_1, \hat{\alpha}_2) = -\frac{12}{\bar{h}^3}\,\hat{\alpha}_\mathrm{m}\,, \tag{2.66a}$$

$$\bar{p}_\alpha^{(2)}(\bar{r}, \hat{\alpha}_1, \hat{\alpha}_2) = \frac{18}{\bar{h}^4}\,(4\hat{\alpha}_\mathrm{m}^2 - \hat{\alpha}_\mathrm{m}\,\hat{\alpha}_\mathrm{r})\,, \tag{2.66b}$$

$$\bar{p}_\alpha^{(3)}(\bar{r}, \hat{\alpha}_1, \hat{\alpha}_2) = -\frac{144}{5}\frac{1}{\bar{h}^5}\,(16\hat{\alpha}_\mathrm{m}^3 - 7\hat{\alpha}_\mathrm{m}^2\hat{\alpha}_\mathrm{r})\,. \tag{2.66c}$$

Here,

$$\hat{\alpha}_\mathrm{m} = \frac{1}{2}\,(\hat{\alpha}_1 + \hat{\alpha}_2) \tag{2.67}$$

and

$$\hat{\alpha}_\mathrm{r}^{-1} = \frac{1}{2}\left(\hat{\alpha}_1^{-1} + \hat{\alpha}_2^{-1}\right) \tag{2.68}$$

are the mean and reduced slip parameters, respectively, both assumed to be $O(1)$. The leading-order intraparticle flux (2.41) is unaffected by slip for $q \gg 1$.

Inserting expansion (2.64) into Eq. (2.51a) yields

$$\bar{f}(q,\hat{\alpha}_1,\hat{\alpha}_2) = \bar{f}_0(q) + \bar{f}_\alpha(q,\hat{\alpha}_1,\hat{\alpha}_2)\,, \tag{2.69}$$

where $\bar{f}_0(q)$ is given by expansion (2.52), and

$$\bar{f}_\alpha(q,\hat{\alpha}_1,\hat{\alpha}_2) = q^{-1}\,\bar{f}_\alpha^{(1)}(\hat{\alpha}_1,\hat{\alpha}_2) + q^{-2}\bar{f}_\alpha^{(2)}(\hat{\alpha}_1,\hat{\alpha}_2) + q^{-3}\,\bar{f}_\alpha^{(3)}(\hat{\alpha}_1,\hat{\alpha}_2) + o(q^{-3})\,, \tag{2.70}$$

with

$$\bar{f}_\alpha^{(1)}(\hat{\alpha}_1,\hat{\alpha}_2) = -2\hat{\alpha}_{\rm m}\,, \tag{2.71a}$$

$$\bar{f}_\alpha^{(2)}(\hat{\alpha}_1,\hat{\alpha}_2) = \,2\,(4\hat{\alpha}_{\rm m}^2 - \hat{\alpha}_{\rm r}\hat{\alpha}_{\rm m})\,, \tag{2.71b}$$

$$\bar{f}_\alpha^{(3)}(\hat{\alpha}_1,\hat{\alpha}_2) = -\frac{12}{5}\,(16\hat{\alpha}_{\rm m}^3 - 7\hat{\alpha}_{\rm r}\hat{\alpha}_{\rm m}^2)\,. \tag{2.71c}$$

These results indicate that the lubrication resistance for permeable and impermeable particles with slip-velocity boundary conditions coincide up to $O(q^{-2})$; the effect of intraparticle flux enters at $O(q^{-5/2})$.

Far-field expansion with finite slip

At leading order, the far-field intraparticle flux is affected by velocity slip only through the resistance coefficient $\bar{f}(q,\hat{\alpha}_1,\hat{\alpha}_2)$ and is thus given by Eq.(2.46). By the analysis presented in Appendix A.3, the far-field pressure distribution, extended for finite slip, is

$$\bar{p}(\bar{r}) - \bar{p}^{(0)}(\bar{r}) = -96q^{-1}\hat{\alpha}_{\rm m}\bar{r}^{-6} - \frac{576}{7}\bar{f}(q,\hat{\alpha}_1,\hat{\alpha}_2)\,\bar{r}^{-7}q^{-5/2} + O(\bar{r}^{-8})\,, \tag{2.72}$$

where $\bar{p}^{(0)}(\bar{r})$ is the pressure distribution corresponding to impermeable spheres with no-slip boundary conditions (2.40). The result indicates that the effect of slip domi-

nates the effect of permeability in the far-field.

Contact Force

The effect of slip on the contact resistance $\tilde{f}_c$ is shown in figure 2.5 for two special cases:

$$\begin{aligned} &\hat{\alpha}_1 = 0\,, \qquad (1) \\ &\hat{\alpha}_2 = \hat{\alpha}_1\,. \qquad (2) \end{aligned} \tag{2.73}$$

Typically, case (1) describes the near-contact interaction of permeable and impermeable particles, discussed in Section 2.4.3; case (2) typically describes near-contact interactions between particles with equal permeability and slip coefficients, according to the coupling between these parameters indicated by Eq. (2.21).

Figure 2.5 shows the numerical results obtained by solving Eqs. (2.27)-(2.28) with g given by

$$g = \frac{1 + 4x_2}{1 + x_2} \tag{2.74}$$

for case (1), and by Eq. (2.23) for case (2).

For small values of the slip parameters, Eq. (2.22) is expanded for $x_i \ll 1$ $(i = 1, 2)$ to obtain

$$g = 1 + 3(x_1 + x_2) + O(x_i^2)\,. \tag{2.75}$$

This form indicates that the contact resistance, $\tilde{f}_c(\hat{\alpha}_1, \hat{\alpha}_2)$, has the regular expansion

$$\tilde{f}_c(\hat{\alpha}_1, \hat{\alpha}_2) = \tilde{f}_c^{(0)} - A\hat{\alpha}_{\mathrm{m}} + O(\hat{\alpha}_i^2) \tag{2.76}$$

for $\hat{\alpha}_{\mathrm{m}} \ll 1$, where $\hat{\alpha}_{\mathrm{m}}$ is the mean slip parameter (2.67), $\tilde{f}_c^{(0)}$ is the contact resistance under no-slip conditions (2.54), and $A \approx 0.445$; the predictions are shown in figure 2.5.

For $\hat{\alpha}_{\rm r} \gg 1$, the contact force has the asymptotic form

$$\tilde{f}_c(\hat{\alpha}_1, \hat{\alpha}_2) = \frac{5}{9\hat{\alpha}_{\rm r}} \left[\log \hat{\alpha}_{\rm r} + B(\hat{\alpha}_2/\hat{\alpha}_1)\right] + O(\hat{\alpha}_{\rm r}^{-2} \log \hat{\alpha}_{\rm r}) \,, \tag{2.77}$$

according to the derivation given in Appendix A.4, where $\hat{\alpha}_{\rm r}$ is the reduced slip parameter (2.68) and the coefficient B is obtained numerically. For equal slip parameters (i.e., case (2)), $B(1) \approx -0.17$ and the resulting asymptote is shown in figure 2.5.

A different situation arises for $\hat{\alpha}_2 \gg 1$ with $\hat{\alpha}_1 = O(1)$ because $\hat{\alpha}_{\rm r} = O(1)$ so that formula (2.77) does not apply. The limit $\hat{\alpha}_2 \to \infty$ corresponds to the near-contact motion between a spherical drop and a permeable particle with slip parameter $\hat{\alpha}_1$ which has contact resistance

$$\tilde{f}_c^{(d)}(\hat{\alpha}_1) = 2^{-6/5} \tilde{f}_c(2^{-1/5}\hat{\alpha}_1) \,, \tag{2.78}$$

according to Eq. (2.87b). Here, $\tilde{f}_c(\hat{\alpha})$ is the contact resistance for permeable particles with equal slip parameters. Using this result and assuming the form (2.77) for the finite $\hat{\alpha}_2$ correction, yields

$$\tilde{f}_c(\hat{\alpha}_1, \hat{\alpha}_2) = 2^{-6/5} \tilde{f}_c(2^{-1/5}\hat{\alpha}_1) + \frac{A_1(\hat{\alpha}_1)}{\hat{\alpha}_2} \left[\log \hat{\alpha}_2 + B_1(\hat{\alpha}_1)\right] + O(\alpha_2^{-2} \log \alpha_2) \,, \quad \hat{\alpha}_2 \gg 1 \,, \tag{2.79}$$

where the coefficients A_1 and B_1 are obtained numerically. For case (1) (i.e., $\alpha_1 = 0$), the coefficients have the values $A_1 \approx 0.35$, $B_1 \approx 0.43$, and $\tilde{f}_c(0) = \tilde{f}_c^{(0)}$ given by Eq. (2.54). The resulting asymptote is shown in figure 2.5.

Impermeable particles with slip-velocity boundary conditions

The classical first-order lubrication problem for the near-contact motion between impermeable particles with slip-velocity boundary conditions [52] is presented in Appendix A.5. Here, the results for permeable and impermeable particles with slip-

velocity boundary conditions are compared for the case of particles with equal slip parameters.

The comparison requires taking the slip-length in Eq. (A.5.2) as

$$\lambda_s = \alpha k^{1/2}\,, \tag{2.80}$$

consistent with Beavers-Joseph boundary conditions (A.2.2), yielding the slip parameter for impermeable particles,

$$m = 6\hat{\alpha}/q\,. \tag{2.81}$$

Inserting this definition into the small-m expansion (A.5.7) for the resistance $\bar{f}$ recovers the first 3 terms of the large-q expansion (2.70)-(2.71) for permeable particles with equal slip parameters. Similarly, a small-m expansion of the pressure (A.5.3) recovers expansion (2.65)-(2.66) for the case of equal slip parameters. Also, the leading-order, far-field correction to the pressure, $\bar{p} - \bar{p}^{(0)}$, is the same for permeable and impermeable particles, as seen by inserting Eq. (2.81) into the expansion Eq. (A.5.4) and comparing the result to Eq. (2.72) for equal slip parameters.

By contrast to the non-singular contact resistance for permeable particles, $\tilde{f}(q,\hat{\alpha}) = \tilde{f}_c(\hat{\alpha})$ for $q \to 0$, presented above in Section 2.4.5, the resistance for impermeable particles with equal slip coefficients is log-singular at contact,

$$\tilde{f}(q,\hat{\alpha}) = \frac{1}{3\hat{\alpha}}\left[\log\left(\frac{6\hat{\alpha}}{q}\right) - 1\right]\,, \qquad q \to 0\,, \tag{2.82}$$

according to Eqs. (A.5.6) and (2.81).

The foregoing comparison shows that for large gaps, $h_0/a \gg K^{2/5}$ (i.e., $q \gg 1$), permeable particles with slip can be approximated as impermeable particles with slip-velocity boundary conditions [53] but this approximation breaks down at small gaps, $h_0/a = O(K^{2/5})$, where the intraparticle flux becomes significant.

Contact time

In this section, the effect of velocity slip on the contact time between permeable particles under the action of a constant force is explored for the case of equal slip parameters $\hat{\alpha}_1 = \hat{\alpha}_2 = \hat{\alpha}$. In this case, formula (2.60) becomes

$$\bar{t}_c = C_\infty - \log\left(C(\hat{\alpha})K^{2/5}\right) + O(\hat{\alpha}K^{2/5})\,, \tag{2.83}$$

where $C(\hat{\alpha})$ describes the reduction in contact time resulting from velocity slip and is given by

$$C(\hat{\alpha}) = \exp\left[-\int_0^1 \frac{\bar{f}(q,\hat{\alpha})}{q}\,dq - \int_1^\infty \frac{\bar{f}(q,\hat{\alpha})-1}{q}\,dq\right]. \tag{2.84}$$

The results in figure 2.6 show that $C(\hat{\alpha})$ is approximately linear. For $\hat{\alpha} \ll 1$, the contact time (2.83) is controlled by particle permeability with

$$C(\hat{\alpha}) = C_0 + O(\hat{\alpha})\,, \tag{2.85}$$

where C_0 has the numerical value reported in Eq. (2.61), and the constant of proportionality is approximately 1.15. For $\hat{\alpha} \gg 1$, the contact time is controlled by the slip-velocity with

$$C(\hat{\alpha}) = 6e^{-3/2}\hat{\alpha} + O(1)\,, \tag{2.86}$$

according to Eqs. (2.80) and (A.5.11), and the constant is approximately 0.1. The equivalent roughness, defined by Eq. (2.63), can be extended for slip-velocity boundary conditions by inserting $C(\hat{\alpha})$ in place of C_0.

The above results demonstrate that the classical non-integrable lubrication singularity is removed by either of two mechanisms: non-zero particle permeability, or non-zero slip velocity.

2.4.6 Permeable Particles and Drops with Fully-Mobile Interfaces

As shown in Section 2.3.3, the results for a spherical drop with a fully-mobile interface and a particle with permeability k_1 and slip parameter $\hat{\alpha}_1$ can be obtained from the results for a pair of permeable particles using transformation (2.33). Accordingly, the resistance functions $\bar{f}^{(d)}(\hat{\alpha}_1)$ and $\tilde{f}^{(d)}(\hat{\alpha}_1)$, for a spherical drop and a permeable particle, are given by

$$\bar{f}^{(d)}(q,\hat{\alpha}_1) = \frac{1}{4}\bar{f}(2^{4/5}q, 2^{-1/5}\hat{\alpha}_1)\,, \qquad \tilde{f}^{(d)}(q,\hat{\alpha}_1) = 2^{-6/5}\tilde{f}(2^{4/5}q, 2^{-1/5}\hat{\alpha}_1)\,, \quad (2.87a,b)$$

where $\bar{f}(q,\hat{\alpha})$ and $\tilde{f}(q,\hat{\alpha})$ are the resistance functions for permeable particles with equal slip parameters.

Formulas (2.87a,b) extend the foregoing results for the lubrication resistance between permeable particles with equal slip parameters to the case of a spherical drop and a permeable particle with slip parameter $\hat{\alpha}_1$. This includes the results for $\hat{\alpha}_1 = 0$ shown in figure 2.4 and Eqs. (2.52)-(2.54), and, by setting $\hat{\alpha}_2 = \hat{\alpha}_1$, also includes the results shown in figure 2.5 (curve 2) and Eqs. (2.70) and (2.76)-(2.77).

According to formula (2.87a) and the analysis presented in Sections 2.4.4 and 2.4.5, the contact time between a spherical drop and a permeable particle is

$$\bar{t}_c = C'_\infty - \log\left(C'(\hat{\alpha}_1)K^{2/5}\right)\,, \qquad (2.88)$$

where

$$C'(\hat{\alpha}) = \left[C(2^{-1/5}\hat{\alpha})\right]^{1/4}\,. \qquad (2.89)$$

Here, $C(\hat{\alpha})$ is defined by Eq. (2.84) and plotted in figure 2.6. The parameter C'_∞ is determined by the hydrodynamic interactions between a spherical drop and an impermeable sphere; it depends only on the initial separation and the viscosity ratio

of the drop.

The contact time between a spherical drop and a rough particle is similarly modified $\bar{t}_c = C'_\infty - \log(\delta/a)^{1/4}$ thus the equivalent roughness for a permeable particle is the same for its interaction with a spherical particle or a drop.

2.5 Comparison with previous work

In this section, the lubrication resistance obtained from this work is compared to prior bispherical-coordinate calculations by Burganos *et al.* [41] and tangent-sphere-coordinate calculations by Sherwood [37]. The former calculations describe the motion of a permeable sphere toward an impermeable wall, the later describes the contact force of an impermeable sphere at the interface of a semi-infinite permeable medium.

The results presented in figure 2.7(a) show close agreement between the lubrication theory and the bispherical-coordinate calculations of Burganos *et al.*. Errors of the lubrication approximation, defined by

$$\Delta = \frac{F_{\text{ex}} - F_{\text{lub}}}{F_{\text{ex}}}\,, \tag{2.90}$$

are shown in figure 2.7(b), where F_{ex} is the exact result from bispherical coordinate calculations [41], and F_{lub} is the lubrication approximation. The results show that errors increase with gap width and permeability, as expected. When recast in terms of lubrication variables, the bispherical-coordinate calculations cluster onto a single curve in the regime where the lubrication theory is expected to apply (i.e., $(h_0/a)^{1/2} \ll 1$ and $K^{1/5} \ll 1$) as seen in figure 2.8. For a fixed value of the slip coefficient, the lubrication theory predicts a weak, 1/10-power dependence on the permeability accordingly to Eq. 2.21, however, this is not discernible in the exact calculations.

In terms of $K = \frac{1}{2}K_1$, the contact force reported by Sherwood [37] for an impermeable sphere in point contact with a permeable half-space, with $K_1^{1/5} \ll 1$ under

no-slip boundary conditions, is given by Eq. (2.55) with coefficient $\tilde{f}_c^{(0)} = 0.27$; this is in contrast to the value $\tilde{f}_c^{(0)} \doteq 0.7507$ determined herein. We have been unable to reconcile this discrepancy (J.D. Sherwood, personal communication).

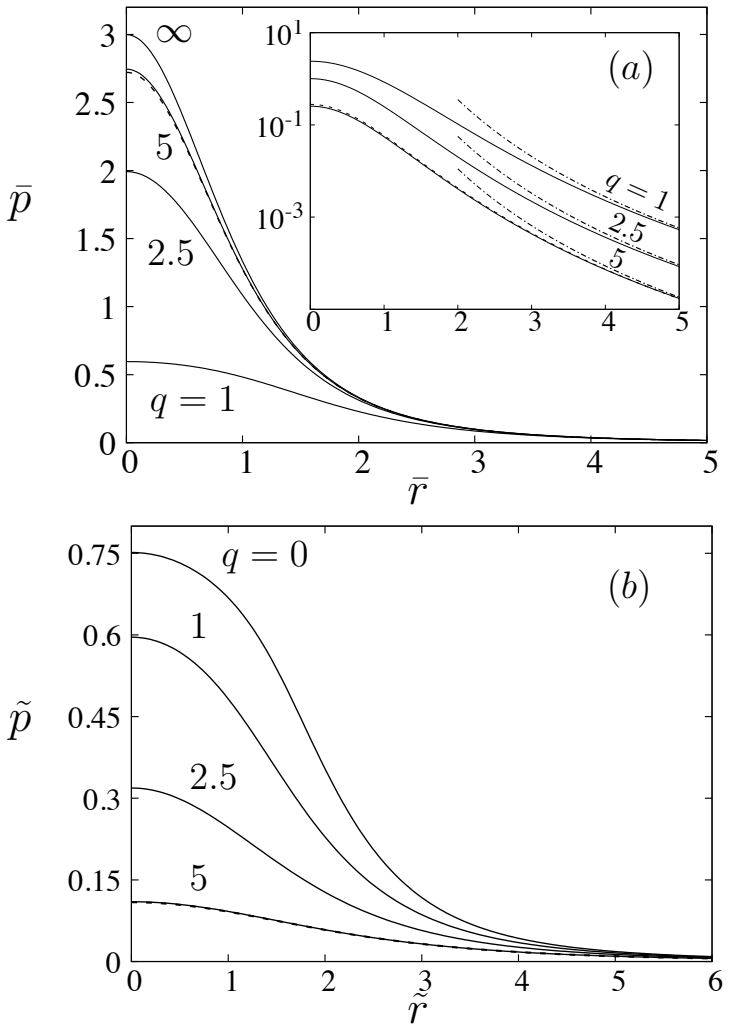

Figure 2.2: Pressure distribution between permeable particles with no-slip boundary conditions, q as indicated; classical (a) and permeable-sphere (b) lubrication variables; two-term large-q expansion (2.38) for $q = 5$ (dashed line); inset: curves depicting $\bar{p}^{(0)}(\bar{r}) - \bar{p}(\bar{r})$, far-field expansion (2.47) (dash-dotted lines).

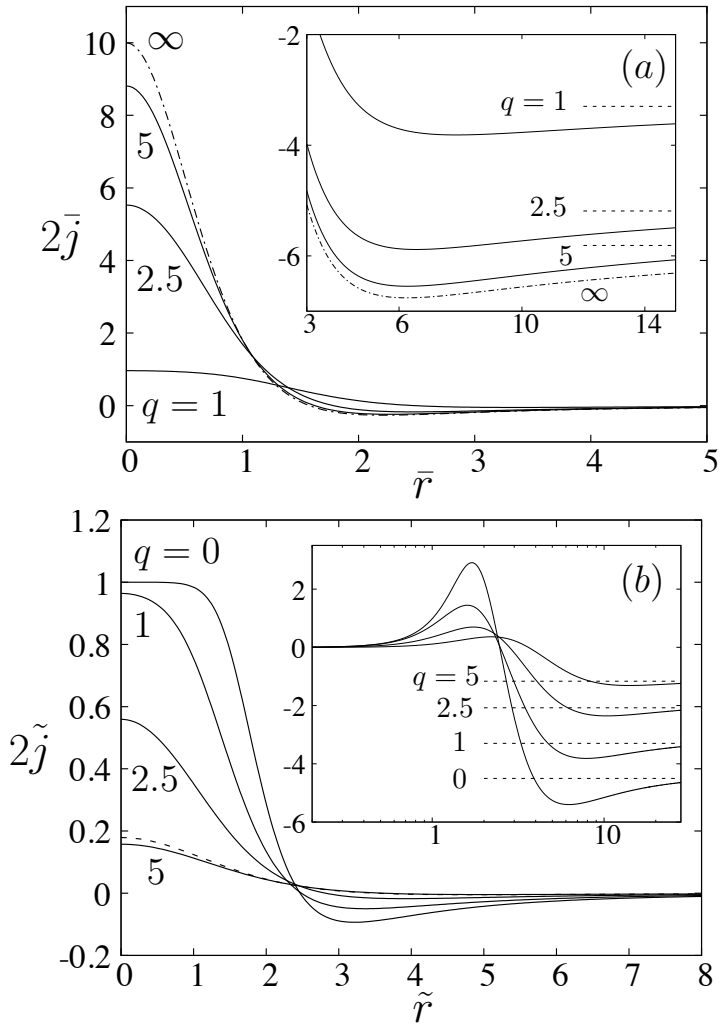

Figure 2.3: Intraparticle flux distribution into permeable particles with no-slip boundary conditions and q as indicated in terms of classical (a) and permeable-sphere (b) lubrication variables; leading-order large-q expansion (2.39) (dash-dotted line) in (a) and curve for $q = 5$ (dashed line) in (b); insets show $2\bar{j}\bar{r}^3$ (a) and $2\tilde{j}\tilde{r}^3$ (b) with far-field expansion (2.46) (dashed lines).

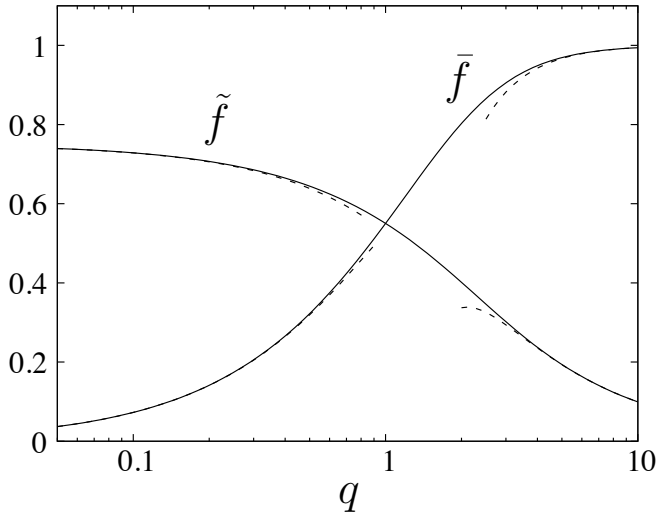

Figure 2.4: Hydrodynamic resistance coefficients (2.51) versus q for permeable particles with no-slip boundary conditions; formulas (2.52)-(2.53) for large and small q (dashed lines).

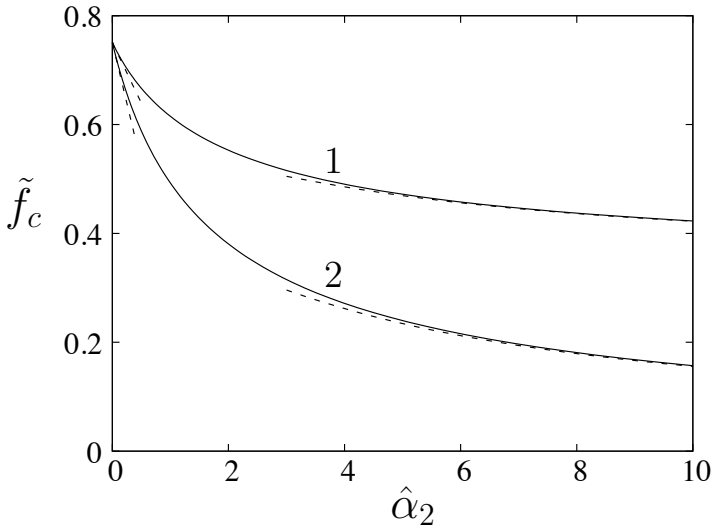

Figure 2.5: Contact resistance as a function of slip parameter; $\hat{\alpha}_1 = 0$ (case 1), $\hat{\alpha}_1 = \hat{\alpha}_2$ (case 2); limiting formulas (2.76)-(2.79) (dashed lines).

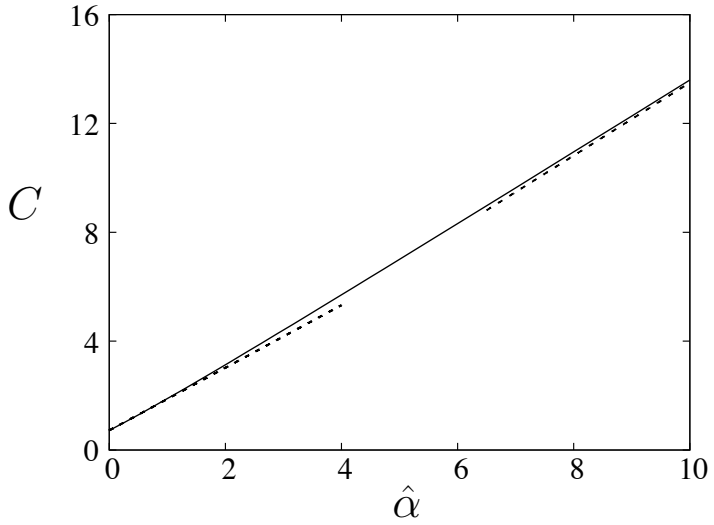

Figure 2.6: Effect of slip parameter on contact time for permeable particles; numerical evaluation (solid line), Eqs.(2.85)-(2.86) (dashed lines).

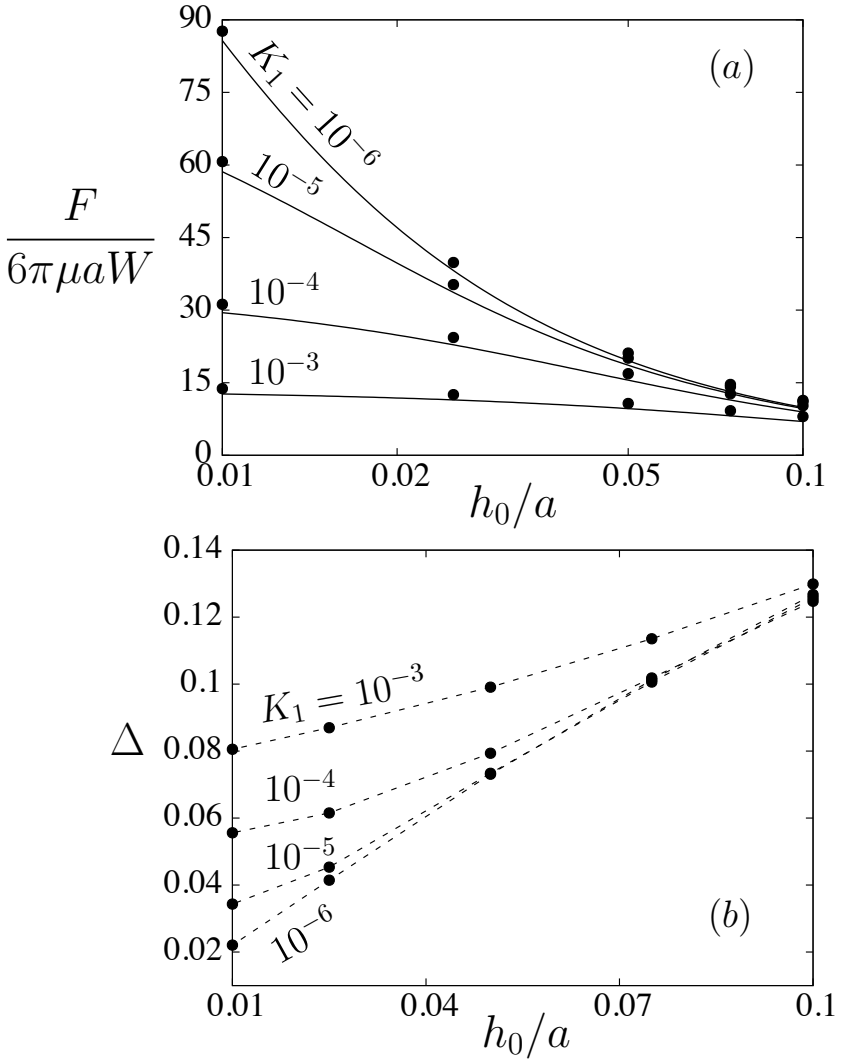

Figure 2.7: Hydrodynamic force between a permeable sphere and an impermeable wall versus gap, $K_1 = 2K$ as indicated, $\alpha_1 = 1$; (a) exact calculations [41] •, lubrication theory (lines); (b) errors of lubrication approximation (2.90) (dashed straight lines between calculations •).

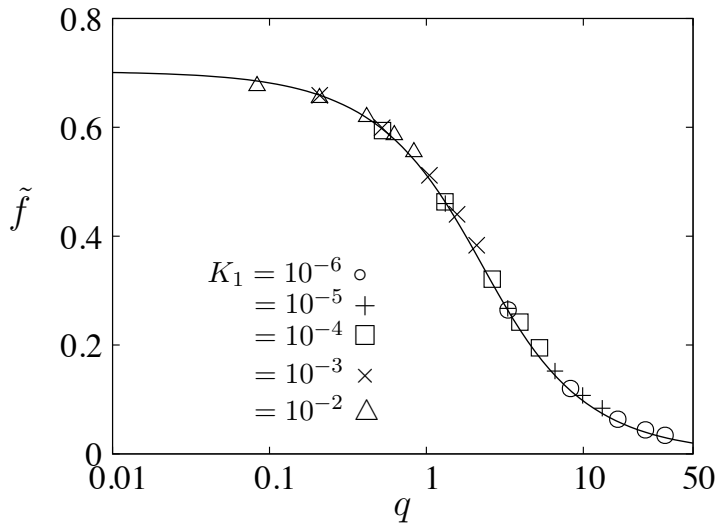

Figure 2.8: Lubrication resistance $\tilde{f}$ versus q; exact calculations [41] $K_1 = 2K$ as indicated, $\alpha_1 = 1$; lubrication theory with $\hat{\alpha}_1 = 0.25$.

Chapter 3

Resistance and Mobility Functions for the Near-Contact motion of Permeable Particles

3.1 Introduction

Understanding particle filtration and particle flocculation require an understanding of the hydrodynamic interactions of permeable particles and particles with a permeable medium [7, 8, 12–14]. The operation and design of packed-bed and fluidized reactors [15, 16] and chromatography columns [17, 18] also relies on a fundamental understanding of the hydrodynamics of permeable particles.

Fluid flow in a homogeneous, permeable material is usually described using Darcy's law [19], whereby the fluid velocity $\mathbf{v}$ in a permeable medium is given by

$$\mathbf{v} = -\frac{k}{\mu}\boldsymbol{\nabla} p\,, \tag{3.1}$$

where k is the permeability, μ is the fluid viscosity, and $\boldsymbol{\nabla} p$ is the local pressure gradient. The permeability scales with the square of the pore size and Darcy's law is

appropriate when the length scale set by pressure gradients is much larger than the pore-scale. This condition is usually satisfied in materials with a dense pore structure, e.g., flow through a packing of solid particles where the particle size sets the pore-scale. Brinkman's equation [54] is more appropriate for materials with very dilute solid networks (e.g., fibrous materials) [20–22]. There have been several investigations of the appropriate boundary condition at the boundary of a permeable material and the free fluid region [25–30] but the no-slip boundary condition is most frequently used.

Hydrodynamic interactions between impermeable particles with thin permeable layers [31–36] and with permeable half-spaces [37, 38]; between permeable particles and impermeable walls [39–41]; and between two permeable particles [42–44] have been investigated. In most of these studies, Darcy's law was used to describe the fluid flow in the permeable medium and no-slip boundary conditions were applied at the interface. Prior studies predict an enhanced axisymmetric near-contact motion between permeable particles or boundaries [31–39,41]. In a recent analysis of the near-contact motion between permeable particles under weak permeability conditions, we explain these findings, showing that the relative velocity between permeable particles under the action of a constant force becomes independent of the gap at sufficiently small gaps. This allows particle-particle contact, in contrast to the linear dependence on gap for impermeable particles that becomes singular at contact [55].

The forces, torques, and stresses acting on a pair of hydrodynamically interacting particles are linearly related to their type of motion through a set of resistance functions that depend on the particle-geometry configuration and obey the Lorentz reciprocal theorem [56]. The resistance functions of spherical particles can be expressed using one or two scalar functions that depend on particle separation and size ratio [57, 58]. Here, we extend our previous lubrication analysis [55] to the case of asymmetric, transverse motion and use the general resistance framework for spheri-

cal particles [11] to derive the complete set of resistance functions that describe the near-contact motion of rigid permeable particles. The flow in the permeable medium is governed by Darcy's law, no-slip boundary conditions are applied on the particle surfaces, and weak permeability conditions are assumed. The formulation allows for arbitrary ratios of particle radii and permeabilities. The governing equations are derived in §2. An integro-differential Reynolds lubrication equation that governs the pressure distribution is derived and solved numerically in §3. The form of the resistance functions that describe the near-contact motion are presented in Section §4 in terms of an additive contribution to the resistance functions for impermeable particles. The additive contribution depends on the pressure distribution between the particles. Mobility functions derived from the lubrication resistance functions are presented in Section §5, including the special case of a particle undergoing near-contact translation parallel to a wall or a permeable half-space under the action of an applied force or an imposed shear-flow. Concluding remarks are presented in §6.

3.2 Problem formulation

The transverse motion of two permeable spherical particles separated by a small gap h_0 in a fluid with viscosity μ is considered here. Particle 1 has radius a_1 and particle 2 has radius $a_2 = \kappa a_1$. The lubrication approximation holds when $h_0 \ll a$ where $a = a_1 a_2/(a_1 + a_2)$ is the reduced radius.

3.2.1 Lubrication equations for transverse motions of permeable particles

A cylindrical coordinate system (r, θ, z) is used with z-coordinate coincident with the line-of-centers of the two particles, and with $z = 0$ at the surface of particle 2 shown in figure 3.1. A Cartesian coordinate system (x, y, z) is also defined with the same

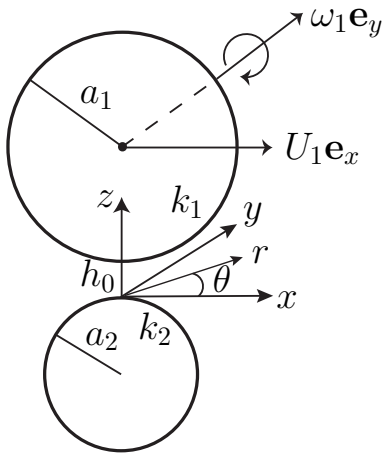

Figure 3.1: Schematic showing two particles with radii and permeabilities a_i and k_i (i=1,2), respectively, separated by a gap h_0; translational and angular velocities U_1 and ω_1, as indicated, where particle 2 is stationary. The Cartesian and cylindrical coordinate systems are shown.

origin, x-coordinate aligned $\theta = 0$, and y aligned with $\theta = \pi/2$. In the near-contact region where $r \ll a$, the surfaces of the particles are approximately parabolic; the surface of particle 1 corresponds to $z = h_0 + r^2/(2a_1)$, and the surface of particle 2 corresponds to $z = -r^2/(2a_2)$.

The leading-order lubrication equations for transverse motion of the particles are

$$\frac{\partial^2 \bar{v}_r}{\partial \bar{z}^2} = \frac{\partial \bar{p}}{\partial \bar{r}}\,, \quad \frac{\partial^2 \bar{v}_\theta}{\partial \bar{z}^2} = \frac{1}{\bar{r}}\frac{\partial \bar{p}}{\partial \theta}\,, \quad \frac{\partial \bar{p}}{\partial \bar{z}} = 0\,, \qquad \frac{1}{\bar{r}}\frac{\partial}{\partial \bar{r}}\left(\bar{r}\bar{v}_r\right) + \frac{1}{\bar{r}}\frac{\partial \bar{v}_\theta}{\partial \theta} + \frac{\partial \bar{v}_z}{\partial \bar{z}} = 0\,. \tag{3.2}$$

The over-bars denote dimensionless variables defined by

$$\bar{r} = \frac{r}{L_1}\,, \quad \bar{z} = \frac{z a_1}{L_1^2}\,, \quad \bar{v}_r = \frac{v_r}{U_0}\,, \quad \bar{v}_\theta = \frac{v_\theta}{U_0}\,, \quad \bar{w} = \frac{w a_1}{U_0 L_1}\,, \quad \bar{p} = \frac{p L_1^3}{\mu U_0 a_1^2}\,, \tag{3.3}$$

where $L_1 = \sqrt{a_1 h_0}$ is the characteristic lateral lengthscale set by the geometry of the near-contact region, and U_0 is a characteristic velocity magnitude that depends on the boundary conditions of the problem.

Only two transverse motions need consideration: (a) transverse motion of particle

1 with velocity in the x-direction (i.e., $\theta = 0$) and magnitude U_1, and (b) rotation of particle 1 with angular velocity in the positive y-direction with magnitude ω_1. Particle 2 is stationary in both problems. The resistances corresponding to the translation and rotation of particle 2 are obtained by relabelling and symmetry, and ultimately the resistances of all transverse motions are derived by the analysis of these two problems in §3.4. Boundary conditions for these two problems are

$$\bar{z} \;=\; \bar{z}_1(\bar{r}) \;:\; \begin{cases} \bar{v}_r = (\bar{U}_1 - \bar{\omega}_1)\cos\theta\,, \quad \bar{v}_\theta = -(\bar{U}_1 - \bar{\omega}_1)\sin\theta \\ \\ \bar{v}_z = -\bar{\omega}_1 \bar{r}\cos\theta + \bar{j}_1[\bar{p}](\bar{r},\theta) \end{cases}, \tag{3.4}$$

$$\bar{z} \;=\; \bar{z}_2(\bar{r}) \;: \qquad \bar{v}_r = \bar{v}_\theta = 0\,, \quad \bar{v}_z = -\bar{j}_2[\bar{p}](\bar{r},\theta)\,, \tag{3.5}$$

where $\bar{z}_1$ and $\bar{z}_2$ define the surfaces of particles 1 and 2, respectively,

$$\bar{z}_1 = 1 + \frac{1}{2}\bar{r}^2\,, \quad \bar{z}_2 = -\frac{1}{2\kappa}\bar{r}^2\,. \tag{3.6}$$

Here, $\bar{U}_1 = U_1/U_0$ and $\bar{\omega}_1 = \omega_1 a_1/U_0$ are the dimensionless translational and rotational velocities of particle 1.

The quantities j_1, j_2 are the fluxes of fluid into the surfaces of the permeable particles that are linear functionals of the pressure distribution in the near-contact region. The fluxes are made dimensionless by the characteristic velocity in the z-direction, $U_0 L_1/a_1$,

$$\bar{j}_i = \frac{j_i a_1}{U_0 L_1}\,, \quad i = 1, 2\,. \tag{3.7}$$

Boundary conditions (3.4)-(3.5) are compatible to the following θ-dependence relations

$$\bar{v}_r = \bar{U}(\bar{r},\bar{z})\cos\theta\,, \quad \bar{v}_\theta = \bar{V}(\bar{r},\bar{z})\sin\theta\,, \quad \bar{v}_z = \bar{W}(\bar{r},\bar{z})\cos\theta\,, \tag{3.8a}$$

$$\bar{p} = \bar{P}(\bar{r})\cos\theta\,, \quad \bar{j}_i = \bar{J}_i[\bar{P}](\bar{r})\cos\theta\,, \quad i = 1, 2\,. \tag{3.8b}$$

Inserting these forms into the lubrication equations (3.2) and boundary conditions (3.4)-(3.5) yields,

$$\frac{\partial^2 \bar{U}}{\partial \bar{z}^2} = \bar{P}'\,, \quad \frac{\partial^2 \bar{V}}{\partial \bar{z}^2} = -\frac{\bar{P}}{\bar{r}}\,, \tag{3.9a, b}$$

$$\frac{\partial \bar{U}}{\partial \bar{r}} + \frac{1}{\bar{r}}\left(\bar{U} + \bar{V}\right) + \frac{\partial \bar{W}}{\partial \bar{z}} = 0\,, \tag{3.10}$$

$$\bar{z} \;=\; \bar{z}_1(\bar{r}) \;:\; \begin{cases} \bar{U} = (\bar{U}_1 - \bar{\omega}_1)\,, \quad \bar{V} = -(\bar{U}_1 - \bar{\omega}_1)\,, \\ \\ \bar{W} = -\bar{\omega}_1 \bar{r} + \bar{J}_1[\bar{P}](\bar{r}). \end{cases} \tag{3.11}$$

$$\bar{z} \;=\; \bar{z}_2(\bar{r}) \;:\; \qquad \bar{U} = \bar{V} = 0\,, \quad \bar{W} = -\bar{J}_2[P](\bar{r})\,, \tag{3.12}$$

Note that $\bar{P}$ depends only on $\bar{r}$, and the prime in Eq. (3.9) denotes a derivative.

Integrating the equations (3.9 a,b) with boundary conditions (3.11)-(3.12) for $\bar{U}$ and $\bar{V}$ yields

$$\bar{U} = \frac{1}{2}\bar{P}'(\bar{r})(\bar{z} - \bar{z}_1(\bar{r}))(\bar{z} - \bar{z}_2(\bar{r})) + \frac{\bar{U}_1 - \bar{\omega}_1}{\bar{h}(\bar{r})}(\bar{z} - \bar{z}_2(\bar{r}))\,, \tag{3.13a}$$

$$\bar{V} = -\frac{1}{2\bar{r}}\bar{P}(\bar{r})(\bar{z} - \bar{z}_1(\bar{r}))(\bar{z} - \bar{z}_2(\bar{r})) - \frac{\bar{U}_1 - \bar{\omega}_1}{\bar{h}(\bar{r})}(\bar{z} - \bar{z}_2(\bar{r}))\,, \tag{3.13b}$$

where

$$\bar{h}(\bar{r}) = \bar{z}_1 - \bar{z}_2 = 1 + \frac{1}{2}(1 + \kappa^{-1})\bar{r}^2\,. \tag{3.14}$$

Inserting these results into the continuity equation (3.10) and integrating using the boundary conditions for $\bar{W}$, yields the Reynolds lubrication equation,

$$\frac{1}{12\,\bar{r}}\left(\bar{r}\bar{P}'\,\bar{h}^3\right)' - \frac{1}{12\,\bar{r}^2}\bar{P}\bar{h}^3 - 2\,\bar{J}\left[\bar{P}\right] = -\frac{A^*}{2}\bar{r}\,, \tag{3.15a}$$

which satisfies the homogeneous boundary conditions,

$$\bar{P}(0) = \bar{P}(\infty) = 0\,, \tag{3.15b}$$

and, A^* is the constant,

$$A^* = \left(\bar{U}_1 + \bar{\omega}_1\right) - \kappa^{-1}\left(\bar{U}_1 - \bar{\omega}_1\right)\,. \tag{3.16}$$

The quantity $2\bar{J} = \bar{J}_1 + \bar{J}_2$ is the combined flux into both particles. For impermeable spheres, i.e., $\bar{J} = 0$, the solution of Eq.(3.15) is

$$\bar{P}_0(\kappa, \bar{r}) = \frac{6}{5}\frac{A^*}{1+\kappa^{-1}}\frac{\bar{r}}{\bar{h}^2}\,. \tag{3.17}$$

3.2.2 Forces, torques and stresslets

The forces, torques, and stresslets on each of the spheres are calculated using the relations [59, 60],

$$\frac{F_{x_1}}{\pi\mu U_0 a_1} = \int_0^{\bar{R}_0}\left[-\bar{P}r + \left(\frac{\partial\bar{V}}{\partial\bar{z}} - \frac{\partial\bar{U}}{\partial\bar{z}}\right)_{\bar{z}=\bar{z}_1}\right] r dr\,, \tag{3.18}$$

$$\frac{F_{x_2}}{\pi\mu U_0 a_1} = \int_0^{\bar{R}_0}\left[-\bar{P}r\kappa^{-1} + \left(\frac{\partial\bar{U}}{\partial\bar{z}} - \frac{\partial\bar{V}}{\partial\bar{z}}\right)_{\bar{z}=\bar{z}_2}\right] r dr\,, \tag{3.19}$$

$$\frac{T_{y_1}}{\pi\mu U_0 a_1^2} = \int_0^{\bar{R}_0}\left(\frac{\partial\bar{U}}{\partial\bar{z}} - \frac{\partial\bar{V}}{\partial\bar{z}}\right)_{\bar{z}=\bar{z}_1} r dr\,, \tag{3.20}$$

$$\frac{T_{y_2}}{\pi\mu U_0 a_1^2} = \int_0^{\bar{R}_0}\left(\frac{\partial\bar{U}}{\partial\bar{z}} - \frac{\partial\bar{V}}{\partial\bar{z}}\right)_{\bar{z}=\bar{z}_2} \kappa\, r dr\,, \tag{3.21}$$

$$\frac{S_{xz,1}}{\pi\mu U_0 a_1^2} = \int_0^{\bar{R}_0} \left[\bar{P} r + \frac{1}{2} \left(\frac{\partial \bar{U}}{\partial \bar{z}} - \frac{\partial \bar{V}}{\partial \bar{z}} \right)_{\bar{z}=\bar{z}_1} \right] r dr \,, \tag{3.22}$$

$$\frac{S_{xz,2}}{\pi\mu U_0 a_1^2} = \int_0^{\bar{R}_0} \left[-\bar{P} r \kappa^{-1} + \frac{1}{2} \left(\frac{\partial \bar{U}}{\partial \bar{z}} - \frac{\partial \bar{V}}{\partial \bar{z}} \right)_{\bar{z}=\bar{z}_2} \right] \kappa \, r dr \,, \tag{3.23}$$

where the upper limit of integration $\bar{R}_0 = O(\sqrt{a_1/h_0})$ and thus lies in the matching region between the lubrication and outer regions.

Inserting Eqs. (3.13 a, b) into Eqs. (3.18)-(3.23) and integrating by parts to separate the pressure contributions yields,

$$\frac{F_{x_1}}{\pi\mu U_0 a_1} = \frac{\kappa^{-1} - 1}{\kappa^{-1} + 1} \frac{A^*}{2} [I_1 - (1 + \kappa^{-1})^{-2} \, I_K] - 2BI_2 \,, \tag{3.24}$$

$$\frac{F_{x_2}}{\pi\mu U_0 a_1} = \frac{1 - \kappa^{-1}}{1 + \kappa^{-1}} \frac{A^*}{2} [I_1 - (1 + \kappa^{-1})^{-2} \, I_K] + 2BI_2 \,, \tag{3.25}$$

$$\frac{T_{y_1}}{\pi\mu U_0 a_1^2} = -\frac{A^*}{2} [I_1 - (1 + \kappa^{-1})^{-2} \, I_K] + 2BI_2 \,, \tag{3.26}$$

$$\frac{T_{y_2}}{\pi\mu U_0 a_1^2} = \frac{\kappa}{2} A^* [I_1 - (1 + \kappa^{-1})^{-2} \, I_K] + 2 \, \kappa \, BI_2 \,, \tag{3.27}$$

$$\frac{S_{xz,1}}{\pi\mu U_0 a_1^2} = \frac{3 - \kappa^{-1}}{1 + \kappa^{-1}} \frac{A^*}{4} [I_1 - (1 + \kappa^{-1})^{-2} \, I_K] + BI_2 \,, \tag{3.28}$$

$$\frac{S_{xz,2}}{\pi\mu U_0 a_1^2} = \frac{\kappa - 3}{\kappa^{-1} + 1} \frac{A^*}{4} [I_1 - (1 + \kappa^{-1})^{-2} \, I_K] + \, \kappa \, BI_2 \,, \tag{3.29}$$

where A is defined by Eq. (3.16) and B is given by,

$$B = \left(\bar{U}_1 - \bar{\omega}_1 \right) \,. \tag{3.30}$$

Here, we define the integrals

$$I_1(\xi,\kappa) = \int_0^{\bar{R}_0} \bar{P}_0^* r^2 dr\,, \qquad I_2(\xi,\kappa) = \int_0^{\bar{R}_0} \frac{r}{\bar{h}}\, dr\,, \tag{3.31}$$

and

$$I_K(\xi,\kappa,K) = (1+\kappa^{-1})^2 \int_0^{\infty} (\bar{P}_0^* - \bar{P}^*) r^2 dr\,, \tag{3.32}$$

where the pressure is factored as

$$\bar{P} = \frac{A^*}{1+\kappa^{-1}} \bar{P}^*\,, \tag{3.33}$$

and $\xi = h_0/\bar{a}$ is the gap normalized by the average radius, $\bar{a} = \frac{1}{2}(a_1 + a_2)$.

This rearrangement of Eqs. (3.18)-(3.23) is useful because it isolates the influence of particle permeability. The integrals I_1 and I_2 describe the dynamics of impermeable spherical particles; only the permeability integral, I_K, depends on the permeability. The upper limit for I_K can be extended to infinity indicating that permeability does not affect flow in the matching region.

3.3 Solution of the Reynolds equation

In this section, an integro-differential equation is derived for the pressure that allows evaluation of the permeability integral, I_K. Numerical and asymptotic limiting results are presented. As shown below, the permeability integral depends on a single parameter,

$$I_K(\xi,\kappa,K) = g(q)\,, \tag{3.34}$$

where q is defined

$$q = K^{-2/5} \frac{h_0}{a}\,. \tag{3.35}$$

Here, K is the dimensionless permeability,

$$K = k/a^2\,, \tag{3.36}$$

k is the mean permeability,

$$k = \frac{1}{2}(k_1 + k_2)\,, \tag{3.37}$$

and $a = a_1 a_2/(a_1 + a_2)$ is the reduced radius.

To obtain the functional form (3.34), we rescale the lubrication equation (3.15) using the variables,

$$\hat{r} = \frac{r}{L_0}\,, \quad \hat{z} = \frac{za}{L_0^2}\,, \quad \hat{P} = \frac{pL_0^3}{\mu U_0 a^2}\,, \quad \hat{J} = \frac{Ja}{U_0 L_0} q^{5/2}\,, \tag{3.38}$$

where

$$L_0 = \sqrt{a h_0}\,, \tag{3.39}$$

is the length scale set by the geometry of the near-contact region (3.14), and a is the reduced radius. The scaling for the particle flux is obtained using the order-of-magnitude estimate, $J \sim kp/\mu L_0$ where $p \sim \mu U_0 a^2/L_0^3$ is the magnitude of pressure in the near-contact region. In terms of these variables, the Reynolds lubrication problem (3.15) becomes

$$\frac{1}{12\,\hat{r}}\left(\hat{r}\hat{P}^{*\prime}\,\hat{h}^3\right)' - \frac{1}{12\,\hat{r}^2}\hat{P}^*\hat{h}^3 - 2\,q^{-5/2}\hat{J}\left[\hat{P}^*\right] = -\frac{1}{2}\hat{r}\,, \qquad \hat{P}^*(0) = \hat{P}^*(\infty) = 0\,, \tag{3.40}$$

where

$$\hat{h}(\bar{r}) = 1 + \frac{1}{2}\hat{r}^2 \tag{3.41}$$

is the gap profile, and

$$g(q) = \int_0^\infty (\hat{P}_0^* - \hat{P}^*) r^2 dr \tag{3.42}$$

is the permeability integral (3.32). Here, $\hat{P}^*$ is the factored pressure, related to $\hat{P}$ by Eq. (3.33), and

$$\hat{P}_0^*(\hat{r}) = \frac{6}{5}\frac{\hat{r}}{\hat{h}^2}\,, \tag{3.43}$$

is solution of Eq. (3.40) corresponding to impermeable spheres, i.e., $\hat{J} = 0$, which is consistent with Eq. (3.17) via (3.33).

As shown in Appendix B.1, the flux depends only on the mean permeability (3.37) and is expressed as a boundary integral of the pressure distribution in the gap between the particles,

$$\hat{J}[\hat{P}^*](\hat{r}) = -\int_0^\infty w[\hat{P}^*](r')\,\phi(r'/\hat{r})\,dr'\,, \tag{3.44}$$

where

$$w[\hat{P}^*](r) = \frac{d}{dr}\left[\frac{1}{r}\frac{d}{dr}\left(r\hat{P}^*\right)\right]\,, \tag{3.45}$$

and the Green's function, $\phi(x)$, is defined by Eq.(B.1.13).

3.3.1 Permeability integral

Results for the permeability integral, $g(q)$, presented in figure 3.2, were obtained by a numerical solution of the Reynolds equation (3.40). The limiting behaviors for small and large q, derived in Appendix B.2, are

$$g(q) = -\frac{12}{5}\log q + c_1 + c_2 q + O(q^2)\,, \qquad q \ll 1\,, \tag{3.46}$$

with $c_1 \doteq -0.48$ and $c_2 \doteq -1.5$, and

$$g(q) = b_1 q^{-5/2} + O\left(q^{-5}\right)\,, \qquad q \gg 1\,, \tag{3.47}$$

with $b_1 \doteq 2.12$.

3.4 Transverse resistance functions for permeable spheres

Rearranging Eqs.(3.24)-(3.29) to isolate the type of motion yields the forces, torques, and stresslets in terms of resistance functions. The notation and general definition of resistance functions used in the literature is followed [11, 58]. The results are

$$-\frac{F_{x_1}}{\pi\mu U_0 a_1} = 6\,Y_{11}^{A}\bar{U}_1 + 4\,Y_{11}^{B}\bar{\omega}_1\,, \tag{3.48}$$

$$-\frac{F_{x_2}}{\pi\mu U_0 a_1} = 3(1+\kappa)Y_{21}^{A}\bar{U}_1 + (1+\kappa)^2 Y_{12}^{B}\bar{\omega}_1\,, \tag{3.49}$$

$$-\frac{T_{y_1}}{\pi\mu U_0 a_1^2} = 4\,Y_{11}^{B}\bar{U}_1 + 8\,Y_{11}^{C}\bar{\omega}_1\,, \tag{3.50}$$

$$-\frac{T_{y_2}}{\pi\mu U_0 a_1^2} = (1+\kappa)^2\,Y_{21}^{B}\bar{U}_1 + (1+\kappa)^3\,Y_{21}^{C}\bar{\omega}_1\,, \tag{3.51}$$

$$-\frac{S_{xz,1}}{\pi\mu U_0 a_1^2} = -4\,Y_{11}^{G}\bar{U}_1 + 8\,Y_{11}^{H}\bar{\omega}_1\,, \tag{3.52}$$

and

$$-\frac{S_{xz,2}}{\pi\mu U_0 a_1^2} = -(1+\kappa)^2\,Y_{21}^{G}\bar{U}_1 + (1+\kappa)^3\,Y_{21}^{H}\bar{\omega}_1\,. \tag{3.53}$$

Using symmetry relations and the Lorentz reciprocal theorem, the grand resistance matrix can be derived from this set of of resistance functions, as shown in Appendix B.3.

The leading-order resistance functions are

$$Y_{\alpha\beta}^{R}(\xi,\kappa,q) = Y_{\alpha\beta}^{R,0}(\xi,\kappa) - g_{\alpha\beta}^{R}(\kappa)\,g(q) + O\left(\xi\log\xi^{-1}\right)\,, \tag{3.54}$$

where the superscript R refers to one of the resistance tensors in the resistance matrix B.3.1. The functions $Y^{R,0}_{\alpha\beta}$ are the classical resistance functions for impermeable spheres (B.3.4)-(B.3.13) [57, 59, 60]. Eq.(3.54) indicates that particle permeability additively affects the transverse resistance functions. Permeability enters only in the permeability integral, $g(q)$, defined by (3.32) and (3.34) with a separable size-ratio dependence through the functions $g^R_{\alpha\beta}$ given by

$$g^A_{11} = \frac{\kappa}{12}\frac{(\kappa-1)^2}{(\kappa+1)^3}\,, \qquad g^A_{21} = -\frac{\kappa}{6}\frac{(\kappa-1)^2}{(\kappa+1)^4}\,, \tag{3.55}$$

$$g^B_{11} = \frac{\kappa}{8}\frac{(\kappa-1)}{(\kappa+1)^2}\,, \qquad g^B_{21} = -\frac{\kappa^2}{2}\frac{\kappa-1}{(\kappa+1)^4}\,, \tag{3.56}$$

$$g^C_{11} = \frac{\kappa}{16(1+\kappa)}\,, \qquad g^C_{21} = -\frac{\kappa^2}{2(1+\kappa)^4}\,, \tag{3.57}$$

$$g^G_{11} = \frac{(3\kappa-1)(\kappa-1)\kappa}{16(1+\kappa)^3}\,, \qquad g^G_{21} = \frac{(\kappa-3)(\kappa-1)\kappa^2}{4(1+\kappa)^5}\,, \tag{3.58}$$

$$g^H_{11} = \frac{\kappa}{32}\frac{1-3\kappa}{(1+\kappa)^2}\,, \qquad g^H_{21} = -\frac{\kappa^2}{4}\frac{\kappa-3}{(1+\kappa)^5}\,. \tag{3.59}$$

3.5 Mobility functions

Here, we present pairwise mobilities of permeable particles defined by the relative velocity of the particles $\mathbf{U}_{12} = \mathbf{U}_2 - \mathbf{U}_1$ under the actions of forces and an imposed flow [61, 62],

$$\begin{aligned}\mathbf{U}_{12} \;=\; & \left[G(s)\hat{\mathbf{r}}\hat{\mathbf{r}} + H(s)\left(\mathbf{I}-\hat{\mathbf{r}}\hat{\mathbf{r}}\right)\right]\cdot\mathbf{U}^{\infty}_{12,0} \\ & + \left[L(s)\hat{\mathbf{r}}\hat{\mathbf{r}} + M(s)\left(\mathbf{I}-\hat{\mathbf{r}}\hat{\mathbf{r}}\right)\right]\cdot\mathbf{U}^{\infty}_{12,g} \\ & + \mathbf{E}_\infty\cdot\mathbf{r} + \boldsymbol{\omega}_\infty\times\mathbf{r} - \left[A(s)\hat{\mathbf{r}}\hat{\mathbf{r}} + B(s)\left(\mathbf{I}-\hat{\mathbf{r}}\hat{\mathbf{r}}\right)\right]\cdot\mathbf{E}_\infty\cdot\mathbf{r}\,.\end{aligned} \tag{3.60}$$

Here, $\mathbf{r} = \mathbf{x}_2 - \mathbf{x}_1$ is the vector between the particle centers, $\hat{\mathbf{r}} = \mathbf{r}/|\mathbf{r}|$ is a unit vector along the line-of-centers, $\mathbf{I}$ is the identity tensor, and $s = |\mathbf{r}|/\bar{a}$ is the center-to-center separation normalized by the average radius, $\bar{a} = \frac{1}{2}(a_1 + a_2)$. The quantities $\mathbf{E}_\infty$ and $\boldsymbol{\omega}_\infty$ are the imposed rate-of-strain and vorticity in the fluid, and $\mathbf{U}^\infty_{12,0}$ and $\mathbf{U}^\infty_{12,g}$ are, respectively, the relative velocities in the absence of hydrodynamic interactions (i.e., $s \to \infty$) under the action of equal and opposite forces and under the action of gravity,

$$\mathbf{U}^\infty_{12,0} = \frac{\mathbf{F}_2 - \mathbf{F}_1}{6\pi\mu a}\,, \quad \mathbf{U}^\infty_{12,g} = \frac{2\,(a_2^2\gamma - a_1^2)\,\Delta\rho_1\,\mathbf{g}}{9\mu}\,, \tag{3.61}$$

where $\mathbf{F}_1 = -\mathbf{F}_2$, a is the reduced radius, $\mathbf{g}$ is the acceleration of gravity, $\Delta\rho_i = \rho_i - \rho$ is the difference between the density of particle i ($i = 1, 2$) and the density of the fluid, and

$$\gamma = \frac{\Delta\rho_2}{\Delta\rho_1}\,, \tag{3.62}$$

is the ratio of particle density differences.

Equation (4.4) defines the pairwise axisymmetric and transverse mobility functions G, L, A and H, M, B, respectively. According to their definitions, G, H, L and M tend to unity at large separations, whereas A and B vanish for $s \to \infty$. The pair mobilities depend on the center-to-center separation, s, size ratio, κ, and permeability, K. (L and M also depend on the density difference ratio, γ.) For the weak permeability regime $K \ll 1$ considered herein, mobilities corresponding to impermeable particles can be used outside of the near-contact region with $O(K)$ error.

The near-contact axisymmetric mobilities, G, L, A were derived from our recent analysis [55] by the procedure described below. The near-contact mobilities H, M, B for transverse motion were obtained by inverting the resistance matrix (B.3.1). Outside of the near-contact region, mobilities were calculated using a code provided by A.Z. Zinchenko [63] based on a bispherical-coordinate solution for impermeable spheres [64].

3.5.1 Axisymmetric mobilities

In a recent axisymmetric analysis for the near-contact motion of permeable particles [55], we obtained

$$G = \frac{(1+\kappa)^2}{2\kappa}\frac{\xi}{f(q)} = \frac{\epsilon}{f(q)}\,, \qquad \epsilon \ll 1\,, \tag{3.63}$$

where $\epsilon = h_0/a$ is the gap normalized by the reduced radius, q is the permeability parameter defined by Eq. (4.30), and $\bar{f}$ is the solution of an axisymmetric integrod-ifferential Reynolds lubrication equation analogous to Eq. (3.40). For $q \gg 1$,

$$G = \left(1 + b_0 q^{-5/2} + O(q^{-5})\right)\epsilon\,, \tag{3.64}$$

where $b_0 \doteq 1.8402$, recovering the result for impermeable particles for $q \to \infty$. For $q \ll 1$, the mobility assumes the limiting form,

$$G = \left(c_0 + c_1 q + O(q^2)\right) K^{2/5}\,, \tag{3.65}$$

where $c_0 \doteq 1.332$, and $c_1 \doteq .397$. This result indicates that the particles undergo a constant approach velocity at close contact under the action of a constant force.

In the near-contact region, L and $1 - A$ are proportional to G, motivating the definition of the modified mobility functions $\hat{L}$ and $\hat{A}_1$,

$$\hat{L}(\epsilon,\kappa,q) = \frac{L(\epsilon,\kappa,q)}{\hat{F}_c^{(g)}(\kappa)} = \hat{A}_1(\epsilon,\kappa,q) = \frac{1 - A(\epsilon,\kappa,q)}{\hat{F}_c^{(E)}(\kappa)} = G(\epsilon,q)\,, \tag{3.66}$$

where $\hat{F}_c^{(g)}$ and $\hat{F}_c^{(E)}$ are dimensionless contact forces, obtained by the procedure described in Appendix B.4 and given by Eqs. (B.4.3)-(B.4.4). These forces arise between two spheres in point-contact, migrating along their line-of-centers in gravity-driven motion, and in axisymmetric straining flow, respectively. The mobility function L also depends on the ratio of the particle density differences, γ. Representative values

for the contact forces are provided in Table C.1.

Axisymmetric mobilities $G, \hat{L}$, and $\hat{A}$ are shown in figure 3.3 as a function of gap. Part (a) of the figure demonstrates the common behavior of the modified axisymmetric mobilities (3.66); permeability qualitatively changes the near-contact motion for $h_0/a \leq O(K^{2/5})$, corresponding to $q \leq O(1)$. Part (b) of figure 3.3 shows the universal near-contact behavior predicted by combining Eqs.(3.63) and (3.66),

$$GK^{-2/5} = \hat{A}_1 K^{-2/5} = \hat{L} K^{-2/5} = \frac{q}{f(q)}\,. \tag{3.67}$$

3.5.2 Transverse mobilities

The transverse mobilities H, M and B have the near-contact form

$$\Lambda(\xi, \kappa, K) = \frac{\lambda_1 + \lambda_2 \log \xi^{-1} + \lambda_3 \left[\log \xi^{-1} - \frac{5}{12} g(q)\right] \log \xi^{-1} + \lambda_6 g(q)}{\lambda_4 + \lambda_5 \log \xi^{-1} + \left[\log \xi^{-1} - \frac{5}{12} g(q)\right] \log \xi^{-1} + \lambda_7 g(q)}\,, \tag{3.68}$$

where the size-ratio-dependent numerical coefficients are listed in Tables 3.5.2, 3.5.2, and 3.5.2, respectively. The results shown in figure 3.4 demonstrate that permeability quantitatively affects the transverse mobilities H, M and B, for $\xi < K^{2/5}$. Inserting (3.46) into (4.33) and taking the limit as $\xi \to 0$ yields the contact values of the transverse mobilities,

$$\Lambda_c(\kappa, K) = \lambda_3 \frac{\log K^{-1} + \lambda_1'}{\log K^{-1} + \lambda_2'}\,, \qquad \xi = 0\,, \tag{3.69}$$

where Λ_c is the contact value of the transverse mobility function H, M, or B, and the coefficients λ_1' and λ_2' are given by

$$\lambda_1' = 6\lambda_6\lambda_3^{-1} + \frac{5}{2}\lambda_2\lambda_3^{-1} - \frac{5}{2}\log\nu - \frac{25}{24}c_1\,, \qquad \lambda_2' = 6\lambda_7 + \frac{5}{2}\lambda_5 - \frac{5}{2}\log\nu - \frac{25}{24}c_1\,, \tag{3.70a,b}$$

where $\nu = 2\kappa(1+\kappa)^{-2}$ and $c_1 \doteq -0.48$ from Eq. (3.46). For convenience, values for λ_1' and λ_2' are listed in Table 3.5.2. Contact values for impermeable particles are given by λ_3. According to formula (3.69), Λ_c increases for $K > 0$ if $\lambda_1' > \lambda_2'$ and decreases if $\lambda_1' < \lambda_2'$. The values in Table 3.5.2 indicate that contact mobilities H and M increase with K whereas B decreases, consistent with results shown in figure 3.4. Given that $H = M = 1$ and $B = 0$ in the absence of hydrodynamic interactions, these observations indicate that particle permeability always diminishes the strength of hydrodynamic pair interactions. Even very small values of permeability can significantly affect tangential near-contact motion because its effect decays only logarithmically.

Permeability has the largest effect for extreme size ratios and no effect for equal size particles because no lubrication pressure is generated by the motion. This is seen in figure 3.4 (a, c) and in the contact values for the mobilities (3.69), given that $\lambda_1' = \lambda_2'$ for $\kappa = 1$, according to Table 3.5.2.

A universal near-contact regime corresponding to Eq. (3.67) for axisymmetric mobilities does not exist for the transverse mobilities; transverse mobilities depend on gap, size ratio, and permeability for $q \leq O(1)$.

κ	λ_1	λ_2	λ_3	λ_4	λ_5	λ_6	λ_7
1	5.087	2.967	.4010	6.325	6.043	-.4514	-.5613
0.9	5.066	2.969	.3997	6.272.	6.036	-.4514	-.5589
0.75	4.921	2.980	.3911	5.927	5.985	-.4508	-.5428
0.6	4.555	2.995	.3696	5.105	5.831	-.4479	-.5020
0.5	4.100	2.993	.3432	4.177	5.599	-.4425	-.4509
0.4	3.387	2.956	.3027	2.877	5.163	-.4313	-.3686
0.3	2.317	2.849	.2443	1.222	4.378	-.4103	-.2378
0.25	1.623	2.756	.2080	0.3221	3.796	-.3951	-.1465
0.125	-0.6696	2.393	.1033	-1.540	1.516	-0.3451	.2069

Table 3.1: Coefficients of transverse mobility H given by Eq. (4.33).

κ	λ_1	λ_2	λ_3	λ_4	λ_5	λ_6	λ_7
0.9	3.128	2.1402	.2206	6.272	6.036	-.2745	-.5589
0.75	2.942	2.104	.2075	5.926	5.985	-.2661	-.5428
0.6	2.529	2.022	.1794	5.105	5.831	-.2477	-.5020
0.5	2.074	1.915	.1497	4.177	5.599	-.2267	-.4509
0.4	1.461	1.736	.1114	2.877	5.163	-.1965	-.3686
0.3	.7212	1.461	.06812	1.222	4.378	-.1560	-.2378
0.25	.3448	1.276	.04718	.3221	3.796	-.1326	-.1465
0.125	-.3928	.6909	9.123×10^{-3}	-1.540	1.516	-.06637	.2069

Table 3.2: Coefficients of transverse mobility M ($\gamma = 1$) given by Eq. (4.33).

κ	λ_1	λ_2	λ_3	λ_4	λ_5	λ_6	λ_7
1	-1.902	1.501	.4060	6.325	6.043	.1688	-.5613
0.9	-1.894	1.496	.4106	6.272.	6.036	.1686	-.5589
0.75	-1.842	1.465	.4403	5.926	5.985	.1681	-.5428
0.6	-1.716	1.378	.5089	5.105	5.831	.1682	-.5020
0.5	-1.566	1.262	.5831	4.177	5.599	.1711	-.4509
0.4	-1.348	1.063	.6822	2.877	5.163	.1816	-.3686
0.3	-1.059	.7307	.7987	1.222	4.378	.2112	-.2378
0.25	-.8967	.4932	.8572	.3231	3.796	.2403	-.1465
0.125	-.5606	-.4511	.9707	-1.540	1.516	.4213	.2069

Table 3.3: Coefficients of transverse mobility B given by Eq. (4.33).

Mobility of a particle moving parallel to a wall

In this section, the motion of a sphere in close-contact with a wall is considered, corresponding to the limit $\kappa \to \infty$. Two problems are considered: (I) motion of a particle in a quiescent fluid under the action of an imposed force $\mathbf{F} = F_0\,\mathbf{e}_x$ parallel to the wall and (II) motion of a force-free particle in an imposed shear-flow parallel to the wall, $\mathbf{U}_\infty = E_\infty z\,\mathbf{e}_x$. The particle is torque-free in both problems.

The resistance formulation for problems (I) and (II), derived from the general resistance formulation (B.3.1) for the particle-wall configuration ($\kappa \to \infty$), is

$$-\frac{F_{x_1}}{\pi\mu U_0 a_1} = 6\,Y_{11}^{A,\infty}\bar{U}_1 + 4\,Y_{11}^{B,\infty}\bar{\omega}_1 - (6\,Y_{11}^{A,\infty} + 2\,Y_{11}^{B,\infty} - 4Y_{11}^{G,\infty})\bar{E}_\infty\,, \qquad (3.71)$$

	H		M ($\gamma = 1$)		B	
κ	λ_1'	λ_2'	λ_1'	λ_2'	λ_1'	λ_2'
1	0	0	-	-	0	0
0.9	14.03	13.98	19.03	13.98	13.81	13.98
0.75	14.42	13.99	19.94	13.99	12.89	13.99
0.6	15.39	13.96	22.29	13.96	12.33	13.85
0.5	16.59	13.82	25.43	13.82	9.697	13.82
0.4	18.60	13.44	31.18	13.44	8.232	13.44
0.3	22.17	12.61	42.98	12.61	6.963	12.61
0.25	25.08	11.96	54.09	11.96	6.471	11.96
0.125	42.42	9.585	150.3	9.585	5.997	9.585

Table 3.4: Coefficients for the contact values of transverse mobilities given by (3.69).

$$-\frac{T_{y_1}}{\pi\mu U_0 a_1^2} = 4\,Y_{11}^{B,\infty}\bar{U}_1 + 8\,Y_{11}^{C,\infty}\bar{\omega}_1 - (4\,Y_{11}^{B,\infty} + 4\,Y_{11}^{C,\infty} + 8Y_{11}^{H,\infty})\bar{E}_\infty\,, \tag{3.72}$$

where a_1 is radius of the sphere, $\bar{E}_\infty = E_\infty a_1/U_0$ is the dimensionless shear rate, and $Y_{11}^{R,\infty}$ are the resistance functions (3.54) corresponding to the limit $\kappa \to \infty$,

$$Y_{11}^{A,\infty} = -\frac{g(q)}{12} + \frac{8}{15}\log\epsilon^{-1} + A_{11}^{Y,\infty} + O(\epsilon\log\epsilon^{-1})\,, \tag{3.73}$$

$$Y_{11}^{B,\infty} = -\frac{g(q)}{8} - \frac{1}{5}\log\epsilon^{-1} + B_{11}^{Y,\infty} + O(\epsilon\log\epsilon^{-1})\,, \tag{3.74}$$

$$Y_{11}^{C,\infty} = -\frac{g(q)}{16} + \frac{2}{5}\log\epsilon^{-1} + C_{11}^{Y,\infty} + O(\epsilon\log\epsilon^{-1})\,. \tag{3.75}$$

$$Y_{11}^{G,\infty} = -\frac{3}{16}g(q) + \frac{7}{10}\log\epsilon^{-1} + G_{11}^{Y,\infty} + O(\epsilon\log\epsilon^{-1})\,. \tag{3.76}$$

$$Y_{11}^{H,\infty} = \frac{3}{32}g(q) - \frac{1}{10}\log\epsilon^{-1} + H_{11}^{Y,\infty} + O(\epsilon\log\epsilon^{-1})\,. \tag{3.77}$$

Here, $\epsilon = h_0/a_1$ is the gap, and $R_{11}^{Y,\infty}$ are the matching constants to the outer solution for this geometry [60, 65].

The translational and rotational mobilities of the particle are determined by the solution of equations (3.71)-(3.72) for problems (I) and (II). The results have the form

of (4.33) with $\lambda_3 = 0$,

$$\bar{V}_1 = \frac{c_0 + c_1 \log \epsilon^{-1} + c_2 g(q)}{c_3 + c_4 \log \epsilon^{-1} + \left[\log \epsilon^{-1} - \frac{5}{12} g(q)\right] \log \epsilon^{-1} + c_5 g(q)}\,, \tag{3.78}$$

where $\bar{V}_1 = \bar{U}_1$ or $\bar{\omega}_1$ and $U_0 = (6\pi\mu a_1)^{-1} F_0$ for problem (I) and $U_0 = E_\infty a_1$ for problem (II). The numerical coefficients appearing in (3.78) are listed in Table 3.5.2 for both problems, and the results are plotted in figure 3.5. The results for impermeable spheres [60, 65, 66] are recovered for $g = 0$, corresponding to $q \gg 1$.

Inserting Eq.(3.46) into (3.78) yields a simplified analytical mobility formula depicted by dashed lines in figure 3.5. Evaluating the result at contact yields,

$$\bar{U}_1 = \bar{\omega}_1 = \frac{d_1}{\log K^{-1} + d_2}\,, \tag{3.79}$$

where $d_1 = 3.125$, $d_1 = 7.280$ for problems (I), (II), respectively, and $d_2 = 6.666$ for both problems. The result indicates that permeable particles roll without slipping at contact, as seen in figure 3.5, and the effect of permeability decays slowly. By contrast, impermeable particles become stationary at contact and exhibit a slipping approach to contact with $\bar{U}_1 > \bar{\omega}_1$ [65, 66].

	$\bar{U}_1$					
Problem	c_0	c_1	c_2	c_3	c_4	c_5
(I)	1.909	2.000	−.3125	1.590	3.1881	−.3008
(II)	2.649	3.716	−.3348	1.590	3.1881	−.3008
	$\bar{\omega}_1$					
	c_0	c_1	c_2	c_3	c_4	c_5
(I)	−.9475	.5000	.3125	1.590	3.1881	−.3008
(II)	.6513	2.109	.3348	1.590	3.1881	−.3008

Table 3.5: Coefficients for particle velocity parallel to wall (3.78).

3.6 Conclusions

A lubrication analysis is presented for permeable spherical particles in the weak permeability regime, $K \ll 1$. Only the mean permeability enters the problem and the size ratio is arbitrary. The complete resistance matrix is derived for transverse motions complementing the recent axisymmetric analysis [55]. Near-contact mobilities depend on gap width, size ratio, and permeability.

Mobilities describing axisymmetric relative particle motion have a universal near-contact behavior described by a universal function $f(q)$ multiplied by a function of size ratio, where $q = K^{2/5}h_0/a$, and $f(q)$ is described elsewhere [55]. Axisymmetric mobilities approach a non-vanishing values at contact, proportional to $K^{2/5}$. By contrast to impermeable particles, contact occurs in finite time under the action of a constant force.

Particle permeability enhances near-contact, transverse relative motion because it releases some of the lubrication pressure. Resistances for permeable particles are given by the classical resistance functions for impermeable particles plus the product of a universal one-parameter function, $g(q)$, times a rational function of size ratio. The function $g(q)$ is obtained by solving an integro-differential form of the Reynolds lubrication equation. Even very small values of permeability can be significant because its effect decays logarithmically. Relative particle motions that do not generate pressure are unaffected by particle permeability, e.g., dumbbell rotation of the particle pair. Permeability qualitatively alters particle mobility for extreme size ratios, providing access to non-singular rolling motion. A permeable particle in point-contact with a planar boundary rolls without slipping under the action of a constant force with a velocity that varies inversely with $\log K^{-1}$. This also occurs for a particle subjected to an imposed shear flow tangent to the boundary. This finding may have relevance to cross-flow particle filtration.

Note

The authors are grateful to Dr. A. Z. Zinchenko [63] for the use of his bispherical coordinate code for computing pair mobilities of impermeable spheres, and to Dr. D. J. Jeffrey [67] for the use of his program available online for resistance functions used herein to obtain the matching constants for the resistance functions of impermeable spheres.

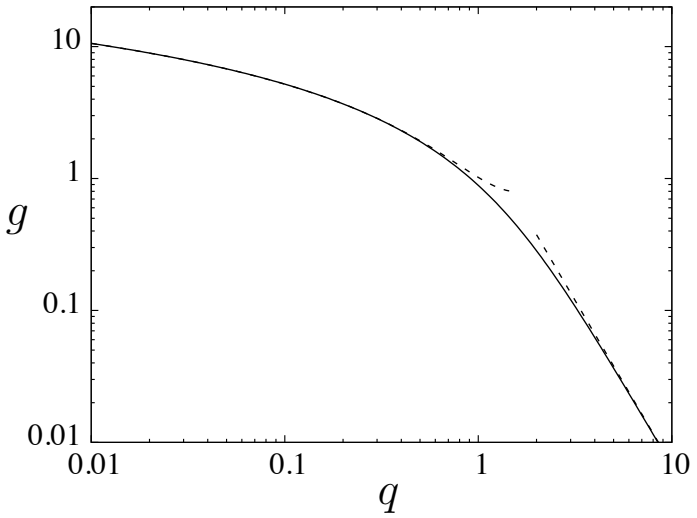

Figure 3.2: Permeability integral $g(q)$, defined by Eq. (3.34); numerical solution (solid curve) and asymptotic limits (3.46)-(3.47) (dashed curves).

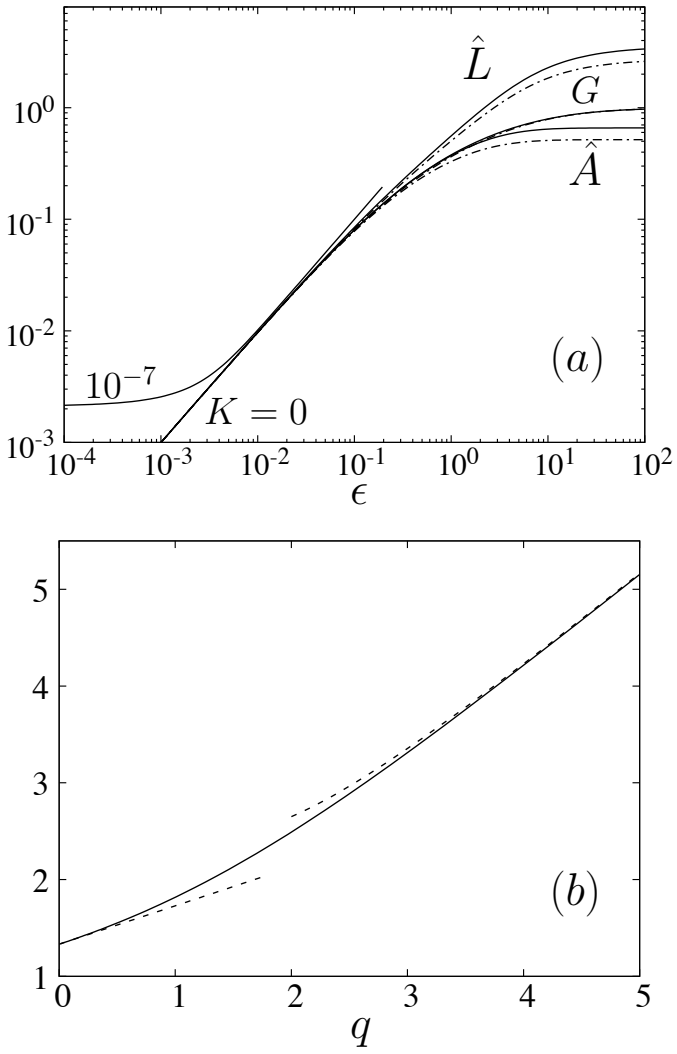

Figure 3.3: (a) Axisymmetric mobility functions $G, \hat{A}_1$, and $\hat{L}$ ($\gamma = 1$) from exact bispherical coordinate solution [63] versus gap, ϵ, for size ratios $\kappa = 0.5$ (solid lines), $\kappa = 0.75$ (dash-dotted lines) (curves for $\kappa = 0.5$, and $\kappa = 0.75$ are indistinguishible for G); lubrication solution for $K = 0$, and $K = 10^{-7}$ (solid lines); (b) universal near-contact behavior (3.67) versus permeability parameter, q; small- and large-q asymptotes given by Eqs. (3.64)-(3.65) (dashed lines).

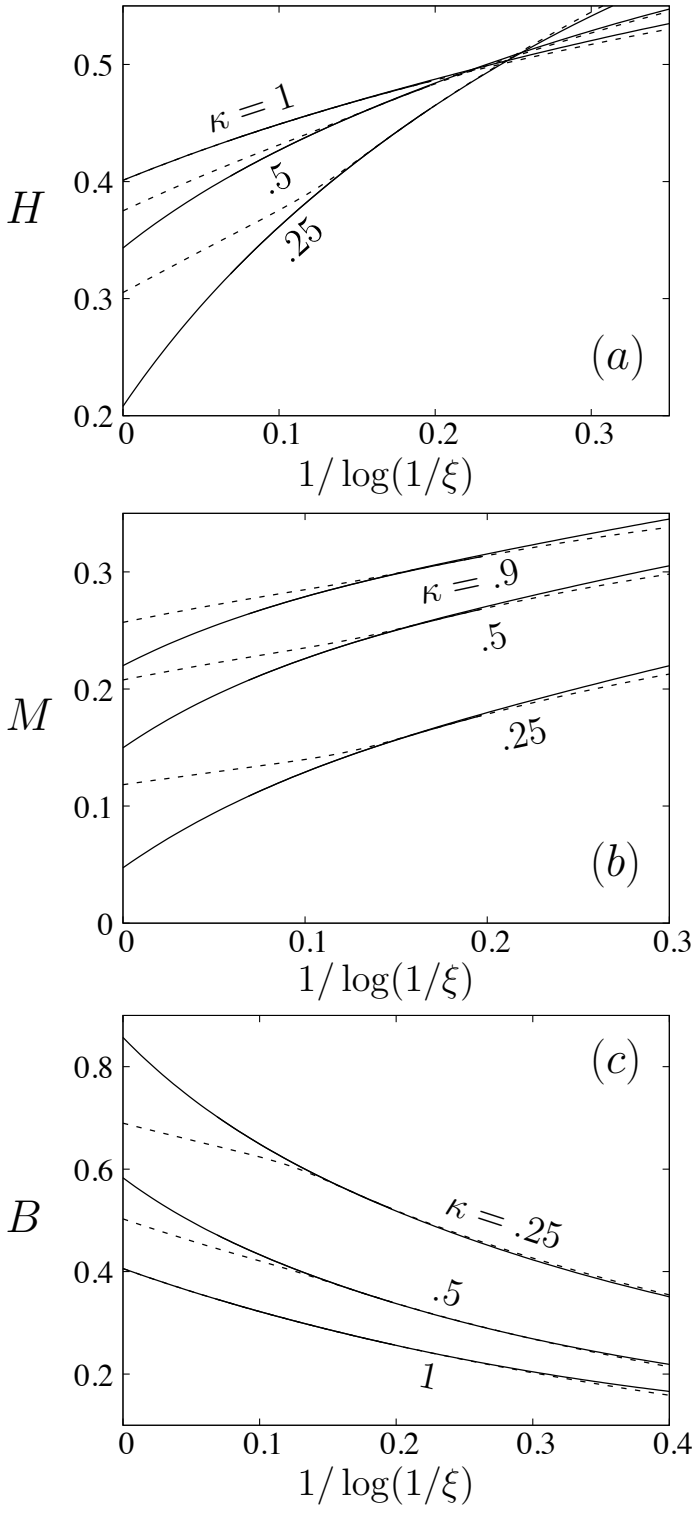

Figure 3.4: Transverse mobility functions H (a), M ($\gamma = 1$) (b), and B (c) from exact bispherical coordinate solution [63] (solid lines) and lubrication solutions for $K = 0$ and $K = 10^{-7}$ (dashed lines) versus gap, ξ, for size ratios indicated.

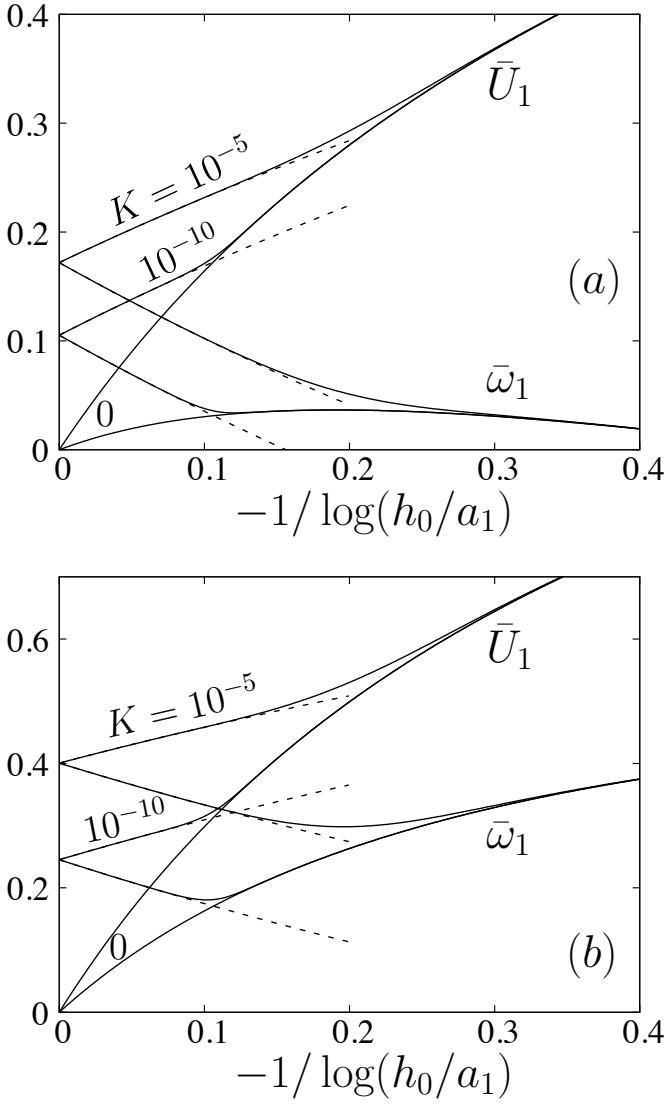

Figure 3.5: Translational and rotational velocities of a particle moving parallel to a plane wall under the action of a force (a), and in shear flow (b); mobility formula (3.78) (solid lines); simplified mobility formula for $q \ll 1$ obtained by inserting Eq. (3.46) into (3.78) (dashed lines); permeabilities as labelled.

Chapter 4

Collision rates of permeable particles in Brownian motion, gravity sedimentation, and linear flows

4.1 Introduction

The aggregation of particles suspended in fluids has been the subject of intense theoretical and practical investigations for over a century. Examples of applications encompass deep-bed granular filtration [6], rain-drop formation [68, 69], and particle coagulation in marine environments, e.g. marine"snow" [9, 70, 71]. A fundamental description of the rates of particle encounters is crucial in properly characterizing the resulting suspension stability and particle microstructure.

The rate of coagulation in a dilute dispersion of impermeable particles was first investigated by Smoluchoswski in 1917 [72] who proposed a model for analyzing interparticle encounters, neglecting hydrodynamic interactions and assuming a sticking

force at contact. Fuchs [73] proposed a correction to Smoluchowski's model for electrically charged aerosol particles. Spielman [74], Valioulis & List [75], and Kim & Zukoski [76] analyzed perikinetic (Brownian) coagulation of spherical colloidal particles, accounting for pairwise hydrodynamic interactions and non-hydrodynamic interparticle forces, such as van der Waals attraction and electrostatic repulsion.

Curtis & Hocking [77], Arp & Mason [78], Zeichner & Schowalter [79], Van de Ven & Mason [80], and Adler [81] studied orthokinetic coagulation: particle coagulation in suspensions undergoing prescribed flows, including shear flow, and uniaxial straining flow. Particle coagulation in more general flows has also been considered [82–84]. In these studies, pairwise hydrodynamic interactions and non-hydrodynamic interparticle forces [85] were incorporated in a trajectory analysis [61, 62, 86–88]. Coagulation of sedimenting particles has also been analyzed using trajectory calculations that incorporate hydrodynamic interactions and interparticle forces [89–92].

The foregoing analyses only consider pairwise particle interactions, thus their application is limited to semi-dilute suspensions. Pairwise coagulation rates are usually expressed in dimensionless form as a collision efficiency, E, i.e., the rate of coagulation normalized by the coagulation rate in the absence of hydrodynamic and non-hydrodynamic forces (i.e., as predicted by the Smoluchowski's theory [72]); stability ratio is defined as the reciprocal of the collision efficiency, E^{-1}.

Davis and co-workers investigated the effects of hydrodynamic interactions and interparticle forces on the collision efficiency of spherical drops in Brownian motion, sedimentation [93], linear flows [94, 95], and particle flotation by bubbles or drops [96]. These studies show that interfacial mobility significantly enhances the collision efficiency of drops compared to rigid particles.

The analyses in most of the foregoing studies is relegated to either the small- or large-Peclet number limit. Exceptions include Zinchencko & Davis [97] and Bal [98,99] who investigated coagulation rates in colloidal suspensions by the combination of

Brownian motion and shear flow at arbitrary Peclet numbers, and Zinchenko & Davis [100] and Ramirez *et.al.* [101] who evaluated coagulation rates by the combination of Brownian motion and sedimentation at arbitrary Peclet number.

Due to the classical lubrication singularity for vanishing surface-to-surface separations, $h_0 \to 0$ (i.e., contact), collisions between smooth spherical (impermeable) particles are possible only in the presence of material-specific non-hydrodynamic attractive forces (e.g. van der Waals forces), or generic physical phenomena, including surface roughness or particle permeability [55] that lead to a break-down of the lubrication singularity at contact.

Particles with surface roughness amplitude δa are usually treated as impermeable spheres, where the surface-to-surface separation is restricted according to $h_0 \geq \delta a$, contact occurs at $h_0 = \delta a$, and the roughness amplitude is assumed to be small compared to the particle size, $\delta \ll 1$ [49, 64, 102]. Two limits for the coefficient of contact friction have been considered: zero and infinite, corresponding respectively, to perfect slip and no-slip, but the results are insensitive to this choice [50, 103] because the viscous transverse lubrication resistance dominates the contact friction.

The collision efficiency of permeable particles date back to 1967 when Sutherland [104] proposed a geometric model for the formation of high-porosity aggregates based on Smoluchowski's diffusion equation. Following this previous work, a significant body of research has been focused on aggregate formation and collision rates of particle aggregates (flocs) that are usually modeled as fractals with highly-porous structure. Generally, Brinkman's equation [54] is favored for describing the flow inside highly porous aggregates [20–22, 39]. Neale et al. [105] proposed a correction factor to the Stokes drag on a settling permeable sphere to account for permeable effects and examined the assumption that an isolated high-porosity aggregate may be modeled as an impermeable body [106]. Adler [107] analyzed streamlines using Brinkman's equation for the flow inside permeable spheres to predict aggregation-disaggregation

dynamics. Further theoretical and experimental works on the aggregation kinetics of fractal aggregates with radially varying permeability showed that collision efficiencies decreased with the fractal dimension while the viscous drag increased [108–111].

Bäbler et al. [44] used the method of reflections [42] to study the pairwise hydrodynamic interactions of high-porosity aggregates in linear flows using Brinkman's equation to describe flow inside the aggregate. Collision efficiencies were estimated from a trajectory analysis with and without van der Waals forces. The same author used the foregoing trajectory analysis scheme to explore the collision efficiency of aggregates accounting for fractal dimension, internal structure, and interparticle forces [112]. Near-field and lubrication interactions were unresolved in these studies, and perhaps justified, by the restriction to high particle porosities.

Problems involving thin permeable layers or membranes have been extensively studied [31, 32, 34–36, 113], including the collision efficiency for particles captured by drops with a permeable interface [114]. In these problems, the thin permeable layer reduces to a normal velocity boundary condition. Core-shell particles comprised of a comparatively thin, highly-porous shell and impermable core have been analyzed using Brinkman's equation to describe the fluid flow in the shell [45, 46], and collision efficiencies have been calculated [115].

Most of the above studies focus on the high-porosity regime, relevant to particle flocs, and thin permeable layers that reduce to a boundary condition for the velocity. Darcy's law [19] is more appropriate for describing the flow inside the particles with moderate and low permeabilities. While Brinkman's equation is compatible with no-slip boundary conditions, slip-velocity boundary conditions [25, 26, 28] are appropriate for Darcy's law although no-slip boundary conditions are often used. Hydrodynamic pair interactions between particles with moderate permeabilities have been computed in bispherical coordinates, using Darcy's law to describe the flow inside the particles, and applying slip-velocity boundary conditions on particle surfaces. [40, 41, 43].

Reboucas & Loewenberg [55, 116] developed a lubrication analysis for permeable spheres in close contact, $h_0/a \ll 1$, under weak permeability conditions,

$$K = k/a^2 \ll 1\,. \tag{4.1}$$

Here, h_0 is the surface-to-surface separation, $a = a_1 a_2 (a_1 + a_2)^{-1}$ is the reduced radius, k is the mean permeability of the particles,

$$k = \frac{1}{2}\left(k_1 + k_2\right)\,, \tag{4.2}$$

and K is the dimensionless permeability. Their analysis showed that axisymmetric mobilities for weakly permeable particles are qualitatively affected for gap widths $h_0/a = O(K^{2/5})$, and, by contrast with impermeable spheres, have non-zero $O(K^{2/5})$ contact values. Accordingly, particle contact is predicted to occur in finite time under the action of a constant force, leading to finite collision efficiencies even in the absence of non-hydrodynamic forces or surface roughness. This is partially off-set by the discovery that permeability causes particles to spend less time in close contact because transverse hydrodynamic interactions are also reduced [116].

The weak permeability limit, $K \to 0$, is singular. Particle permeability affects trajectories at $O(1)$ within a thin, $O(K^{2/5})$ boundary layer that forms in the near-contact region, but has only an $O(K)$ effect for $h_0/a \gg K^{2/5}$. Surface roughness is an analogous physical phenomenon that circumvents the lubrication singularity and forms a δ-thickness boundary layer in the zero-roughness-limit. These situations are similar to the $O(A_H/\mu a^2 U_{12}^{\infty})^{1/2}$ thickness boundary layer that forms in the near-contact region for impermeable particles in limit of weak van der Waals forces, $A_H \to 0$, where A_H is the Hamaker constant, U_{12}^{∞} is the relative velocity of the particles at large separations, a is the particle size, and μ is the fluid viscosity [90, 117].

In this chapter, the collision efficiency of permeable particles is analyzed for aggre-

gation in Brownian motion, gravity sedimentation, uniaxial straining flow, and shear flow, each separately considered. Weak permeability conditions (4.1) are assumed. Darcy's law is used to describe the intraparticle flow, and no-slip boundary conditions are applied at the particle surfaces. Collision efficiencies are derived for spheres with small-amplitude surface roughness and the two problems are shown to be analogous through the definition of an equivalent roughness for permeable particles. The resulting formulas provide accurate closed-form analytical approximations for the collision efficiencies of permeable spheres. The focus here is on the physical mechanism of particle permeability thus van der Waals attraction is included only for collision efficiencies in Brownian motion and neglected in calculations of collision efficiencies in flow and sedimentation under the assumption of large Peclet numbers. The problem is formulated in §2 and the assumptions are discussed. Collision efficiency formulas are derived for permeable particles in §3 and for rough particles in §4. The results are graphically presented and discussed in §5.

4.2 Problem formulation

In a dilute suspension, the pair-distribution function, p_{12}, is governed by the steady-state Fokker-Plank equation,

$$\boldsymbol{\nabla}\cdot\left(p_{12}\boldsymbol{V}_{12}\right)=0\,, \tag{4.3}$$

where $\boldsymbol{V}_{12}$ is the relative velocity of the particles. Particles are assumed to aggregate on contact thus $p_{12}=0$ on a spherical contact surface with radius $r=a_1+a_2$, where a_1 and a_2 are the particle radii; far from the contact surface, $p_{12}=1$.

The relative velocity of the particles is given by [61, 62],

$$\begin{aligned}\mathbf{V}_{12} &= -D_{12}^{(0)}\left[G(s)\hat{\mathbf{r}}\hat{\mathbf{r}} + H(s)\left(\mathbf{I}-\hat{\mathbf{r}}\hat{\mathbf{r}}\right)\right]\cdot\boldsymbol{\nabla}\left(\log p_{12}(\mathbf{r}) + \frac{\Phi_{12}(s)}{k_BT}\right)\\ &\quad + \left[L(s)\hat{\mathbf{r}}\hat{\mathbf{r}} + M(s)\left(\mathbf{I}-\hat{\mathbf{r}}\hat{\mathbf{r}}\right)\right]\cdot\mathbf{V}_{12,g}^{(0)}\\ &\quad + \mathbf{E}_\infty\cdot\mathbf{r} + \boldsymbol{\omega}_\infty\times\mathbf{r} - \left[A(s)\hat{\mathbf{r}}\hat{\mathbf{r}} + B(s)\left(\mathbf{I}-\hat{\mathbf{r}}\hat{\mathbf{r}}\right)\right]\cdot\mathbf{E}_\infty\cdot\mathbf{r}\,. \end{aligned} \tag{4.4}$$

Here, $\mathbf{r} = \mathbf{r}_2 - \mathbf{r}_1$ is the vector between the particle centers, $\hat{\mathbf{r}} = \mathbf{r}/|\mathbf{r}|$ is a unit vector along the line-of-centers, $\mathbf{I}$ is the identity tensor, and $s = |\mathbf{r}|/\bar{a}$ is the center-to-center separation normalized by the average radius (4.10). The quantities $\mathbf{E}_\infty$ and $\boldsymbol{\omega}_\infty$ are the imposed rate-of-strain and vorticity in the fluid. The quantities k_B and T are Boltzmann's constant and absolute temperature; Φ_{12} is the interparticle potential. The quantities $D_{12}^{(0)}$ and $\mathbf{V}_{12,g}^{(0)}$ are, respectively, the Stokes-Einstein-Sutherland relative diffusivity and gravitational particle velocities in the absence of hydrodynamic interactions (i.e., $s \to \infty$),

$$D_{12}^{(0)} = k_BT\left(m_1^{(0)} + m_2^{(0)}\right), \qquad \mathbf{V}_{12,g}^{(0)} = \left|\mathbf{F}_{1,g}m_1^{(0)} - \mathbf{F}_{2,g}m_2^{(0)}\right|, \tag{4.5}$$

where

$$m_i^{(0)} = \frac{1+K_i}{6\pi\mu a_i} \qquad (i=1,2) \tag{4.6}$$

are the hydrodynamic mobilities of isolated permeable particles in Stokes flow with no-slip boundary conditions, and

$$\mathbf{F}_{i,g} = \frac{4\pi}{3}a_i^3\Delta\rho\,\mathbf{g} \qquad (i=1,2) \tag{4.7}$$

are the net gravity forces acting on the particles. Here, k_i are the particle permeabilities and $K_i = k_i/a_i^2$ are the dimensionless permeabilities, μ is the fluid viscosity, $\Delta\rho$ is the excess particle density (assumed the same for both particles), and $\boldsymbol{g}$ is the

acceleration of gravity.

Equation (4.4) defines the pairwise axisymmetric and transverse mobility functions G, L, A and H, M, B, respectively. According to their definitions, G, H, L and M tend to unity at large separations, whereas A and B vanish for $s \to \infty$. The pair mobilities depend on the center-to-center separation s, particle permeabilities K_i $(i = 1, 2)$, and size ratio $\kappa = a_2/a_1$. The linear superposition inherent in the form of the relative particle velocity (4.4) is predicated on the assumption of small Reynolds numbers,

$$\mathrm{Re} = \frac{\rho V_{12}^{(0)} a}{\mu} \ll 1 \,, \tag{4.8}$$

where $V_{12}^{(0)} = |\mathbf{V}_{12}^{(0)}|$, and ρ is the fluid density.

For the weak permeability regime $K \ll 1$ considered herein, particle mobilities are affected only by the mean permeability (4.1) in the near-contact region and are equal to the mobilities of impermeable particles outside of this region. Impermeable particles with small-amplitude surface roughness, $\delta \ll 1$, will also be analyzed because of the useful analogy it provides. In this case, impermeable mobility functions apply everywhere away from the contact surface at $r = a_1 + a_2 + \delta a$, where a is the reduced radius (4.11). For either of these cases, isolated mobilities for impermeable spheres, $(6\pi\mu a_i)^{-1}$ $(i = 1, 2)$, can be used in place of the isolated mobilities for permeable spheres (4.6). Accordingly, (4.5) simplifies to

$$D_{12}^{(0)} = \frac{k_B T}{6\pi\mu a} \,, \qquad \mathbf{V}_{12,g}^{(0)} = \frac{2\,(a_1^2 - a_2^2)\,\Delta\rho\,\mathbf{g}}{9\mu} \,. \tag{4.9}$$

Different length normalizations are convenient in different contexts. For conve-

nience, these are summarized here. The average and reduced radius are defined

$$\bar{a} = \frac{1}{2}\left(a_1 + a_2\right) = \frac{1}{2}a_1\left(1+\kappa\right)\,, \tag{4.10}$$

$$a = a_1 a_2 \left(a_1 + a_2\right)^{-1} = a_1\kappa\left(1+\kappa\right)^{-1} = \nu\bar{a}\,, \tag{4.11}$$

where $\kappa = a_2/a_1$ denotes the size ratio and ν is the conversion factor between the average and reduced radius which arises in the analysis to follow,

$$\nu = \frac{a}{\bar{a}} = 2\kappa\left(1+\kappa\right)^{-2}\,. \tag{4.12}$$

The center-to-center separation r and surface-to-surface separation h_0 are both relevant, and two corresponding dimensionless lengths are used,

$$s = \frac{r}{\bar{a}}\,, \tag{4.13}$$

and

$$\epsilon = \frac{h_0}{a}\,; \qquad \xi = s - 2 = \frac{h_0}{\bar{a}} = \nu\epsilon\,. \tag{4.14}$$

4.2.1 Van der Waals attraction

Herein, consideration of interparticle forces is limited to the unretarded van der Waals potential [118],

$$\Phi_{12} = A_H\bar{\Phi}_{12}\,, \tag{4.15}$$

where A_H is the Hamaker constant, and $\bar{\Phi}_{12}$ is the dimensionless potential,

$$\bar{\Phi}_{12}(s) = -\frac{1}{6}\left(\frac{8\kappa}{(\kappa+1)^2\left(s^2-4\right)} + \frac{8\kappa}{(\kappa+1)^2 s^2 - 4(1-\kappa)^2} + \log\left[\frac{(\kappa+1)^2\left(s^2-4\right)}{(\kappa+1)^2 s^2 - 4(1-\kappa)}\right]\right)\,, \tag{4.16}$$

which has the singular form at contact,

$$\bar{\Phi}_{12}(\xi) = -\frac{\nu}{6\xi} + O(\log \xi)\,, \qquad \xi \ll 1\,, \tag{4.17}$$

where κ, ξ, and ν are defined above.

The dimensionless Hamaker parameter,

$$\bar{A}_H = A_H/k_B T\,. \tag{4.18}$$

characterizes the relative strength of van der Waals attraction in Brownian motion; typically $\bar{A}_H = O(1)$. The relative strength of van der Waals interactions for non-diffusing particles, aggregating under gravity-driven sedimentation or in a prescribed flow, is characterized by the parameter Q_H which is related to the Peclet number,

$$Q_H = \frac{Pe}{\bar{A}_H}\,, \qquad \mathrm{Pe} = \frac{\mu V_{12}^{(0)} a^2}{k_B T}\,, \tag{4.19}$$

where $V_{12}^{(0)}$ is given by (4.9) for sedimentation and $V_{12}^{(0)} = E_\infty a$ for particles in flow, where E_∞ is the imposed strain-rate. Often, $\mathrm{Pe} \gg 1$ and thus $Q_H \gg 1$. Consider, for example, 30μm particles in a fluid with viscosity $\mu = .01$ Pa $\cdot$ s with $\bar{A} \approx 1$ for two situations: (i) sedimenting in normal gravity with $\Delta\rho/\rho = 2$, and (ii) in shear flow with shear-rate $E_\infty = 10$ s^{-1}. For both of these cases, $Q_H \approx 10^6$ (and $\mathrm{Re} \approx .001$, where the Reynolds number is defined by Eq. (4.8)).

Even for $Q_H \gg 1$, van der Waal attraction can be important because of its singular behavior (4.17). Balancing the $O(\mu V_{12}^{(0)} a)$ viscous and $O(A_H a h_0^{-2})$ van der Waals forces acting on particles in close-contact yields the $O(A_H/\mu a^2 U_{12}^\infty)^{1/2}$ boundary layer associated with weak van der Waals attraction [90, 117]. Comparing to the $O(K^{2/5})$ boundary layer associated with particle permeability [55] indicates that van der Waals

attraction is negligible if

$$K \gg Q_H^{-5/4}\,. \tag{4.20}$$

Van der Waals attraction is included in our analysis of aggregation in Brownian motion because $\bar{A}_H = O(1)$ is typical. However, van der Waals attraction is omitted in our collision efficiency calculations for non-diffusing particles aggregating under sedimentation or in an imposed flow under the assumption that Eq. (4.20) holds. Herein, the focus is on permeability and surface roughness as physical mechanisms that give rise to non-zero collision rates in the absence of non-hydrodynamic forces. The complimentary regime of particle collisions mediated by colloidal forces has been the subject of numerous classical investigations, such as those discussed in the Introduction.

4.2.2 Collision efficiencies

In this section, pairwise aggregation rates are defined and the classical formulas for collision efficiencies, given in terms of pair mobility functions, are recalled for particles in Brownian motion, gravity sedimentation, and in imposed uniaxial straining and shear flows; each case is separately considered.

The pairwise aggregation rate of particles J_x is given by the integral of the flux over the contact surface at $r = r_c$,

$$J_x = -n_1 n_2 \int_{r_c} p_{12} \boldsymbol{V_{12}} \cdot \boldsymbol{n}\, dS \tag{4.21}$$

where $r_c = a_1 + a_2 + \delta a$ for particles with surface roughness, otherwise $r_c = a_1 + a_2$. Here, n_i $(i = 1, 2)$ are the upstream number densities of the particles, and subscript $x = B, g, st, sh$, respectively, will be used to denote aggregation in Brownian motion, gravity sedimentation, straining flow, and shear flow. Collision efficiencies are defined

as

$$E_x = J_x / J_x^{(0)} \,, \tag{4.22}$$

where $J_x^{(0)}$ is the aggregation rate in the absence of hydrodynamic interactions (i.e., $G = H = L = M = 1$ & $A = B = 0$). Collision rates under these conditions are given by [72]

$$J_B^{(0)} = 4\pi n_1 n_2 D_{12}^{(0)} (a_1 + a_2) \,, \qquad J_g^{(0)} = n_1 n_2 V_{12,g}^{(0)} \pi (a_1 + a_2)^2 \tag{4.23a,b}$$

for aggregation in Brownian motion and gravity sedimentation, and

$$J_{st}^{(0)} = \frac{8\pi}{3\sqrt{3}} n_1 n_2 E_\infty (a_1 + a_2)^3 \,, \qquad J_{sh}^{(0)} = \frac{4}{3} n_1 n_2 E_\infty (a_1 + a_2)^3 \tag{4.24a,b}$$

for aggregation in uniaxial straining flow and shear flow. Here, $D_{12}^{(0)}$ and $V_{12,g}^{(0)}$ are given by Eq. (4.9), and E_∞ is the imposed strain-rate.

Collision efficiencies are obtained for each aggegration mechanism, by appropriately simplifying the relative particle velocity (4.4), inserting it into Eq. (4.3), and integrating with with boundary conditions,

$$p_{12}(s_c) = 0 \,, \quad \text{and} \quad p_{12}(\infty) = 1 \,, \tag{4.25}$$

where $s_c = r_c / \bar{a}$.

The collision efficiency for Brownian motion is obtained by simplifying Eq. (4.4) for neutrally-buoyant particles in a quiescent fluid (i.e., $V_{12,g}^{(0)} = \mathbf{E}_\infty = \boldsymbol{\omega}_\infty = 0$). Integrating the resulting radial velocity in Eq. (4.3) and applying boundary conditions (4.25) yields [74],

$$E_B = 1 / I_B(s_c) \,, \qquad I_B(s) = 2 \int_s^\infty \frac{e^{\bar{A}_H \bar{\Phi}(s)}}{s^2 G(s)} ds \,. \tag{4.26a,b}$$

As indicated, van der Waals attraction is retained in the above formula for the binary collision efficiency of particles in Brownian motion. The formulas below for collision efficiencies in sedimentation and linear flows are derived with van der Waals attraction omitted, as discussed in §4.2.1.

The collision efficiency for gravity sedimentation is obtained by inserting Eq. (4.4) simplified for non-diffusing particles in a quiescent fluid (i.e., $D_{12}^{(0)} = \mathbf{E}_\infty = \boldsymbol{\omega}_\infty = 0$) into Eq.(4.3). Dividing the resulting components of the relative velocity normal, and parallel, to the line-of-centers, and integrating the critical trajectory upstream from the equator of the contact surface to determine the radius of the upstream collision cross-section, yields [62, 90]

$$E_g = e^{2I_g(s_c)}\,, \qquad I_g(s) = \int_s^\infty \frac{L(s) - M(s)}{L(s)} \frac{ds}{s}\,. \tag{4.27a,b}$$

The collision efficiency for uniaxial straining flow is similarly obtained after inserting Eq. (4.4), simplified for non-diffusing, neutrally-buoyant particles in an axisymmetric flow (i.e., $D_{12}^{(0)} = V_{12,g}^{(0)} = \boldsymbol{\omega}_\infty = 0$), into Eq.(4.3). The result is [61, 87, 94],

$$E_{st} = e^{-3I_{st}(s_c)}\,, \qquad I_{st}(s) = \int_s^\infty \frac{A(s) - B(s)}{1 - A(s)} \frac{ds}{s}\,. \tag{4.28a,b}$$

A more complicated picture arises in shear flow due to the existence of nearby recirculating (closed) particle trajectories that do not contribute to particle aggregation at steady-state and must be subtracted from the net particle flux on the contact surface. The collision efficiency in this case is given by [94]

$$E_{sh} = \left(e^{-2I_{st}(s_c)} - I_{sh}(s_c)\right)^{3/2}\,, \qquad I_{sh}(s) = \frac{1}{4}\int_s^\infty e^{-2I_{st}} \frac{B(s)}{1 - A(s)}\, s\, ds\,, \tag{4.29a,b}$$

where $e^{-2I_{st}} - I_{sh} > 0$ is assumed; for $e^{-2I_{st}} - I_{sh} \le 0$, $E_{sh} \equiv 0$.

4.2.3 Permeable particles

For permeable particles, the pairwise mobilities that appear in Eq. (4.4) depend on particle separation, size ratio, and the permeability parameter q,

$$q = \epsilon K^{-2/5} = \nu^{-1}\xi K^{-2/5}\,, \tag{4.30}$$

where, K is the dimensionless mean permeability, and ϵ is the dimensionless gap (4.14).

Under weak permeability conditions (4.1), particle mobilities are approximately the same as those for impermeable particles with $O(K)$ error for $q \gg 1$, but they are qualitatively altered for $q = O(1)$. The near-contact axisymmetric mobilities for permeable particles exhibit a simplified, separable dependence on permeability [116],

$$G_\xi = \nu^{-1}\frac{\xi}{f(q)}\,, \qquad L_\xi = R_g(\kappa)\,\frac{\xi}{f(q)}\,, \qquad A_\xi = 1 - R_{st}(\kappa)\,\frac{\xi}{f(q)}\,, \qquad (4.31a,b,c)$$

where R_g and R_{st}, respectively, are dimensionless contact resistances that arise for particles in point-contact migrating parallel to their line-of-centers in gravity and uniaxial straining flow. The function $f(q)$ is the numerical solution of an axisymmetric Reynolds lubrication equation [55] that has the asymptotic properties,

$$f(q) = c_1 q - c_2 q^2 + O(q^2), \quad q \ll 1\,; \qquad f(q) = 1 - \,c_3\, q^{-5/2} + O(q^{-5}), \quad q \gg 1\,, \tag{4.32a,b}$$

where $c_1 \doteq .7507$, $c_2 \doteq .224$, and $c_3 \doteq 1.8402$. Inserting Eqs. (4.30) and (4.32a) into Eq. (4.31) reveals that the axisymmetric mobilities of permeable particles have non-zero $O(K^{2/5})$ contact values by contrast to impermeable particles [116]. This is why permeable particles can aggregate even in the absence of interparticle forces.

The transverse mobilities M and B have the lubrication forms

$$M_\xi = \frac{m_1 + m_2 \log \xi^{-1} + m_3 \left[\log \xi^{-1} - \frac{5}{12} g(q)\right] \log \xi^{-1} + m_6 g(q)}{m_4 + m_5 \log \xi^{-1} + \left[\log \xi^{-1} - \frac{5}{12} g(q)\right] \log \xi^{-1} + m_7 g(q)}\,, \tag{4.33a}$$

$$B_\xi = \frac{b_1 + b_2 \log \xi^{-1} + b_3 \left[\log \xi^{-1} - \frac{5}{12} g(q)\right] \log \xi^{-1} + b_6 g(q)}{b_4 + b_5 \log \xi^{-1} + \left[\log \xi^{-1} - \frac{5}{12} g(q)\right] \log \xi^{-1} + b_7 g(q)}\,, \tag{4.33b}$$

where the coefficients m_i and b_i (i = 1-9) depend on size ratio. The function $g(q)$ is the numerical solution of a transverse Reynolds lubrication equation [116] with the asymptotic properties,

$$g(q) = -\frac{12}{5} \log q + c_4 + O(q), \quad q \ll 1\,; \qquad g(q) = c_5 q^{-5/2} + O\left(q^{-5}\right), \quad q \gg 1, \tag{4.34a, b}$$

with $c_4 \doteq -0.48$ and $c_5 \doteq 2.12$. Inserting the limiting result (4.34a) for $q \to 0$ into Eq. (4.33), yields permeability-dependent contact values for the transverse mobilities [116].

The lubrication forms of the classical mobility functions are

$$G_{\xi,0} = \nu^{-1} \xi\,, \qquad L_{\xi,0} = R_g(\kappa)\, \xi\,, \qquad A_{\xi,0} = 1 - R_{st}(\kappa)\, \xi\,, \tag{4.35a, b, c}$$

and

$$M_{\xi,0} = \frac{m_1 + m_2 \log \xi^{-1} + m_3 \log^2 \xi^{-1}}{m_4 + m_5 \log \xi^{-1} + \log^2 \xi^{-1}}\,, \tag{4.36a}$$

$$B_{\xi,0} = \frac{b_1 + b_2 \log \xi^{-1} + b_3 \log^2 \xi^{-1}}{b_4 + b_5 \log \xi^{-1} + \log^2 \xi^{-1}}\,. \tag{4.36b}$$

These results are recovered from formulas (4.31) and (4.33) by setting $f = 1$ and $g = 0$, corresponding to $q \to \infty$, according to Eqs. (4.32 b) and (4.34 b).

Away from the near-contact region, the particle mobilities are approximated by the mobilities of impermeable particles, denoted by G_0, L_0, A_0, M_0, B_0, under the assumption of weak permeablity, as discussed above.

4.3 Collision efficiency formulas for permeable particles

In this section, a leading-order asymptotic formulation is presented for the computation of collision efficiencies of weakly permeable particles. Collision efficiencies are determined by the values of the collision efficiency integrals (4.26)-(4.29) on the contact surface at $s = 2$. The formulation employs a uniformly valid approximation of the integrands in Eqs. (4.26b)-(4.29b) for $K \ll 1$. The resulting collision efficiencies are given by a quadrature of lubrication approximations for the mobility functions of permeable particles in the near-contact region, and size-ratio-dependent parameters are derived from standard hard-sphere mobilities. Details of the generic derivation are provided in Appendix C.1, and the procedure for evaluating the formulas is provided in Appendix C.2.

4.3.1 Collision efficiency for Brownian motion

The binary collision efficiency for permeable particles undergoing Brownian motion is given by Eq. (4.26). The collision efficiency integral I_B is evaluated on the contact surface by the procedure described in Appendix C.1.1. For integral (4.26b), the required functions are

$$Q(s) = G(s)\,, \qquad P(s) = \frac{2e^{\bar{A}_H \bar{\Phi}(s)}}{s^2}\,, \tag{4.37a,b}$$

and correspondingly, by Eqs. (4.31a) and (4.17),

$$Q_\xi = \frac{\nu^{-1}\xi}{f(q)}\,, \qquad P_\xi = \frac{e^{-\frac{\nu \bar{A}_H}{6\xi}}}{2}\,. \tag{4.38a,b}$$

The corresponding function, G_0, for impermeable spheres is also required, and in the lubrication regime is given by Eq. (4.35a). The required indefinite integral (C.1.11) is

$$F_B(x) = \nu \int_0^x e^{-\frac{\nu \bar{A}_H}{6\xi}} \frac{d\xi}{2\xi} = \frac{\nu}{2} E_1 \left(\frac{\nu \bar{A}_H}{6x} \right) , \tag{4.39}$$

where $E_1 = \int_x^\infty e^{-t} dt/t$ is the exponential integral.

Inserting Eqs. (4.37)-(4.39) into Eq. (C.1.12) and the result into Eq. (4.26) yields the collision efficiency,

$$E_B^{(k)} = \left[\Gamma_B + \Lambda_B^{(0)} - \frac{\nu}{2} E_1(A_k) \right]^{-1} , \tag{4.40}$$

where

$$\Gamma_B = \lim_{\xi \to 0} \left[\int_\xi^\infty \frac{2 e^{\bar{A}_H \bar{\Phi}(t)}}{(2+t)^2 G(t)} dt + \frac{\nu}{2} E_1 \left(\frac{\nu \bar{A}_H}{6\xi} \right) \right] , \tag{4.41}$$

$$= \int_0^\infty \frac{2 e^{\bar{A}_H \bar{\Phi}(t)}}{(2+t)^2 G(t)} dt \, , \qquad \bar{A}_H > 0 \, , \tag{4.42}$$

and

$$\Lambda_B^{(0)} = \frac{\nu}{2} \left[\int_1^\infty e^{-A_k/q} \left[f(q) - 1 \right] \frac{dq}{q} + \int_0^1 e^{-A_k/q} f(q) \frac{dq}{q} \right] . \tag{4.43}$$

Here, the parameter A_k is the modified Hamaker parameter for permeable particles,

$$A_k = \frac{\bar{A}_H}{6 K^{2/5}} \, . \tag{4.44}$$

For $A_k \ll 1$, Eqs. (4.37b), (4.38b) and (4.39) reduce to

$$P(s) = \frac{2}{s^2} \, , \qquad P_\xi = \frac{1}{2} \, , \tag{4.45a, b}$$

and

$$F_{B,0}(x) = \frac{\nu}{2} \log x \,, \tag{4.46}$$

yielding the collision efficiency,

$$E_B^{(k)} = \left[\Gamma_{B,0} + \Lambda_{B,0}^{(0)} - \frac{\nu}{2} \log \nu K^{2/5} \right]^{-1} \,, \qquad A_k \ll 1 \,, \tag{4.47}$$

where

$$\Gamma_{B,0} = \lim_{\xi \to 0} \left[\int_\xi^\infty \frac{2}{(2+t)^2 G(t)} dt + \frac{\nu}{2} \log \xi \right] \,, \tag{4.48}$$

and

$$\Lambda_{B,0}^{(0)} = \frac{\nu}{2} \left[\int_1^\infty [f(q) - 1] \frac{dq}{q} + \int_0^1 f(q) \frac{dq}{q} \right] \doteq 0.1626 \, \nu \,. \tag{4.49}$$

Here, $\Gamma_{B,0}$ depends only on size ratio, and $\nu^{-1}\Lambda_{B,0}^{(0)}$ has the indicated constant value. The numerical value of this integral was previously computed to determine the contact time between permeable particles under the action of a constant force [55, Eq.(4.24)].

The effect of particle permeability vanishes in the complementary limit of strong van der Waals attraction, $\bar{A}_k \gg 1$, and the classical result $E_B^{(0)}$ for impermeable spheres is recovered,

$$E_B^{(0)} = \Gamma_B^{-1} \,, \tag{4.50}$$

with Γ_B given by Eq.(4.42).

4.3.2 Collision efficiency for sedimentation

The collision efficiency for permeable particles undergoing sedimentation is given by Eq. (4.27). The collision efficiency integral I_g is evaluated on the contact surface by the procedure described in Appendix C.1.1. For integral (4.27b), the required functions are

$$Q(s) = L(s) \,, \qquad P(s) = (L(s) - M(s))\, s^{-1} \,, \tag{4.51}$$

and from Eqs.(4.31b) and (4.33a), the lubrication forms are

$$Q_\xi = R_g \frac{\xi}{f(q)}\,, \qquad P_\xi = -\frac{1}{2} M_\xi(\xi, q)\,. \tag{4.52}$$

The corresponding functions, L_0 and M_0, for impermeable spheres are also required; their lubrication forms are given by Eqs.(4.35b) and (4.36a). Here, the required indefinite integral (C.1.11) is

$$F_g(x) = -\frac{1}{R_g} \int^x M_{\xi,0}(t) \frac{dt}{2t} = \log f_g(x)\,, \tag{4.53}$$

and $f_g(x)$ is given by Eq. (C.1.30) in Appendix C.1.4. Inserting this result with Eqs. (4.51)-(4.52) into (C.1.12) yields the collision efficiency integral evaluated on the contact surface,

$$I_g^{(k)}(s_c) = \Gamma_g + \Lambda_g^{(0)} - \log f_g(\nu K^{2/5})\,, \tag{4.54}$$

where

$$\Gamma_g = \lim_{\xi \to 0} \left[\int_\xi^\infty \frac{L_0(t) - M_0(t)}{(2+t) L_0(t)} dt + \log f_g(\xi) \right]\,, \tag{4.55}$$

$$\Lambda_g^{(0)} = -\frac{1}{2R_g} \left[\int_1^\infty \left[M_\xi(\xi, q) f(q) - M_{\xi,0}(\xi) \right] \frac{dq}{q} + \int_0^1 M_\xi(\xi, q) f(q) \frac{dq}{q} \right]\,. \tag{4.56}$$

Inserting this result into Eq. (4.27) yields the collision efficiency,

$$E_g^{(k)} = \left[e^{-\left(\Gamma_g + \Lambda_g^{(0)}\right)} f_g\left(\nu K^{2/5}\right) \right]^{-2}\,. \tag{4.57}$$

4.3.3 Collision efficiency for uniaxial strain

The collision efficiency for permeable particles in uniaxial strain is given by Eq. (4.28). The analysis is closely analogous to that given above for gravity-induced collisions.

The collision efficiency integral (4.28b) is evaluated on the contact surface by the procedure described in Appendix C.1.1. In this case, the required functions are

$$Q(s) = 1 - A(s)\,, \qquad P(s) = (A(s) - B(s))\, s^{-1}\,. \tag{4.58}$$

From Eqs.(4.31c) and and (4.33b), the lubrication forms are

$$Q_\xi = R_{st}\frac{\xi}{f(q)}\,, \qquad P_\xi = \frac{1}{2}B'_\xi(\xi, q)\,, \tag{4.59}$$

where we define,

$$B' = 1 - B\,. \tag{4.60}$$

The corresponding functions, $1 - A_0$ and B_0, for impermeable spheres are also required, and their lubrication forms are given by Eqs.(4.35c) and (4.36b). The required indefinite integral (C.1.11) is

$$F_{st}(x) = \frac{1}{R_{st}}\int^x B'_{\xi,0}(t)\frac{dt}{2t} = \log f_{st}(x)\,, \tag{4.61}$$

and $f_{st}(x)$ is given by Eq. (C.1.31) and $B'_{\epsilon,0}$ is defined by Eq. (4.60). Inserting this result with Eqs. (4.58)-(4.59) into (C.1.12) yields the collision efficiency integral evaluated on the contact surface,

$$I^{(k)}_{st}(s_c) = \Gamma_{st} + \Lambda^{(0)}_{st} - \log f_{st}(\nu K^{2/5})\,, \tag{4.62}$$

where

$$\Gamma_{st} = \lim_{\xi\to 0}\left[\int_\xi^\infty \frac{A_0(t) - B_0(t)}{(2+t)\,[1 - A_0(t)]}dt + \log f_{st}(\xi)\right]\,, \tag{4.63}$$

and

$$\Lambda^{(0)}_{st} = \frac{1}{2R_{st}}\left[\int_1^\infty \left[B'_\xi(\xi, q)f(q) - B'_{\xi,0}(\xi)\right]\frac{dq}{q} + \int_0^1 B'_\xi(\xi, q)f(q)\frac{dq}{q}\right]\,. \tag{4.64}$$

Inserting this result into Eq. (4.28) yields the collision efficiency,

$$E_{st}^{(k)} = \left[e^{-\left(\Gamma_{st}+\Lambda_{st}^{(0)}\right)} f_{st}\left(\nu K^{2/5}\right) \right]^3 . \tag{4.65}$$

4.3.4 Collision efficiency for shear flow

Contact values for two collision efficiency integrals are needed for the collision efficiency of particles in shear flow, according to Eq. (4.29). This includes $I_{st}(s_c)$, as analyzed above, and $I_{sh}(s_c)$, analyzed below by the procedure described in Appendix C.1.1. The required functions for $I_{sh}(s_c)$ are

$$Q(s) = 1 - A(s)\,, \qquad P(s) = \frac{1}{4} e^{-2I_{st}(s)} B(s) s\,. \tag{4.66}$$

Here, evaluation of the collision efficiency integral I_{st} is required away from the contact surface which is facilitated by the procedure described in Appendix C.1.3. The lubrication forms of Eq. (4.66) are obtained using Eqs. (C.1.22)-(C.1.23) and Eqs. (4.31c) and (4.33b),

$$Q_\xi = R_{st} \frac{\xi}{f(q)}\,, \qquad P_\xi = \frac{1}{2}\left(e^{-(\Gamma_{st}+\Lambda_{st}(q))} f_{st}(\nu K^{2/5})\right)^2 B_\xi(\xi, q)\,, \qquad \xi = O(K^{2/5})\,, \tag{4.67}$$

and

$$Q_{\xi,0} = R_{st}\,\xi\,, \qquad P_{\xi,0} = \frac{1}{2}\left(e^{-\Gamma_{st}} f_{st}(\xi)\right)^2 B_{\xi,0}(\xi)\,, \qquad K^{2/5} \ll \xi \ll 1\,, \tag{4.68}$$

where Γ_{st} is given by Eq. (4.63) and $f_{st}(\xi)$ is given by Eq. (C.1.31). The function $\Lambda_{st}(q)$ is generically defined by Eq. (C.1.24) and is, in this case, given by

$$\Lambda_{st}(q) = \frac{1}{2R_{st}} \left[\int_1^\infty \left[B'_\xi(\xi, q') f(q') - B'_{\xi,0}(\xi) \right] \frac{dq'}{q'} + \int_q^1 B'_\xi(\xi, q') f(q') \frac{dq'}{q'} \right]\,, \tag{4.69}$$

where B' is defined by Eq. (4.60). The additional indefinite integral (C.1.11), needed for evaluating I_{sh} on the contact surface is

$$F_{sh}(\xi) = \frac{e^{-2\Gamma_{st}}}{2R_{st}} \int_{\xi_0}^{\xi} f_{st}^2(t) B_{\xi,0}(t) \frac{dt}{t} \,, \tag{4.70}$$

where ξ_0 is an arbitrary constant.

Inserting the above elements into (C.1.12) yields the collision efficiency integral evaluated on the contact surface,

$$I_{sh}^{(k)}(s_c) = \Gamma_{sh} + \Lambda_{sh}^{(0)} - F_{sh}\left(\nu K^{2/5}\right) \,, \tag{4.71}$$

where

$$\Gamma_{sh} = \lim_{\xi \to 0} \left[\int_{\xi}^{\infty} \frac{e^{-2I_{st,0}(t)} B_0(t)}{4\left[1 - A_0(t)\right]} (2+t) dt + F_{sh}(\xi) \right] \,, \tag{4.72}$$

and

$$\Lambda_{sh}^{(0)} = \frac{e^{-2\Gamma_{st}}}{2R_{st}} \left[\int_1^{\infty} \left[e^{-2\Lambda_{st}(q)} f_{st}^2\left(\nu K^{2/5}\right) B_{\xi}(\xi, q) f(q) - f_{st}^2\left(\xi\right) B_{\xi,0}(\xi) \right] \frac{dq}{q} \right.$$

$$\left. + \int_0^1 e^{-2\Lambda_{st}(q)} f_{st}^2\left(\nu K^{2/5}\right) B_{\xi}(\xi, q) f(q) \frac{dq}{q} \right] \,. \tag{4.73}$$

Note that the value of ξ_0 used in Eq. (4.70) affects the value of Γ_{sh} but not the value of $I_{sh}^{(k)}(s_c)$.

Inserting this result together with Eqs. (4.62) into Eq. (4.29) yields

$$E_{sh}^{(k)} = \left[\left(e^{-\left(\Gamma_{st} + \Lambda_{st}^{(0)}\right)} f_{st}\left(\nu K^{2/5}\right) \right)^2 - \left(\Gamma_{sh} + \Lambda_{sh}^{(0)} - F_{sh}\left(\nu K^{2/5}\right) \right) \right]^{3/2} \,, \tag{4.74}$$

where the quantity inside the square brackets is assumed to be positive, otherwise $E_{sh} = 0$. In shear flow, there exists a positive, size-ratio-dependent critical perme-

ability, K_*, below which $E_{sh} = 0$. The critical permeability is a root of the equation

$$\left(e^{-\left(\Gamma_{st}+\Lambda^{(0)}_{st*}\right)} f_{st}\left(\nu K_*^{2/5}\right)\right)^2 - \left(\Gamma_{sh} + \Lambda^{(0)}_{sh*} - F_{sh}\left(\nu K_*^{2/5}\right)\right) = 0\,, \tag{4.75}$$

where $\Lambda^{(0)}_{st*}$ and $\Lambda^{(0)}_{sh*}$ denote evaluation at $K = K_*$. The existence of a critical permeability is analogous to the critical roughness below which particle contact does not occur in shear [88].

4.4 Collision efficiency formulas for rough particles

Aggregation of particles with small-amplitude surface roughness $\delta \ll 1$ is considered in this section because of the qualitative similarity to the aggregation of permeable particles. Rough particles also have axisymmetric mobilities with non-zero contact values and can thus undergo aggregation in the absence of non-hydrodynamic interparticle forces. The $O(\delta)$ boundary layer that forms in the limit of small-amplitude roughness is analogous to the $O(K^{2/5})$ boundary layer formed with permeable particles in the weak-permeability limit (4.1).

The axisymmetric mobilities of particles with surface roughness have non-zero $O(\delta)$ contact values because the contact surface is, by definition, at a non-zero surface-to-surface separation, $\epsilon = \delta$; the contact values are obtained by inserting $\epsilon = \delta$ into the near-contact mobilities for impermeable particles Eqs. (4.35)-(4.36). For separations $\epsilon > \delta$, the mobilities of rough particles are identical to those for smooth, impermeable particles [49, 64, 102].

4.4.1 Collision efficiencies for rough particles

As shown in Appendix C.1.2, values of collision efficiency integrals at the contact surface, $s = 2 + \nu\delta$, for particles with small-amplitude surface roughness, δ, are directly obtained from the contact values of collision efficiency integrals for permeable particles by making the substitution:

$$\Lambda^{(0)} \to F(\nu K^{2/5}) - F(\nu\delta)\,. \tag{4.76}$$

This result is supported by Eq. (C.1.25). By this procedure, the collision efficiencies for particles with small-amplitude surface roughness are derived below. A direct derivation of the formulas is presented in Appendix C.1.2, and parameters needed for evaluating the formulas are provided in Appendix C.2.

Brownian motion

By the procedure described above, using substitution (4.76), the collision efficiency for rough particles in Brownian motion is derived from Eq. (4.40), and is given by

$$E_B^{(\delta)} = \left[\Gamma_B - \frac{\nu}{2} E_1(A_\delta)\right]^{-1}\,, \tag{4.77}$$

where Γ_B is given by Eq. (4.42), $E_1(x)$ is the exponential integral, and A_δ is the modified Hamaker parameter for rough particles,

$$A_\delta = \frac{\bar{A}_H}{6\delta}\,. \tag{4.78}$$

For $A_\delta \ll 1$, Eq. (4.77) reduces to

$$E_B^{(\delta)} = \left[\Gamma_{B,0} - \frac{\nu}{2}\log\nu\delta\right]^{-1}\,, \qquad A_\delta \ll 1\,, \tag{4.79}$$

where $\Gamma_{B,0}$ is given by Eq. (4.48). The classical result (4.50) is recovered for $A_\delta \gg 1$; surface roughness has negligible effect under these conditions.

Gravity sedimentation

The collision efficiency for rough particles undergoing sedimentation, derived from Eq. (4.57) by substitution (4.76), is

$$E_g^{(\delta)} = \left(e^{-\Gamma_g} f_g(\nu\delta)\right)^{-2} , \tag{4.80}$$

where f_g is defined by Eq. (C.1.30) and Γ_g is given by Eq. (4.55).

Uniaxial strain

The collision efficiency for rough particles in uniaxial strain, derived from Eq. (4.62) by substitution (4.76), is

$$E_{st}^{(\delta)} = \left(e^{-\Gamma_{st}} f_{st}(\nu\delta)\right)^{3} , \tag{4.81}$$

where f_{st} is defined by Eq. (C.1.31) and Γ_{st} is given by Eq. (4.63).

Shear flow

By the same procedure, substituting Eq. (4.76) into Eq. (4.75), the collision efficiency of rough particles in shear flow is given by

$$E_{sh}^{(\delta)} = \left[\left(e^{-\Gamma_{st}} f_{st}(\nu\delta)\right)^2 - (\Gamma_{sh} - F_{sh}(\nu\delta))\right]^{3/2} , \tag{4.82}$$

where f_{st} is given by Eq. (C.1.31), Γ_{st} by Eq. (4.63), Γ_{sh} by (4.72), and F_{sh} by (4.70).

The size-ratio-dependent critical roughness, δ_*, below which $E_{sh}^{(\delta)} = 0$ [88], is a root of the equation obtained by making the same substitution into Eq.(4.75), i.e.,

$$\left(e^{-\Gamma_{st}} f_{st}(\nu\delta_*)\right)^2 - (\Gamma_{sh} - F_{sh}(\nu\delta_*)) = 0 . \tag{4.83}$$

4.4.2 Equivalent roughness

The qualitative similarity between weakly-permeable particles and particles with small-amplitude surface roughness suggests the introduction of an equivalent roughness δ_{eq} defined by setting the corresponding collision efficiencies equal, $E^{(\delta_{eq})} = E^{(k)}$. Equating the collision efficiency for permeable and rough particles, by equating contact values for the collision efficiency integrals (C.1.12) and (C.1.20) yields

$$F(\nu\delta_{eq}) - F(\nu K^{2/5}) + \Lambda^{(0)} = 0\,. \tag{4.84}$$

This result suggests $\delta_{eq} \approx c_k K^{2/5}$, reflecting the respective boundary layer thicknesses for the two problems, where the coefficient c_k would be expected to depend on the aggregation mechanism and size ratio of the particles. Inserting this scaling and Eqs. (4.86), (C.1.11), and (C.1.14) into Eq. (4.84) yields an equation for the roughness coefficient, c_k,

$$\int_1^{c_k} P_{\xi,0}(\xi)\frac{dq}{q} + \int_1^{\infty} \left[P_\xi(\xi,q)f(q) - P_{\xi,0}(\xi)\right]\frac{dq}{q} + \int_0^1 P_\xi(\xi,q)f(q)\frac{dq}{q} = 0\,. \tag{4.85}$$

This relationship is not generally invertible except for constant P_ξ, and, under these conditions, c_k will be independent of size ratio. These conditions are met for particle aggregation under Brownian motion in the absence of van der Waals attraction, according to Eq. (4.45b). Inserting Eqs. (4.45b) and (4.49) into relation (4.85) yields

$$\delta_{eq} = c_k K^{2/5}\,, \qquad c_k = e^{-2\nu^{-1}\Lambda^{(0)}_{B,0}} \doteq 0.7224\,. \tag{4.86}$$

The collision efficiency of particles with permeability K under Brownian motion without van der Waals attraction is thus rigorously related to the collision efficiency of particles with surface roughness δ_{eq}; the result is independent of size ratio. Defining equivalent roughness by equating collision rates in Brownian motion is mathematically

equivalent to equating the contact time between permeable and rough particles under the action of a constant force directed along their line-of-centers starting from an arbitrary separation outside of the lubrication region (cf. [55, Eqs.(4.24) and (4.26)]).

Equation (4.86) holds for constant P_ξ in Eq. (4.85). Non-constant P_ξ arises because of the oblique near-contact trajectories that determine collision efficiencies in sedimentation, uniaxial strain, and in shear flow. The transverse mobilities M and B are insensitive to permeability thus $P_\xi \approx P_{\xi,0}$ [116] but the logarithmic behavior of $P_{\xi,0}$ at $\xi = 0$, resulting from the lubrication forms of the transverse mobilities (4.36), suggests that, while the scaling of Eq. (4.86) is expected to hold, the roughness coefficient, c_k, may be sensitive to the aggregation mechanism, size ratio, and the Hamaker constant (Brownian motion). However, the results presented below contradict this conclusion and support the robustness of Eq. (4.86) for all four aggregation mechanisms and parameter ranges considered herein.

4.5 Numerical Results and Discussion

In this section, numerical results are presented for collision efficiencies of permeable particles undergoing (i) Brownian motion, (ii) gravity sedimentation, (iii) uniaxial straining flow, and (iv) shear flow. In the latter case, results are also presented for the critical permeability below which $E_{sh} = 0$. The corresponding results for rough particles are also presented using the relationship (4.86). The procedure for evaluating the collision efficiencies is described in Appendix C.2.

Figures 4.1-4.5 reveal very close quantitative agreement between the results for permeable and rough particles using an equivalent roughness defined by (4.86) for all four aggregation mechanisms over a wide range of parameter values; in most cases, the curves for permeable particles and particles with equivalent roughness are virtually indistinguishable.

The dotted lines in figure 4.3 depict results for permeable particles obtained using the axisymmetric lubrication formula (4.31c) for permeable particles with the transverse lubrication formula (4.36b) for impermeable particles (i.e., in place of Eq. (4.33b)). Particle permeability has no effect on the transverse pair mobility of equal size particles, a modest effect on unequal size particles, and it qualitatively affects the near-contact motion for extreme size ratios [116]. A comparison of the dotted and solid lines in figure 4.3, however, indicates that effect of permeability on the transverse mobility is barely perceptible even for $\kappa = .125$. This finding demonstrates the insensitivity of collision efficiencies to the transverse mobility and provides a plausible explanation for the robustness of the proposed equivalent roughness (4.86) for permeable particles.

Bäbler *et. al.* (2006) [44] calculated collision efficiencies for permeable particles in shear flow in complementary high-permeability regime, $K = O(1)$. A reliable quantitative comparison to their results is not possible due to the disparity of the regimes considered. However, results for the largest permeabilities presented in figure 4.4 appear to be in approximate agreement with the predictions of Bäbler *et. al.* (2006) for permeabilities in the smallest range they considered.

Permeability and roughness are analogous generic mechanisms that allow particle aggregation without the need for interparticle forces. Simplified asymptotic formulas for binary collision rates were derived for weak permeability and small-amplitude roughness. A quantitative relation between permeable and rough particles is established through an equivalent roughness, allowing use of the simpler explicit formulas for rough particles as approximations for the aggregation rate of permeable particles.

Note

The authors are grateful to Dr. A. Z. Zinchenko [63] for the use of his bispherical coordinate code for computing pair mobilities of impermeable spheres, and to Dr. D. J. Jeffrey [67] for the use of his program available online for resistance functions used herein to obtain the matching constants for the resistance functions of impermeable spheres.

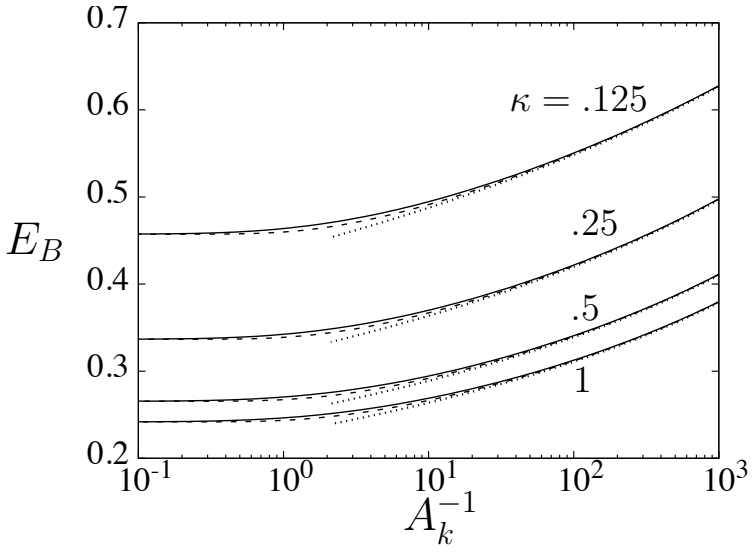

Figure 4.1: Collision efficiencies for particles in Brownian motion, permeable particles (4.40) (solid lines), rough particles (4.77) with $A_\delta^{-1} = c_k A_k^{-1}$ with c_k given by Eq. (4.86) (dashed lines), size ratios indicated, and $\bar{A}_H = 10^{-4}$; weak van der Waals formula (4.47) (dotted lines).

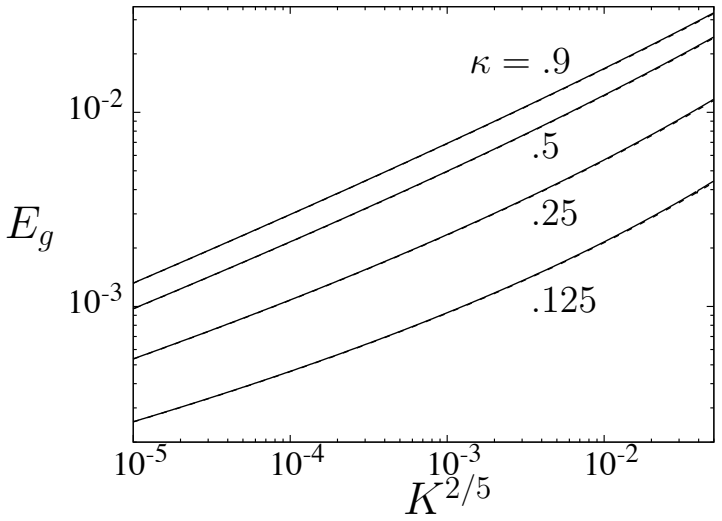

Figure 4.2: Collision efficiencies for particles undergoing sedimentation, permeable particles (4.57) (solid lines), rough particles (4.80) with δ_{eq} given by Eq. (4.86) (dashed lines); size ratios indicated.

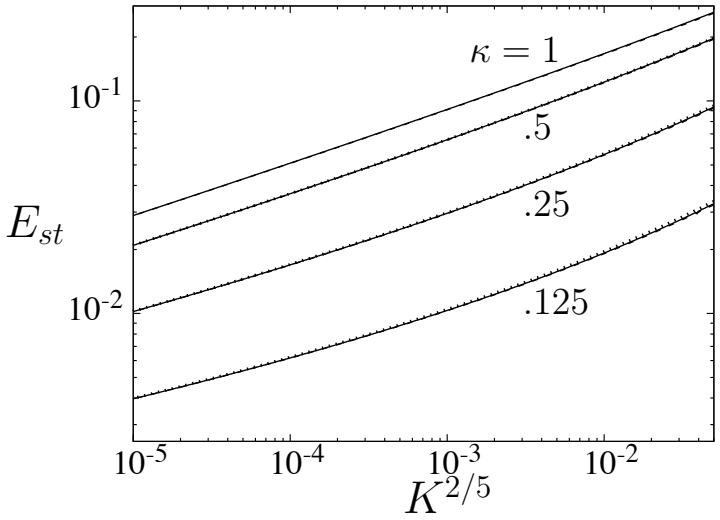

Figure 4.3: Collision efficiencies for particles in uniaxial straining flow, permeable particles (4.65) (solid lines), rough particles (4.81) with δ_{eq} given by Eq. (4.86) (dashed lines), permeable particles using impermeable transverse mobility function $B_{\xi,0}$ (dotted lines); size ratios indicated.

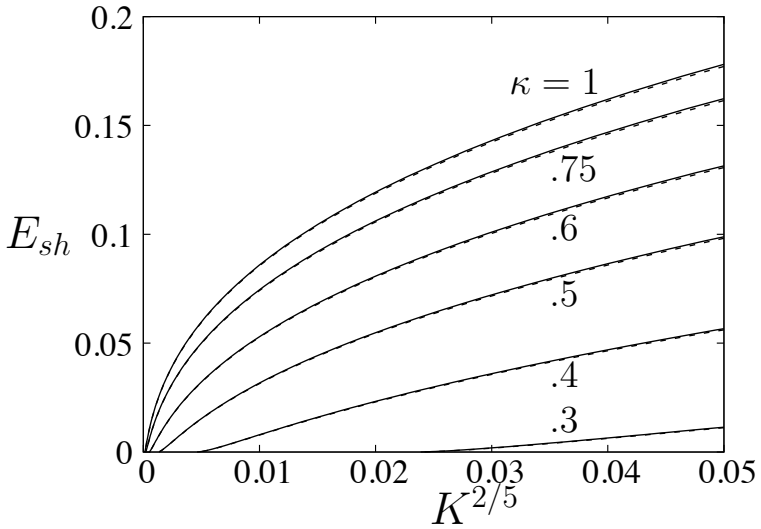

Figure 4.4: Collision efficiencies for particles in shear flow, permeable (4.74) (solid lines), and rough particles (4.82) with δ_{eq} given by Eq. (4.86) (dashed lines); size ratios indicated.

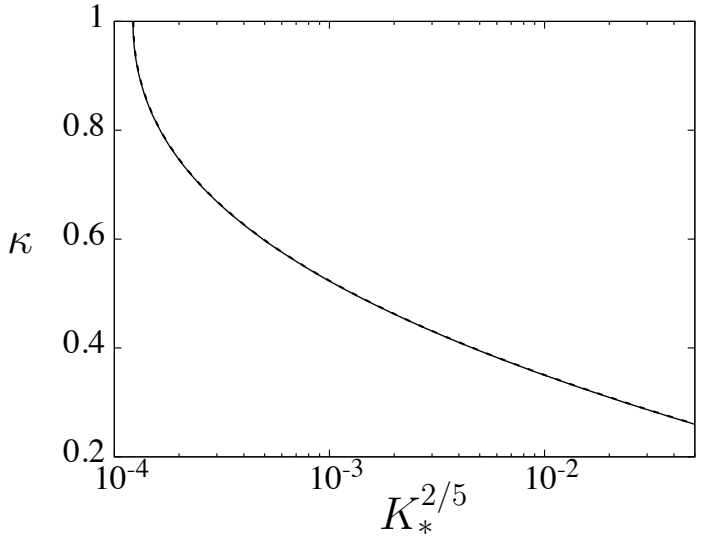

Figure 4.5: Size ratio versus critical permeability (4.75) (solid lines) and critical roughness (4.83) with δ_{eq} given by Eq. (4.86) (dashed lines).

Chapter 5

A pairwise hydrodynamic theory for flow-induced particle transport in shear and pressure-driven flows

5.1 Introduction

Particles in a fluid subjected to a bulk deformation interact with each other hydrodynamically, modifying the rheology of suspensions, and can lead to flow-induced microstructuring [119–123]. Flow-induced microstructure in flowing suspensions is a key to understanding a diverse range of natural phenomena and is fundamental to the engineering design of these systems. Flow-induced microstructure is important in materials processing, such as the production of particle-filled polymers [124–126], and ceramic tape casting [127]. Rheology and microstructure affect the sensation of food and digestion [2, 3]. Flow-induced demixing in polydisperse suspensions is a useful separation technique [4, 5].

The effects of suspension microstructure are especially pronounced in tightly-confined flows as arise in microfluidic devices [128–131] and hydrofracturing [132,133].

Blood flow in the microcirculation depends critically on the coupled rheology and flow-induced microstructure [1]. The Fahraeus-Lindqvist effect refers to the concomitant reduction in hematocrit and viscosity in capillaries and small vessels (i.e., arterioles, venules). In their classical paper, Fahraeus and Lindqvist [134] explain these phenomena in terms of the migration of red blood cells (erythrocytes) to the region of faster-moving fluid at the center of the capillary where velocity gradients are smaller. This mechanism is important for reducing the workload on the heart and helps to understand the detrimental effects of certain diseased states (e.g., malaria, sickle-cell anemia) that disrupt this mechanism by altering the mechanical properties of red blood cells [135–137]. This phenomenon continues to be an active area of study [138–140].

Investigations of flow-induced structuring have focused on suspensions of spherical particles suspended in Newtownian liquids. Low-Reynolds-number conditions usually apply, based on the small size of the suspended particles in typical applications. Accordingly, fluid motion is governed by the Stokes equations [141]. Early studies include experimental measurements [142, 143] and computer simulations [144, 145] of self-diffusion of marked tracer particles in sheared suspensions. Eckstein et. al. [142] proposed a self-diffusivity, $D_s \sim \dot{\gamma} a^2$, resulting from $O(a)$ random particle displacements with zero mean due to uncorrelated hydrodynamic interactions between particles occurring at a rate of $\dot{\gamma}$, where a is the particle radius, $\dot{\gamma}$ is the magnitude of the shear-rate, and the proportionality depends on the volume fraction. Leighton and Acrivos [146] proposed the existence of a cross-flow particle flux down the particle concentration gradient with a similarly scaled diffusivity, $D \sim D_s$, and a particle drift velocity, V, from high to low shear stress [147]. This theoretical framework was used to explain the anomolous time-varying viscosity previously observed by Gadala-Maria and Acrivos [147, 148] and provides the basis for the diffusive flux model of suspensions where the microstructure is predicted by a phenomenological particle transport

equation and is coupled to the suspension rheology [149]. The diffusive flux model has been subsequently used to describe the flow-induced microstructure and rheology of suspensions and emulsions [150–152].

An alternate suspension balance model was developed where particle fluxes result from particle stresses [153, 154]. The suspension balance model has also been widely used to explore the flow-induced microstructure and rheology of suspensions [155–159]. The suspension balance and diffusive flux models are similar; moreover, the diffusive flux model can be derived from the suspension balance model [153, 160].

Both models have difficulty describing flows at points where the local shear-rate vanishes, e.g., at the center of a Poiseuille flow. At these points, the predicted particle concentration profile has an unphysical cusp but the issue can be remedied through the use of an ad hoc non-local shear-rate or the imposition of a maximum particle packing fraction. Away from these singular points, the predicted particle concentration profiles are in general agreement with experimental measurements [156, 161–163], including predictions of size segregation in bidisperse suspensions with enrichment of larger particles in regions of low shear-rate [164–166] seen in experiments [167–169]. However, the prediction that particle enrichment can be manipulated, even reversed, to yield the enrichment of smaller particles in low-shear-rate regions has not been observed.

Kinetic theory models have been used to predict particle segregation in suspensions of polydisperse systems with complex, deformable particles [170–178]. Some of these studies focused on margination, the size segregation that occurs in the vicinity of a no-slip boundary; others explored size segregation that occurs in small channels, several particle diameters wide (e.g., arterioles, venules). The results further a fundamental understanding of the Fahraeus-Lindqvist effect and related phenomena such as plasma skimming [179, 180], showing that smaller, stiffer particles (e.g., platelets, neutrophils) accumulate near bounding walls of a channel with larger and more de-

formable particles (e.g., erythrocytes) migrating away. These models are inherently pairwise descriptions and thus, in principle, restricted to semi-dilute systems although they may represent a reasonable coarse-graining for suspensions with modest particle volume fraction [181–184]. This is more likely to be true for soft particles because particle deformation tends to suppress highly-correlated phenomena, such as jamming. These descriptions involve computationally intensive boundary integral simulations of pair trajectories of deformable particles to determine the resulting displacements that yield the collision kernel of the kinetic theory model. The resulting Boltzmann equation can be directly integrated to yield the particle distributions, or the collision kernel can be expanded for smoothly varying spatial distributions of particles, extracting diffusive particle fluxes and drift velocities resulting from pair interactions. This yields a phenomenological particle transport equation similar to the diffusive flux model.

Pairwise hydrodynamic interactions of force- and torque-free, spherical particles in shear flow under creeping flow conditions are well-understood and analytically tractable [87, 185–188]. By the linearity of the Stokes equations and by symmetry, pair interactions between spherical particles on open trajectories in shear flow are reversible, yielding zero net cross-flow displacements of the particles; however, there are diverse phenomena that can break the symmetry of pair trajectories in shear flow, leading to non-zero net displacements. It is generally accepted that particle displacements resulting from irreversible pair interactions are the dominant mechanism for particle transport [146, 149].

Mechanisms that break the symmetry of pair interactions include the perturbative effects that slightly affect hydrodynamic pair interactions and short-range phenomena that qualitatively affect the motion of particles when they are in near-contact with surface-to-surface separations $h_0 \ll a$ but have a negligible effect at larger separations. Short-range phenomena involve symmetry-breaking "contact" interactions

between particles on narrowly offset streamlines of the flow. The classical lubrication singularity between smooth spherical particles hinders the near-contact approach of particles in the compressive quadrant of the shear flow, preventing contact, and acts symmetrically slowing the separation of the particles in the extensional quadrant of the flow. Contact interactions break the symmetry of pair interactions in shear flow because they involve a compressive force that prevents particle overlap in the compressive quadrant of the flow without a compensating tensile force in the extensional quadrant.

The prototypical example of a short-range mechanism for contact interactions is small-amplitude surface roughness, $d \ll a$, that prevents surface-to-surface particle separations less than d. [49, 102, 103, 189, 190]. Other examples of particles with short-range contact interactions include particles with weak permeability [55,116,191], particles stabilized by screened electrostatic interactions [94,192], and emulsion drops under high-surface-tension conditions [151,193]. Particle-scale deformation associated with stronger flows is an example of a perturbative mechanism, affecting hydrodynamic interactions at $O(a)$ separations, and breaking the symmetry of more distant, non-contacting pair trajectories [194–197]. It is worth noting that qualitatively similar results are predicted under high-surface-tension conditions where displacements result from short-range contact interactions [193].

In this chapter, we present a simplified theory for flow-induced structuring in particle suspensions based on pair interactions between particles. Starting from a Boltzmann-type master equation, particle fluxes are derived for the cross-flow hydrodynamic particle transport in flows such as shear and planar Poiseuille flow. A general analysis is presented for the boundary layer that forms in regions where the shear rate vanishes and for the stationary particle distributions that form away from these regions. Cross-stream displacements for particles that undergo symmetry-breaking, contact interactions are formulated in terms of quadratures of mobility functions for

spherical particles. Using this result, transport coefficients are explicitly calculated for rough particles and emulsion drops and results are presented for particle distributions and calculated for monodisperse and bidisperse suspensions.

The general formulation of the problem, including the Boltzmann equation is presented in § 5.2, transport coefficients are derived in §5.3 including an analysis of the region where shear rates vanish. General results for stationary particle distributions are derived in §5.4 that are independent of the character of the pair interactions between particles. Trajectories of particles that undergo contact interactions are analytically integrated in §5.5 to yield particle displacements formulated as quadratures of standard mobility functions. The results from §5.4 and §5.5 are combined in §5.6 to obtain spatial distributions of rough particles and emulsion drops in mono- and bidisperse mixtures. Concluding remarks are made in §5.7.

5.2 Boltzmann formulation

We consider particle transport in a polydisperse suspension of non-Brownian neutrally-buoyant particles in 2d unidirectional flows,

$$\mathbf{v} = v(X_2)\mathbf{e_1}\,, \tag{5.1}$$

where (X_1, X_2, X_3) describes a Cartesian coordinate system and $\mathbf{e_k}$ $(k = 1, 2, 3)$ are the corresponding unit vectors. Velocity fields (5.1) include simple shear and planar Poiseuille flow.

The particle distribution evolves in the plane perpendicular to the fluid velocity according to a Boltzmann-type master equation [171, 174]

$$\frac{\partial n_i}{\partial t} = -\boldsymbol{\nabla}\cdot\mathbf{F}_i\,, \tag{5.2}$$

where $n_i(X_2, X_3)$ is the number density of type-i particles ($i = 1, 2, \cdots, m$), and $F_{ik}(X_2, X_3)$ ($k = 2, 3$) is the flux of type-i particles in the k-direction resulting from pairwise "collisions" with other particles,

$$F_{ik}(X_2, X_3) = \sum_{j=1}^{m} F_{ijk}\,. \tag{5.3}$$

Here, F_{ijk} is the contribution to the flux F_{ik} from collisions with type-j particles ($j = 1, 2, ..., m$) given by the Boltzmann collision integral,

$$F_{ijk} = \int_{-\infty}^{\infty} dx_3^{-\infty} \int_{-\infty}^{\infty} dx_2^{-\infty} \int_{-\Delta X_k^{ij}}^{0} n_i(X_k^{i,-\infty}) n_j(X_k^{j,-\infty}) \left|v^{ij}\right| dX_k^{i,-\infty}\,, \tag{5.4}$$

where $X_k^{i,-\infty}$ is the distance of particle i from the plane X_k where the flux is evaluated, and ΔX_k^{ij} is the displacement of particle i in the k-direction due to its binary encounter with particle j. Prior to a pair interaction, particles are widely separated in the X_1-direction (i.e., flow direction) with uncorrelated initial positions $(X_2^{i,-\infty}, X_3^{i,-\infty})$ and $(X_2^{j,-\infty}, X_3^{j,-\infty})$ in the cross-flow plane. The relative initial position in the cross-flow plane, i.e., the trajectory offset, is defined, $x_k^{-\infty} = X_k^{j,-\infty} - X_k^{i,-\infty}$, ($k = 2, 3$). Formula (5.4) is obtained using the odd symmetry of particle displacements with respect to trajectory offset,

$$\Delta X_k^{ij}\left(-x_k^{-\infty}\right) = -\Delta X_k^{ij}\left(x_k^{-\infty}\right)\,. \tag{5.5}$$

Particle displacements are, moreover, symmetric with respect to complementary coordinates, i.e.,

$$\Delta X_2^{ij}(-x_3^{-\infty}) = \Delta X_2^{ij}(x_3^{-\infty})\,, \qquad \Delta X_3^{ij}(-x_2^{-\infty}) = \Delta X_3^{ij}(x_2^{-\infty})\,. \tag{5.6}$$

The widely-separated particles approach with velocity magnitude,

$$|v^{ij}| = \left|v(X_2^{j,-\infty}, X_3^{j,-\infty}) - v(X_2^{i,-\infty}, X_3^{i,-\infty})\right| , \tag{5.7}$$

where $v(X_2, X_3)$ is the prescribed velocity (5.1).

Cross-flow convection, such as particle migration away from solid boundaries, is outside the scope of our study, and is omitted from Eq. (5.2). For suspensions contained by boundaries that are impermeable to the particles, stationary particle distributions are governed by

$$\mathbf{F}_i = 0 . \tag{5.8}$$

5.3 Particle transport

5.3.1 Local transport coefficients

Here, we analyze particle transport in suspensions undergoing flows with velocity (5.1) and derive diffusive and drift fluxes, i.e., fluxes proportional to the local concentration gradients of particle species and a flux associated with a drift velocity of particles from high to low shear rates. Local transport coefficients for these fluxes are obtained. The diffusive fluxes have been derived previously [198] and a drift velocity has been extracted from a Boltzmann collision integral [177]. A brief derivation is provided below for completeness and uniformity.

The diffusive and drift fluxes are obtained by evaluating the collision flux (5.4) for perturbative variations in number densities and relative velocities. The number densities and shear-rates are expanded up to linear variations,

$$n_i = n_{i0} + \sum_{k=2}^{3} \frac{\partial n_i}{\partial X_k} X_k + O(X_k^2) , \tag{5.9}$$

$$\dot{\gamma} = \dot{\gamma}_0 + \frac{d\dot{\gamma}}{dX_2} X_2 + O(X_2^2)\,, \tag{5.10}$$

where $\dot{\gamma}_0$ and n_{i0}, respectively, are the local shear-rate-magnitude and number densities of the particles at $X_k = 0$ $(k = 2, 3)$; the quantities $d\dot{\gamma}/dX_2$ and $\partial n_i/\partial X_k$ are the corresponding local values of the derivatives. In general, the relative velocity (5.7) becomes

$$|v^{ij}| = |x_2^{-\infty}| \left| \dot{\gamma}_0 + \frac{d\dot{\gamma}}{dX_2} \left[X_2^{i,-\infty} + \frac{1}{2} x_2^{-\infty} \right] \right| . \tag{5.11}$$

The development presented here assumes a non-vanishing shear rate,

$$\dot{\gamma}_0 > \left| \frac{d\dot{\gamma}}{dX_2} \right| \left| X_2^{i,-\infty} + \frac{1}{2} x_2^{-\infty} \right| , \tag{5.12}$$

so that the relative velocity (5.11) reduces to

$$|v^{ij}| = |x_2^{-\infty}| \left(\dot{\gamma}_0 + \frac{d\dot{\gamma}}{dX_2} \left[X_2^{i,-\infty} + \frac{1}{2} x_2^{-\infty} \right] \right) . \tag{5.13}$$

The case of vanishing shear rates is analyzed in the next section.

Inserting Eqs.(5.9)-(5.10) into the flux (5.4) and integrating in $X_k^{i,-\infty}$ yields the net flux of type-i particles,

$$F_{ik} = F_{ik}^{(c)} + \delta_{k2} F_{i2}^{(\dot{\gamma})}\,, \tag{5.14}$$

where $F_{ik}^{(c)}$ are the diffusive fluxes

$$F_{ik}^{(c)} = -D_{ik}^{s} \frac{dn_i}{dX_k} - \sum_{j=1}^{m} \left(D_{ijk} \frac{dn_j}{dX_k} \right) , \tag{5.15}$$

and $F_{i2}^{(\dot{\gamma})}$ is the drift flux

$$F_{i2}^{(\dot{\gamma})} = -n_{i0} V_i \frac{d\dot{\gamma}}{dX_2}\,. \tag{5.16}$$

The Kronecker delta δ_{pq} in Eq. (5.14) indicates that there is a drift flux in the X_2-direction only.

The above diffusivities and the drift-velocity-coefficient are defined by

$$D^s_{ik} = \dot{\gamma}_0 \sum_{j=1}^{m} n_{j0}\, I^A_{ijk}\,, \tag{5.17}$$

$$D_{ijk} = \dot{\gamma}_0\, n_{i0} \left(I^A_{ijk} + I^B_{ijk} \right)\,, \tag{5.18}$$

$$V_i = \sum_{j=1}^{m} n_{j0} \left(I^A_{ij2} + \frac{1}{2} I^B_{ij2} \right)\,, \tag{5.19}$$

where I^A_{ijk}, I^B_{ijk} are integrals over the cross-flow plane,

$$I^A_{ijk} = \frac{1}{2} \int_{-\infty}^{\infty} \int_{-\infty}^{\infty} |x_2^{-\infty}| (\Delta X^{ij}_k)^2 dx_2^{-\infty} dx_3^{-\infty}\,, \tag{5.20}$$

$$I^B_{ijk} = -\int_{-\infty}^{\infty} \int_{-\infty}^{\infty} |x_2^{-\infty}| x_k^{-\infty} \Delta X^{ij}_k dx_2^{-\infty} dx_3^{-\infty}\,. \tag{5.21}$$

Both integrals are intrinsically positive given the symmetry of particle displacements (5.5).

The self diffusivity of type-i particles, D^s_{ik}, defined by Eq. (5.17), can be directly obtained as a sum of the rate of mean squared displacements from random encounters with all particle species. Diffusive fluxes occur in the both the velocity gradient and vorticity directions and have contributions from concentration gradients of all species; a non-zero diffusive flux of a species with uniform concentration can be generated by a gradient of another species. This formulation of the diffusive fluxes concurs with that presented by Zarraga & Leighton (2001).

The drift velocities describe the migration of particles from regions of high shear rates. Gradients of the shear-rate-magnitude $\dot{\gamma}$ generate an oppositely-directed flux. By symmetry, gradients of the shear-rate-magnitude do not contribute to the diffusive flux.

The $O(r^{-3})$ far-field velocity gradients of force-free particles perturb the trajectories of deformable particles, where r is distance between the particles normalized

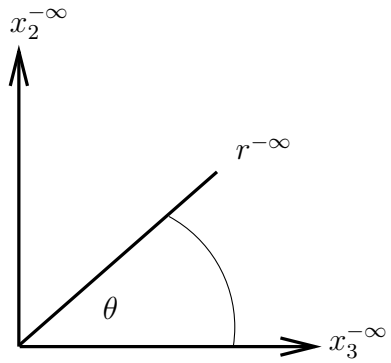

Figure 5.1: Cylindrical coordinate system for cross-flow plane.

by particle size. Integrated along an open trajectory, this perturbation produces pair displacements $\Delta X_k^{ij} = O(r^{-\infty})^{-2}$ for widely offset trajectories, $r^{-\infty} \gg 1$, where $r^{-\infty}$ is the radial relative trajectory coordinate, defined in figure 5.1. Accordingly, integral (5.21) is divergent. The self-diffusivity of deformable particles can be computed from pair interactions because integral (5.20) converges [193], but the evaluation of the diffusive and drift fluxes (5.15) and (5.16) requires a numerical cut-off [173, 175],

$$\Delta X_k^{ij} = 0\,, \qquad r^{-\infty} > r_c^{ij}\,, \tag{5.22}$$

where $r_c^{ij} = r_c^{ji}$. With this cut-off, integrals (5.20)-(5.21) become

$$I_{ijk}^A = \frac{1}{2}\int_0^{2\pi}\int_0^{r_c^{ij}} |r^{-\infty}\sin\theta|(\Delta X_k^{ij})^2\, r^{-\infty} dr^{-\infty} d\theta\,, \tag{5.23}$$

$$I_{ijk}^B = -\int_0^{2\pi}\int_0^{r_c^{ij}} |r^{-\infty}\sin\theta| x_k^{-\infty}\Delta X_k^{ij}\, r^{-\infty} dr^{-\infty} d\theta\,. \tag{5.24}$$

where $(r^{-\infty}, \theta)$ is a cylindrical coordinates system with $x_2^{-\infty} = r^{-\infty}\sin\theta$ and $x_3^{-\infty} = r^{-\infty}\cos\theta$, as shown in figure 5.1.

As discussed in §5.5, the outer boundary (5.22) applies rigorously for spherical particles that undergo contact interactions. Such particles have circular upstream collision cross-sections [94, 189].

5.3.2 Particle transport at points of vanishing shear rate

Here, the analysis of particle transport developed in the previous section is extended to regions where the shear rate vanishes linearly. Accordingly, we consider regions where the velocity is locally quadratic,

$$v = v_0 + \frac{\gamma_2'}{2} X_2^2 \,, \tag{5.25}$$

where γ_2' is the magnitude of the shear-rate gradient and v_0 is an arbitrary local velocity that can be ignored since only velocity differences are significant. The corresponding magnitude of the shear rate and its gradient are given by

$$\dot{\gamma}_0 = \gamma_2' \left| X_2 \right| , \qquad \frac{d\dot{\gamma}}{dX_2} = \text{sign}\left(X_2\right) \gamma_2' \,. \tag{5.26a, b}$$

An example is the velocity field at the center of planar Poiseuille flow in a channel of half-width H, where $\mathbf{v}$ is given by Eq. (5.1) with

$$v = V_0 \left[1 - \left(\frac{X_2}{H} \right)^2 \right] . \tag{5.27}$$

Here, $v_0 = V_0$ is the velocity at centerline, $X_2 = 0$, and the magnitude of the shear rate is given by Eq. (5.26) with $\gamma_2' = 2V_0 H^{-2}$.

Inserting Eq. (5.26) into Eq. (5.11) yields the relative velocity magnitude,

$$|v^{ij}| = \dot{\gamma}_2' \left| x_2^{-\infty} \right| \left| X_2 + X_2^{i,-\infty} + \frac{1}{2} x_2^{-\infty} \right| . \tag{5.28}$$

For $|X_2| > X_c^{ij}$, the result reduces to the form of Eq. (5.13),

$$|v^{ij}| = \dot{\gamma}_2' \left| x_2^{-\infty} \right| \left(|X_2| + \text{sign}(X_2) \left[X_2^{i,-\infty} + \frac{1}{2} x_2^{-\infty} \right] \right) , \qquad |X_2| > X_c^{ij} \,, \tag{5.29}$$

where X_c^{ij} is the half-width of the excluded region

$$X_c^{ij} = \max \left| X_2^{i,-\infty} + \frac{1}{2} x_2^{-\infty} \right| \leq \Delta X_{2,\max}^{ij} + \frac{1}{2} r_c^{ij} \,. \tag{5.30}$$

Here, $\Delta X_{2,\max}^{ij}$ is the maximum displacement magnitude of a type-i particle by a pair interaction with a type-j particle and is thus the upper bound for $|X_2^{i,-\infty}|$; the radius of the collision cross-section, r_c^{ij}, is the upper bound for $|x_2^{-\infty}|$. In general, $\Delta X_{2,\max}^{ij}$, and thus X_c^{ij}, are $O(r_c^{ij})$. For spherical particles that undergo contact interactions, $X_c^{ij} \leq r_c^{ij}$, as discussed in §5.5.

For $|X_2| > X_c^{ij}$, the local analysis presented in §5.3.1 applies with shear-rate magnitude and gradient given by Eq. (5.26). Accordingly, a linearly-varying diffusive flux and constant drift velocity are obtained according to Eqs. (5.15)-(5.19). However, for $|X_2| < X_c^{ij}$, the relative velocity, v_{ij}, changes sign within the maximum range of particle displacements, $\Delta X_{2,\max}^{ij}$, that contribute to the particle flux. Within this region, Eq. (5.28) must be used to describe the magnitude of the relative velocity. The use of Eq. (5.29) is inconsistent and leads to incorrect results. For example, inserting the linearly-varying diffusive flux balanced by the constant drift velocity, obtained by the local analysis, into Eq. (5.14) and then (5.8) yields,

$$X_2 \, n \frac{dn}{dX_2} = -Mn^2 \,, \tag{5.31}$$

where $M > 0$ is a positive constant. A singular distribution, $n \approx |X_2|^{-M}$ is thus obtained, as pointed out by Leighton & Acrivos (1987) [146].

The region $|X_2| < X_c^{ij}$ defines a boundary layer within which the transport coefficients exhibit a more complex dependence on position X_2. By retaining the relative velocity magnitude (5.28) in this region, we obtain the essential dependence of the transport coefficients required to avoid the spurious singularity at $X_2 = 0$ without resorting to an ad hoc local averaging of the shear-rate or imposition of a maximum

packing fraction.

Particle transport in the vorticity direction ($k = 3$) does not have a singular behavior because there is no drift velocity, so the local analysis presented in §5.3.1 is uniformly valid.

According to the derivation provided in Appendix D.1, the particle flux in the velocity gradient direction is given by

$$F_{i2}(X_2) = F_{i2}^{(c)}(X_2) + F_{i2}^{(\dot{\gamma})}(X_2)\,, \tag{5.32}$$

where the diffusive and drift fluxes are

$$F_{i2}^{(c)}(X_2) = -D_{i2}^{s}(X_2)\frac{dn_i}{dX_2} - \sum_{j=1}^{m}\left(D_{ij2}(X_2)\frac{dn_j}{dX_2}\right)\,, \tag{5.33}$$

$$F_{i2}^{(\dot{\gamma})}(X_2) = -\gamma_2' \, n_{i0} V_i(X_2)\,, \tag{5.34}$$

the diffusivities and drift-velocity-coefficient are

$$D_{i2}^{s}(X_2) = \gamma_2'|X_2| \sum_{j=1}^{m} n_{j0} I_{ij}^{(1)}(X_2)\,, \tag{5.35}$$

$$D_{ij2}(X_2) = \gamma_2'|X_2|\, n_{i0} I_{ij}^{(2)}(X_2)\,, \tag{5.36}$$

$$V_i(X_2) = \sum_{j=1}^{m} n_{j0} I_{ij}^{(3)}(X_2)\,, \tag{5.37}$$

and the integrals $I_{ij}^{(1)}, I_{ij}^{(2)}, I_{ij}^{(3)}$ are given by

$$\begin{aligned} I_{ij}^{(1)}(X_2) = \frac{1}{2}\frac{1}{|X_2|}\int_0^{\pi}\int_0^{r_c} r^{-\infty}\sin\theta \left[\int_0^{-\Delta X_2^{ij}} \left(\left|X_2^{i,-\infty} + \frac{1}{2}r^{-\infty}\sin\theta - X_2\right|\right.\right. \\ \left.\left. + \left|X_2^{i,-\infty} + \frac{1}{2}r^{-\infty}\sin\theta + X_2\right|\right) X_2^{i,-\infty} dX_2^{i,-\infty}\right] r^{-\infty} dr^{-\infty} d\theta\,. \end{aligned} \tag{5.38}$$

$$I_{ij}^{(2)}(X_2) = \frac{1}{2}\frac{1}{|X_2|}\int_0^{\pi}\int_0^{r_c} r^{-\infty}\sin\theta\left[\int_0^{-\Delta X_2^{ij}}\left(\left|X_2^{i,-\infty}+\frac{1}{2}r^{-\infty}\sin\theta - X_2\right|\right.\right.$$
$$\left.+\left|X_2^{i,-\infty}+\frac{1}{2}r^{-\infty}\sin\theta + X_2\right|\right) \tag{5.39}$$
$$\left.\left(x_2^{-\infty}+X_2^{i,-\infty}\right)dX_2^{i,-\infty}\right] r^{-\infty}dr^{-\infty}d\theta\,,$$

$$I_{ij}^{(3)}(X_2) = \frac{1}{2}\int_0^{\pi}\int_0^{r_c} r^{-\infty}\sin\theta\left[\int_0^{-\Delta X_2^{ij}}\left(\left|X_2^{i,-\infty}+\frac{1}{2}r^{-\infty}\sin\theta + X_2\right|\right.\right.$$
$$\left.\left.-\left|X_2^{i,-\infty}+\frac{1}{2}r^{-\infty}\sin\theta - X_2\right|\right)dX_2^{i,-\infty}\right] r^{-\infty}dr^{-\infty}d\theta\,, \tag{5.40}$$

where $(r^{-\infty},\theta)$ are the cylindrical coordinates defined in figure 5.1. Note that $-\Delta X_2^{ij} \geq 0$, as explained below Eq. (D.1.2). Carrying out the indicated $X_2^{i,-\infty}$ integrations in Eqs. (5.38)-(5.40) leads to Eqs. (D.1.9)-(D.1.11).

For $|X_2| \geq X_c^{ij}$, integrals (5.38)-(5.40) reduce to their local forms,

$$I_{ij}^{(1)} \to I_{ij2}^{A}\,, \qquad I_{ij}^{(2)} \to I_{ij2}^{A} + I_{ij2}^{B}\,, \qquad I_{ij}^{(3)} \to \mathrm{sign}(X_2)\,(I_{ij2}^{A} + \frac{1}{2}I_{ij2}^{B})\,, \qquad |X_2| \geq X_c^{ij}\,. \tag{5.41}$$

as shown in Appendix D.1. Accordingly, the transport coefficients (5.35)-(5.37) reduce to their corresponding local forms, Eqs. (5.17)-(5.19), with the shear-rate magnitude and its gradient given by Eqs. (5.26a,b).

An important observation is that $|X_2|I_{ij}^{(1)}$ and $|X_2|I_{ij}^{(2)}$ are even functions of X_2 and tend to a nonzero constant for $X_2 \to 0$, whereas $I_{ij}^{(3)}$ is an odd function and varies linearly for $X_2 \to 0$. Accordingly, the resulting drift velocity coefficient (5.37) varies linearly and the diffusivities have non-vanishing values for $X_2 \to 0$. Thus, particle

transport is governed by an equation of the form,

$$n\frac{dn}{dX_2} = -MX_2\, n^2\,, \qquad |X_2| \to 0\,, \tag{5.42}$$

instead of Eq. (5.31), yielding the nonsingular behavior $n \approx n_0 - \frac{1}{2}MX_2^2$, where $M > 0$ and n_0 is the number density at $X_2 = 0$. Hence, the source of the classical singular particle distribution, described above, is eliminated.

5.4 Stationary particle distributions: general results

The results are presented in this section are independent of the character of pairwise particle interactions. Specific results for particles that undergo short-range contact interactions are presented in §5.6.

5.4.1 One-dimensional particle distribution

First, we present a stationary solution for the particle distribution in a polydisperse suspension in a flow with a power-law shear-rate magnitude,

$$\dot{\gamma} = C_1 X_2^{\beta}\,, \tag{5.43}$$

where β and C_1 are arbitrary nonzero constants. Here, we restrict our attention to regions where the shear-rate is non-vanishing, thus $X_2 > 0$ is assumed.

Inserting Eqs. (5.14)-(5.19) into Eq. (5.8) yields

$$\sum_{j=1}^{m} \left(\dot{\gamma}\left[I^A_{ij2}\, n_j n_i' + \left(I^A_{ij2} + I^B_{ij2}\right) n_i n_j'\right] + \dot{\gamma}'\left[n_i n_j (I^A_{ij2} + \tfrac{1}{2} I^B_{ij2})\right]\right) = 0 \tag{5.44}$$

for $i = 1, 2, \cdots, m$, where primes are used to denote X_2-derivatives.

A power-law particle distribution

$$n_i(X_2) = c_i X_2^{-\beta/2}\,, \tag{5.45}$$

is seen to satisfy Eq. (5.44) with arbitrary coefficients c_i. This is a general result that holds independent of the details of pairwise particle interactions in a given system. Note that the effect of particle interactions exactly cancel, i.e., the spatial distribution of each particle species is unaffected by the presence of the others. This feature breaks down in regions where the shear-rate vanishes, as seen below.

5.4.2 Planar Poiseuille flow

Here, we consider the steady-state particle distribution in quadratic flows (5.25), including regions $X_2 \to 0$, where the shear-rate vanishes.

Polydisperse suspension

Inserting Eqs. (5.32)-(5.37) into Eq. (5.8) yields the equation governing the stationary particle distribution,

$$\sum_{j=1}^{m} \left(|X_2| \left[I_{ij}^{(1)}(X_2)\, n_j n_i' + I_{ij}^{(2)}(X_2)\, n_i n_j' \right] + I_{ij}^{(3)}(X_2)\, n_i n_j \right) = 0\,, \qquad |X_2| < X_c\,. \tag{5.46}$$

In a polydisperse system, each binary interaction has a distinct boundary layer half-thickness, X_c^{ij}, determined by Eq. (5.30), and X_c is the maximum of these, i.e.,

$$X_c = \sup\left\{X_c^{ij}\right\}\,. \tag{5.47}$$

For $|X_2| < X_c$, spatial distributions of particle species are coupled, unlike the situation considered in §5.4.1. However, Eq. (5.46) decouples in the outer region,

$|X_2| > X_c$, reducing to Eq. (5.44), according to Eq. (5.41), and thus obeys the distribution given by Eq. (5.45) with $\beta = 1$,

$$n_i(X_2) = c_i X_2^{-1/2}\,, \tag{5.48}$$

where constants c_i are determined by global boundary conditions for the problem. In principle, the constants are coupled through the boundary layer region but the coupling is weak in wide channels, as shown below.

Monodisperse particle distribution

For $m = 1$, Eq. (5.46) reduces to the linear equation,

$$\mathrm{D}(y)\bar{n}' + \mathrm{V}(y)\bar{n} = 0\,, \tag{5.49}$$

where the transport coefficients are

$$\mathrm{D}(y) = |y|\left(I_{11}^{(1)}(y) + I_{11}^{(2)}(y)\right)\,, \qquad \mathrm{V}(y) = I_{11}^{(3)}(y)\,. \tag{5.50a,b}$$

Here, the dimensionless variables are defined,

$$y = X_2/X_c\,, \qquad \bar{n} = n/n_c\,, \tag{5.51a,b}$$

where $n_c = n(X_c)$, and primes in Eq. (5.49) denote derivatives with respect to y. Integrating Eq.(5.49) and setting $\bar{n}(1) = 1$, consistent with Eq. (5.51b), yields

$$\bar{n}(y) = \exp\left(\int_{|y|}^{1} \frac{\mathrm{V}(t)}{\mathrm{D}(t)} dt\right)\,. \tag{5.52}$$

For $|y| > 1$, the transport coefficients (5.50) reduce to their local forms,

$$\mathrm{D}(y) = |y| \left(2I^A_{112} + I^B_{112}\right) , \qquad \mathrm{V}(y) = \mathrm{sign}(y) \left(I^A_{112} + \frac{1}{2} I^B_{112}\right) , \tag{5.53a,b}$$

according to Eq. (5.41), and thus

$$\bar{n}(y) = y^{-1/2} , \tag{5.54}$$

consistent with Eq. (5.48).

The number density, $n(X_c)$, used to define the dimensionless number density (5.51b), is determined by particle conservation,

$$q\, n_\infty = \int_0^{H_1} v(x) n(x) dx , \tag{5.55}$$

where n_∞ is the prescribed average number density, $v(x)$ is the velocity (5.27), $q = \frac{2}{3} V_0 H$ is the corresponding volume flow, and H is the half-width of the channel. The upper bound $H_1 = H - a$ used for the conservation relation (5.55) reflects the excluded volume within one radius of the channel walls.

Applying boundary condition (5.55) yields

$$\frac{n_c}{n_\infty} = \tfrac{5}{12} \epsilon^{-1/2} \left[1 - \tfrac{5}{8} \Delta\bar{n}\, \epsilon^{1/2} + O(\epsilon^2)\right]^{-1} , \tag{5.56}$$

where $\epsilon = X_c/H \approx a/H$ is assumed to be small compared to unity. The quantity $\Delta\bar{n}$ is the (average) deficit of particles in the center region compared to the singular distribution (5.54) obtained using local transport coefficients,

$$\Delta\bar{n} = -\int_0^1 \left[\bar{n}(y) - y^{-1/2}\right] dy . \tag{5.57}$$

Excluded volume at the walls of the channel affects the amplitude of the particle

distribution at $O(\epsilon^2)$, the same as the order of error as that induced by neglecting particle-wall hydrodynamic interactions. Details of the modified transport coefficients in the central region enter the conservation relation through the particle deficit, $\Delta\bar{n}$, and have a more slowly-decaying $O(\epsilon^{1/2})$ effect on the amplitude of the particle distribution in wide channels. To leading order, particle conservation is controlled by the outer region, according to Eqs. (5.54)-(5.56),

$$n_c = \tfrac{5}{12}\epsilon^{-1/2} n_\infty \,, \quad \text{and} \qquad n/n_\infty = \tfrac{5}{12}\tilde{y}^{-1/2} \,, \tag{5.58a,b}$$

where $\tilde{y} = X_2/H$, indicating that the particle distribution away from the center acquires the length set by the the channel width. In the wide-channel regime, the leading-order outer particle distribution in a polydisperse suspension has the corresponding form,

$$n_{ic} = \tfrac{5}{12}\epsilon^{-1/2} n_{i\infty} \,, \quad \text{and} \qquad n_i/n_{i\infty} = \tfrac{5}{12}\tilde{y}^{-1/2} \,, \tag{5.59a,b}$$

where $n_{i\infty}$ are the prescribed number densities of the particle species, and $n_{ic} = n_i(X_c)$. The result indicates that the distributions of particle species are decoupled from each other in the outer region, $|X_2| > X_c$.

5.5 Particle displacements

5.5.1 Contact interactions

Particles that undergo short-range symmetry-breaking "contact" interactions in shear-flow are considered here, specifically, particles with surface roughness, permeable particles, and emulsion drops. Pair trajectories of such particles are analytically integrated to yield formulas for binary cross-stream particle displacements ΔX_k^{12}, ΔX_k^{21} $(k = 2, 3)$ involving integrals of the standard pair mobility functions for spherical par-

ticles. Here, ΔX_k^{12} refers to the displacement of particle-1 resulting from its collision with particle-2 and visa versa for ΔX_k^{21}. The particles have radii a_1 and a_2, and the size ratio $\kappa = a_2/a_1 < 1$ is assumed. The particles are assumed to be non-Brownian and neutrally buoyant. Creeping flow conditions are considered, and particle inertia is neglected.

According to the usual model for rough particles, surface asperities with size d transmit a normal inter-particle contact force between rigid particles that prevents surface-to-surface particle separations less than d but do not exert a tensile force upon separation. Here, $\bar{\delta} = d/\bar{a}$ is the dimensionless roughness amplitude, $\bar{a} = (a_1 + a_2)/2$ is the average particle radius, and $\bar{\delta} \ll 1$ is assumed. Particle permeability is another short-range, symmetry-breaking mechanism. The dimensionless permeability is defined $\bar{K} = k/\bar{a}^2$, where k is the permeability and Darcy's law is used to describe the intraparticle flow. Weak permeability alleviates the lubrication pressure between particles, allowing particle contact, $h_0 = 0$, but otherwise has little effect on the pair interaction [55]. Under the assumption that the particles are rigid and not cohesive, the effect of weak permeability closely resembles small-amplitude particle roughness [191]. The small, flattened thin film that forms in the near-contact region between approximately spherical emulsion drops in apparent contact, $h_0 \approx 0$, under high-surface-tension-conditions is a third short-range mechanism that breaks the symmetry of pair trajectories. Slow drainage from the film prevents drop coalescence in the compressional quadrant of the flow [199–203]. The film quickly reverts as the drops rotate into the extensional quadrant of the flow and has little effect on their separation [151,193]. This model is characterized by a drop- to continuous-phase viscosity ratio, λ. Marangoni stresses are neglected.

Relative particle trajectories emanate from $x_1 \to -\infty$ $(+\infty)$ for $x_2^{-\infty} > 0$ (< 0) in the coordinate system defined by figure 5.2. Apart from the contact interactions, trajectories are accurately described using standard pair mobility functions for spherical

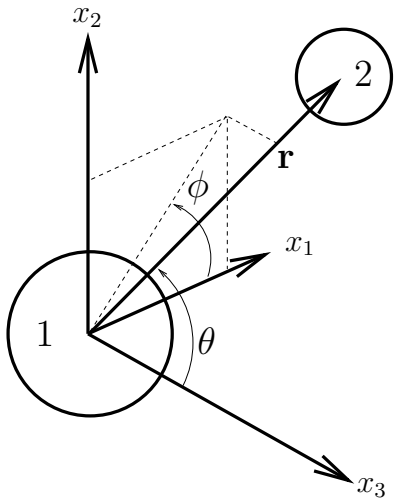

Figure 5.2: Spherical coordinate system for pair trajectories.

particles (or drops) in shear flow [87, 187, 188]. Accordingly, particles with short-range contact interactions have circular upstream collision cross-sections, defined by Eq. (5.22), where r_c^{12} depends on size ratio, and on the roughness, permeability, or drop- to continuous-phase viscosity ratio, respectively, for rough or permeable particles or drops [94, 189, 191]. Trajectories with offsets $r^{-\infty} > r_c^{12}$ are reversible, i.e., $\Delta X_k^{12} = \Delta X_k^{21} = 0$.

Pair trajectories with upstream trajectory offsets, $r^{-\infty} < r_c^{12}$, reach the contact surface, defined by $s = s^*$, where $s = r/\bar{a}$ is the center-to-center separation, r, normalized by the average particle radius. For permeable particles and high-surface-tension drops, $s^* = 2$; for particles with surface roughness, $s = 2 + \bar{\delta}$. On the contact surface, the particles undergo relative rotation through the compressional quadrant of the flow and separate at the equator ($\cos\phi = 0$), under the assumption that cohesive forces are absent. The motion on the contact surface is described by a subset of the trajectory equations corresponding to zero relative radial velocity. An example of a contacting pair trajectory for particles with surface roughness is illustrated in figure 5.3.

Below a critical roughness, the collision cross-section for rough particles vanishes;

similarly, there exists a critical permeability below which $r_c^{12} = 0$. The values of these critical parameters increase with diminishing size ratio [191, 204]. Likewise, drops have a critical viscosity ratio beyond which $r_c^{12} = 0$, and the critical viscosity ratio decreases with diminishing size ratio [200]. Equivalently, there exists a finite critical size ratio ratio, κ^*, below which $r_c^{12} = 0$ for fixed values of particle roughness or permeability, or drop viscosity ratio.

5.5.2 Particle trajectories

In a linear flow under creeping flow conditions, the trajectories of non-Brownian, neutrally-buoyant, inertialess particles with labels 1 and 2 are described by [186]

$$\mathbf{V}_1 = \mathbf{V}_1^{(\infty)} - \left[A_1(s)\hat{\mathbf{r}}\hat{\mathbf{r}} + B_1(s)\left(\mathbf{I} - \hat{\mathbf{r}}\hat{\mathbf{r}}\right)\right] \cdot \mathbf{E} \cdot \hat{\mathbf{r}} \tag{5.60}$$

and

$$\mathbf{V}_2 = \mathbf{V}_2^{(\infty)} - \left[A_2(s)\hat{\mathbf{r}}\hat{\mathbf{r}} + B_2(s)\left(\mathbf{I} - \hat{\mathbf{r}}\hat{\mathbf{r}}\right)\right] \cdot \mathbf{E} \cdot \hat{\mathbf{r}} \tag{5.61}$$

where, $\mathbf{r} = \mathbf{X}^{(2)} - \mathbf{X}^{(1)}$ is the vector between the particle centers as shown in figure 5.2, $\hat{\mathbf{r}} = \mathbf{r}/|\mathbf{r}|$ is a unit vector along the line-of-centers, $\mathbf{I}$ is the identity tensor, and $s = |\mathbf{r}|/\bar{a}$ is the center-to-center separation normalized by the average radius. The undisturbed particle velocities are $\mathbf{V}_i^{(\infty)} = \mathbf{E} \cdot \mathbf{X}^{(i)} + \boldsymbol{\omega} \times \mathbf{X}^{(i)}$ $(i = 1, 2)$, where $\mathbf{E}$ is the rate of strain, and $\boldsymbol{\omega}$ is the angular velocity. In simple shear flow,

$$\mathbf{E} = \dot{\gamma} \begin{pmatrix} 0 & 1/2 & 0 \\ 1/2 & 0 & 0 \\ 0 & 0 & 0 \end{pmatrix}, \qquad \boldsymbol{\omega} = \dot{\gamma} \begin{pmatrix} 0, & 0, & -1/2 \end{pmatrix}, \tag{5.62}$$

where $\dot{\gamma}$ is the magnitude of the local shear rate. In Eqs. (5.60) and (5.61), A_i and B_i $(i = 1, 2)$, respectively, are mobility functions that incorporate the effect of hydrodynamic interactions on the particle velocities parallel and normal to the line-

of-centers of the pair [87, 185–188]. Mobility functions depend also on the particle size ratio $\kappa = a_2/a_1$, and for spherical drops, also on the drop-to-continuous phase viscosity ratio, λ.

The particle displacements ΔX_k^{12} and ΔX_k^{21} $(k = 2, 3)$ are conveniently expressed in terms of relative and pair displacements, Δx_k and $\Delta \bar{x}_k$,

$$\Delta X_k^{12} = \frac{1}{2}(\Delta \bar{x}_k - \Delta x_k)\,, \qquad \Delta X_k^{21} = \frac{1}{2}(\Delta \bar{x}_k + \Delta x_k)\,, \tag{5.63}$$

where

$$x_k = X_k^{(2)} - X_k^{(1)}\,, \qquad \bar{x}_k = X_k^{(1)} + X_k^{(2)}\,, \tag{5.64}$$

are, respectively, the relative and pair positions.

On contacting trajectories (cf., figures 5.3-5.4), particles reach the contact surface (ii), move along the contact surface in the compressional quadrant of the flow (ii-iii) (dotted lines in figure 5.3), and separate at the edge of the compressional quadrant (iii), i.e., at $\phi = \pi/2$. A contact force prevents particle overlap on the contact-surface-portion of trajectories (ii-iii).

These segments of the relative and pair trajectories are analytically integrated below, treating the relative and pair motion separately. The former has been previously analyzed in classical works [186, 188], as indicated; integration of the pair trajectory is new. Both are presented below for completeness.

5.5.3 Trajectory integration

The relative motion of the particles are described by the trajectory equations [186],

$$\frac{ds}{dt} = (1-A)s\sin^2\theta\sin\phi\cos\phi \tag{5.65}$$

$$\frac{d\theta}{dt} = (1-B)\sin\theta\cos\theta\sin\phi\cos\phi \tag{5.66}$$

$$\frac{d\phi}{dt} = -\frac{1}{2}+\frac{1}{2}(1-B)\cos 2\phi\,, \tag{5.67}$$

where the spherical coordinates defined in figure 5.2 are used. The pair motion of the particles is described by

$$\frac{d\bar{x}_1}{dt} = \bar{x}_2 - \left[\frac{B_p\,x_2}{2}+(A_p-B_p)\,\frac{x_1^2\,x_2}{s^2}\right], \tag{5.68}$$

$$\frac{d\bar{x}_2}{dt} = -\left[\frac{B_p\,x_1}{2}+(A_p-B_p)\,\frac{x_1\,x_2^2}{s^2}\right], \tag{5.69}$$

$$\frac{d\bar{x}_3}{dt} = -(A_p-B_p)\,\frac{x_1\,x_2\,x_3}{s^2}. \tag{5.70}$$

Here, t is strain, and $\mathbf{x}$ and $\bar{\mathbf{x}}$, respectively, are the relative and pair positions (5.64). The relative and pair mobilities are $M = M_2 - M_1$ and $M_p = M_1 + M_2$, respectively, where $M = A$ or B. Only differences of the pair position, $\Delta\bar{\mathbf{x}}$, are significant, and by symmetry, we can restrict our attention to relative positions $\mathbf{x}$ in the positive quarter-plane. Accordingly, the initial conditions are

$$x_1^{(\mathrm{i})} = -\infty\,, \quad x_2^{(\mathrm{i})},\, x_3^{(\mathrm{i})} \geq 0\,; \qquad \bar{x}_1^{(\mathrm{i})} = \bar{x}_2^{(\mathrm{i})} = \bar{x}_3^{(\mathrm{i})} = 0\,. \tag{5.71a,b}$$

Integrating Eqs.(5.65)-(5.67) with initial conditions (5.71a) yields [94, 186]

$$x_2(s) = \varphi(s)\left[(x_2^{\infty})^2 + \Psi(s)\right]^{1/2}, \tag{5.72}$$

$$x_3(s) = x_3^\infty \, \varphi(s) \,, \tag{5.73}$$

$$x_1(s) = \mp \sqrt{s^2 - x_2^2 - x_3^2} \tag{5.74}$$

where x_2^∞ and x_3^∞ are the cross-flow coordinates of the far-field relative position of the particles at $s \to \infty$. The functions $\varphi(s)$ and $\Psi(s)$ are given by

$$\varphi(s) = \exp \left[\int_s^\infty \frac{A(s') - B(s')}{1 - A(s')} \frac{d\, s'}{s'} \right] , \tag{5.75}$$

and

$$\Psi(s) = \int_s^\infty \frac{B(s') s'}{[1 - A(s')]\, \varphi^2(s')} \, ds'. \tag{5.76}$$

The minus sign applies in Eq. (5.74) for $\pi/2 < \phi < \pi$; the + sign applies for $0 < \phi < \pi/2$.

Dividing Eqs.(5.69)-(5.70) by (5.65) and integrating yields the pair positions

$$\bar{x}_2(s) = \bar{x}_2^\infty + \bar{\Psi}(s, x_2^\infty) \,, \tag{5.77}$$

and

$$\bar{x}_3(s) = \bar{x}_3^\infty + \bar{\varphi}(s, x_3^\infty) \,, \tag{5.78}$$

where $\bar{x}_2^\infty$ and $\bar{x}_3^\infty$ are the corresponding coordinates of the far-field pair position. The functions $\bar{\varphi}(s, x_3^\infty)$ and $\bar{\Psi}(s, x_2^\infty)$ are defined

$$\bar{\varphi}(s, x_3^\infty) = \int_s^\infty \frac{[A_p(s') - B_p(s')]\, x_3(s', x_3^\infty)}{[1 - A(s')]\ s'} \, ds', \tag{5.79}$$

and

$$\bar{\Psi}(s, x_2^\infty) = \int_s^\infty \left[\frac{B_p(s')\, s'}{2\left[1 - A(s')\right]\, x_2(s', x_2^\infty)} + \frac{\left[A_p(s') - B_p(s')\right] x_2(s', x_2^\infty)}{\left[1 - A(s')\right]\, s'} \right] ds' \,, \quad (5.80)$$

where $x_2(s, x_2^\infty)$ and $x_3(s, x_3^\infty)$ are defined by Eqs. (5.72)-(5.73). The streamwise coordinate of the pair position, $\bar{x}_1$, does not affect the cross-flow particle distribution.

Trajectories on contact surface

On the contact surface $s = s^*$ in the compressional quadrant of the flow, the relative trajectory is described by setting the relative radial velocity to zero. The polar and azimuthal angles (θ, ϕ) evolve according to Eqs. (5.66)-(5.67) over the range,

$$\frac{\pi}{2} \leq \phi \leq \phi_0 \,, \quad (5.81)$$

where (θ_0, ϕ_0) is the initial point of contact (point (ii) in figures 5.3-5.4); separation occurs at $\phi = \pi/2$ (point (iii)). Dividing the two equations and integrating yields [205],

$$\theta_1(\phi) = \tan^{-1}\left(\tan\theta_0 \sqrt{\frac{1 - B_1^* \cos(2\phi_0)}{1 - B_1^* \cos 2\phi}} \right) \,, \quad (5.82)$$

where $B_1^* = 1 - B(s^*)$.

The pair motion on the contact surface is obtained by dividing Eqs. (5.69) and (5.70) by Eq. (5.67) and integrating the range (5.81) to yield,

$$\bar{x}_2^*(\phi) = \bar{x}_2^*(\phi_0) + \Omega(\phi) \,, \quad (5.83)$$

and

$$\bar{x}_3^*(\phi) = \bar{x}_3^*(\phi_0) + \chi(\phi) \,, \quad (5.84)$$

where the functions $\Omega(\phi)$ and $\chi(\phi)$ are defined by

$$\Omega(\phi) = \int_{\phi_0}^{\phi} \frac{[\hat{r}_3^2(\phi') - 1]\left[B_p^* \hat{r}_1(\phi') + 2(A_p' - B_p^*)\hat{r}_1(\phi')\hat{r}_2^2(\phi')\right]}{\frac{1}{2}B^*\left[2\,\hat{r}_2^2(\phi') + \hat{r}_3^2(\phi') - 1\right] - \hat{r}_2^2(\phi')}\, d\phi' \,, \tag{5.85}$$

and

$$\chi(\phi) = \int_{\phi_0}^{\phi} \frac{[\hat{r}_3^2(\phi') - 1]\left[2\,(A_p' - B_p^*)\hat{r}_1(\phi')\hat{r}_2(\phi')\hat{r}_3(\phi')\right]}{\frac{1}{2}B^*\left[2\,\hat{r}_2^2(\phi') + \hat{r}_3^2(\phi') - 1\right] - \hat{r}_2^2(\phi')}\, d\phi' \,. \tag{5.86}$$

Here, mobility functions B_p^* and B^* are evaluated at $s = s^*$; A_p' is the modified contact mobility, derived below, that encompasses the correction resulting from the action of the contact force. The relative position vector on the contact surface is given by

$$\hat{\mathbf{r}} = (\sin[\theta_1(\phi)]\cos\phi, \sin[\theta_1(\phi)]\sin\phi, \cos[\theta_1(\phi)]) \,, \tag{5.87}$$

where $\theta_1(\phi)$ is given by Eq. (5.82).

The contact force, F_c, that prevents particle overlap is determined by the force balance,

$$\mathbf{V}_{12} \cdot \hat{\mathbf{r}} = 2(1 - A^*)(\mathbf{E} : \hat{\mathbf{r}}\hat{\mathbf{r}}) - \frac{F_c}{\mu \bar{a}^2 \dot{\gamma}}\, G^* = 0 \,, \tag{5.88}$$

where μ is the continuous phase viscosity, and G^* is the relative radial mobility function evaluated at contact. The contact force modifies the pair velocity for unequal size particles,

$$\mathbf{V}_{12}^p \cdot \hat{\mathbf{r}} = -2A_p^*(\mathbf{E} : \hat{\mathbf{r}}\hat{\mathbf{r}}) - \frac{F_c}{\mu \bar{a}^2 \dot{\gamma}}\, G_p^* \,, \tag{5.89}$$

where G_p^* is the pair radial mobility function evaluated at contact. Substituting the normal force derived from Eq. (5.88) into (5.89) yields

$$\mathbf{V}_{12}^p \cdot \hat{\mathbf{r}} = -2A_p'(\mathbf{E} : \hat{\mathbf{r}}\hat{\mathbf{r}}) \,, \tag{5.90}$$

where $A_p' = A_p^* + (1 - A^*)G_p^*/G^*$ is the modified axisymmetric pair mobility that appears in formulas (5.85)-(5.86) [198]. The modified mobility represents a higher-

order correction, e.g., an $O(\bar{\delta})$ correction for rough particles. A contact force is not calculated for drops because $1 - A^* = 0$.

Examples of trajectories on the contact surface

Examples of contacting trajectories are shown in figures 5.3-5.4. For moderate viscosity ratios, drops have considerably larger collision cross-sections and correspondingly larger displacements than rough particles, as seen in figure 5.4. Drop trajectories also deflect more in the vorticity direction.

Models for rough particles include a coefficient of friction to describe tangential forces transmitted by surface asperities at contact, $h_0 = d$ [102,103,189]. The limiting cases of zero- or infinite-friction-coefficient correspond, respectively, to evaluating the contact tangential mobility as $B^* = B(2 + \bar{\delta})$ or as $B^* = B(2)$. Similar predictions are obtained in these two limits, as seen in figure 5.4b (compare solid and dash-dotted lines). An explanation for this finding is the dominant role of the viscous lubrication resistance. The zero-friction-coefficient model was used for all subsequent rough-particle calculations presented herein.

Recently, the following hydrodynamic equivalence between particle roughness and particle permeability was proposed [55],

$$\bar{\delta} \longleftrightarrow .7224\, \nu^{1/5} \bar{K}^{2/5}\,. \tag{5.91}$$

where $\bar{\delta}$ and $\bar{K}$ are the dimensionless particle roughness and permeability (i.e., nondimensionalized by the average drop radius), and $\nu = 2\kappa/(1+\kappa)^2$. This relation is based on the contact time between particles under the action of a constant force. It was subsequently found to hold accurately for colliding pair trajectories in several types of flow, including shear flow for a wide range of size ratios [191]. The trajectory for permeable particles shown in figure 5.4b (dotted line) lies between the two trajecto-

ries corresponding to zero and infinite friction and supports the use of relation (5.91) also for trajectories on the contact surface. It follows that particle displacements, and thus particle transport, of permeable particles can be inferred from results for rough particles.

5.5.4 Net cross-flow displacements

The indefinite trajectory integrals derived in §5.5.3 are combined here to yield formulas for the net relative- and pair-displacements in terms of the pair mobility functions. The relative and pair trajectory segments, (i-ii), (ii-iii), and (iii-iv) are schematically shown in figure 5.3.

From Eqs. (5.72)-(5.73), the relative cross-flow position at the contact point is

$$x_2^{(\mathrm{ii})} = \varphi^* \left[\left(x_2^{(\mathrm{i})} \right)^2 + \Psi^* \right]^{1/2}, \qquad x_3^{(\mathrm{ii})} = \varphi^* x_3^{(\mathrm{i})}, \tag{5.92a,b}$$

where φ^* and Ψ^* are the functions (5.75)-(5.76) evaluated on the contact surface, $s = s^*$, and $\mathbf{x}^{(\mathrm{i})}$ is the initial condition (5.71a). The polar and azimuthal angles at the initial contact point (θ_0, ϕ_0), are given by

$$2\cos\theta_0 = x_3^{(\mathrm{ii})}, \qquad 2\sin\theta_0 \sin\phi_0 = x_2^{(\mathrm{ii})}. \tag{5.93a,b}$$

The separation point is given by

$$x_2^{(\mathrm{iii})} = 2\sin\left[\theta_1\left(\frac{\pi}{2}\right)\right] \qquad x_3^{(\mathrm{iii})} = 2\cos\left[\theta_1\left(\frac{\pi}{2}\right)\right], \tag{5.94a,b}$$

where $\theta_1(x)$ is the function (5.82). The final relative position of the particles in the

cross-flow plane is

$$x_2^{(\mathrm{iv})} = \left[\left(\frac{x_2^{(\mathrm{iii})}}{\varphi^*}\right)^2 - \Psi^*\right]^{1/2}, \qquad x_3^{(\mathrm{iv})} = \frac{x_3^{(\mathrm{iii})}}{\varphi^*}\,. \tag{5.95a,b}$$

The displacement relations for the pair motion are obtained from Eqs.(5.77)-(5.78) and (5.83)-(5.84), yielding the pair position

$$\bar{x}_2^{(\mathrm{ii})} = \bar{\Psi}^*(x_2^{(\mathrm{i})})\,, \qquad \bar{x}_3^{(\mathrm{ii})} = \bar{\varphi}^*(x_3^{(\mathrm{i})})\,, \tag{5.96a,b}$$

where $\bar{\varphi}^*$ and $\bar{\Psi}^*$ are the functions (5.79)-(5.80) evaluated at $s = s^*$. Note that $\bar{\mathbf{x}}^{(\mathrm{i})} = 0$, according to initial condition (5.71b). The separation point is

$$\bar{x}_2^{(\mathrm{iii})} = \bar{x}_2^{(\mathrm{ii})} + \Omega\left(\frac{\pi}{2}\right), \qquad \bar{x}_3^{(\mathrm{iii})} = \bar{x}_3^{(\mathrm{ii})} + \chi\left(\frac{\pi}{2}\right), \tag{5.97a,b}$$

where $\Omega(x)$ and $\chi(x)$ are the functions (5.85)-(5.86). The final cross-flow pair position is

$$\bar{x}_2^{(\mathrm{iv})} = \bar{x}_2^{(\mathrm{iii})} + \bar{\Psi}^*(x_2^{(\mathrm{iii})})\,, \qquad \bar{x}_3^{(\mathrm{iv})} = \bar{x}_3^{(\mathrm{iii})} + \bar{\varphi}^*(x_3^{(\mathrm{iii})})\,. \tag{5.98a,b}$$

Particle displacements

Combining Eq. (5.95a,b) and using $\left(x_2^{(\mathrm{iii})}\right)^2 + \left(x_3^{(\mathrm{iii})}\right)^2 = (s^*)^2$, we obtain the radius of the upstream collision cross-section,

$$r_c^{12} = \left[\left(\frac{s^*}{\varphi^*}\right)^2 - \Psi^*\right]^{1/2}. \tag{5.99}$$

which is related to the collision efficiency, E_{12}, by

$$\frac{r_c^{12}}{\bar{a}} = 2E_{12}^{1/3}. \tag{5.100}$$

Collision efficiencies for rough and permeable particles and drops are available in the literature [191, 200].

Net displacements of each particle are determined by combining the above results to obtain the net relative and pair displacements,

$$\Delta x_k = x_k^{(\mathrm{iv})} - x_k^{(\mathrm{i})}\,, \qquad \Delta \bar{x}_k = \bar{x}_k^{(\mathrm{iv})} - \bar{x}_k^{(\mathrm{i})}\,, \tag{5.101}$$

and inserting them into Eq. (5.63). Note that $\bar{x}_k^{(\mathrm{i})} = 0$, according to Eq. (5.71b). Examples of individual particle displacements are shown by the contour maps in figures 5.5 and 5.6. By the symmetry relations (5.5)-(5.6), only a quarter of the cross-flow plane is shown.

For contact interactions between pairs of inertialess particles in creeping flows, the maximum displacement magnitudes are achieved for $r^{-\infty} \to 0$ and satisfy

$$\Delta X_{2,\max}^{12} + \Delta X_{2,\max}^{21} = r_c^{12}\,. \tag{5.102}$$

Bounds for the magnitudes of the individual particle displacements are given by

$$0 < \Delta X_{2,\max}^{12} \leq \frac{1}{2} r_c^{12}\,, \qquad \frac{1}{2} r_c^{12} \leq \Delta X_{2,\max}^{21} < r_c^{12}\,, \qquad 0 < \kappa \leq 1\,. \tag{5.103}$$

For equal size particles,

$$\Delta X_{2,\max}^{12} = \Delta X_{2,\max}^{21} = \frac{1}{2} r_c^{12}\,, \qquad \kappa = 1\,, \tag{5.104}$$

and for the limiting case of extreme size ratio, we have

$$\Delta X_{2,\max}^{12} \to 0\,, \qquad \Delta X_{2,\max}^{21} \to r_c^{12}\,, \qquad \kappa \to 0\,. \tag{5.105}$$

Figures 5.7 and 5.8 show maximum particle displacements as a function of size ratio,

and illustrate relations (5.102)-(5.105). Together, the results in figures 5.5-5.8 show that drops have larger collision cross-sections and undergo larger displacements than rough particles. Pair collisions displace the smaller particle much more than the larger, even for modest size ratios. Particle displacements in the velocity gradient direction are considerably larger than in the vorticity direction, especially for rough particles.

Boundary layer thickness

Given that relation (5.102) is attained for $r^{-\infty} \to 0$ and $\Delta X_2^{12} = \Delta X_2^{21} = 0$ for $r^{-\infty} = r_c^{12}$, suggests that Eq. (5.30) can be replaced by the tighter bound,

$$X_c^{ij} = \max\left(\Delta X_{2,\max}^{ij}, \frac{1}{2} r_c^{ij}\right) \tag{5.106}$$

for particles that undergo contact interactions, where the indices $ij = 12$ or 21. Our results do not depend on this relation but our calculations support it. The relation is used here to discuss the width of the boundary layer, X_c, that forms where the shear-rate vanishes.

In a monodisperse suspensions, the boundary layer thickness is set by the collision cross-section, according to Eq. (5.104),

$$X_c = \frac{1}{2} r_c \,, \tag{5.107}$$

where r_c is used here to denote the collision cross-section for equal-size spheres which depends on particle roughness or permeability or the drop viscosity ratio. Below the critical values of these parameters, $r_c = 0$, and particle structuring is not predicted.

In a bidisperse suspension,

$$X_c = \max\left(\Delta_{2,\max}^{21}, \frac{1}{2} \bar{r}_c \, a_1\right) \,, \tag{5.108}$$

given that $X_c^{21} \geq X_c^{12}$, according to Eq. (5.103). Here, $\bar{r}_c$ is the collision cross-section for equal-size spheres nondimensionalized by the sphere radius. The results shown in figures 5.7 and 5.8 indicate that the boundary layer thickness is controlled by heterogeneous pair interactions (i.e., $\Delta_{2,\max}^{21} > r_c$) for moderate size ratios, and by the collision cross-section of the larger particles closer to the critical size ratio, κ^*. For $\kappa < \kappa^*$, the bidisperse particle distribution reduces to a superposition of monodisperse distributions with boundary layer thicknesses, $a_1\bar{r}_c$ and $a_2\bar{r}_c$.

5.6 Particle distributions in Poiseuille flow: particles with contact interactions

Stationary particle distributions are presented here for suspensions in planar Poiseuille flow (5.27) for systems with particles that undergo contact interactions using the analysis developed in §5.5. The results here are specific examples of the results presented in §5.4 for the case of rough particles and emulsion drops, and for permeable particles through relation (5.91). Variables used in this section are made dimensionless using the thickness of the boundary layer region at the center of the channel, X_c, defined by Eq. (5.47).

5.6.1 Particle distribution in monodisperse suspension

Figures 5.9-5.11 show, respectively, transport coefficients (5.50), stationary particle distributions (5.52), and the average particle deficit (5.57) in the central, boundary layer region of the flow. The variables defined by Eq. (5.51) are used, and the transport coefficients are nondimensionalized using the characteristic length, X_c, which is given by Eq. (5.107). Integrals (D.1.9)-(D.1.11), required for the transport coefficients, were numerically evaluated with particle displacements, $\Delta X_2^{12} = -\Delta X_2^{21}$, obtained by quadratures of mobility functions, as described in §5.5.4; particle distri-

butions were obtained by evaluating Eq. (5.52).

The results shown in figure 5.9 demonstrate that the drift velocity but not the diffusion coefficient, defined by Eq. (5.50), vanishes at the center of the channel, where the shear-rate vanishes, and shows the corresponding odd and even symmetries of these quantities. As discussed at the end of §5.3.2, these are the essential features of the transport coefficients that avoid the classical particle distribution singularity at points of vanishing shear rate. The dashed lines depict the local form of the transport coefficients (5.53) for $|y| > 1$.

Examples of particle distributions for rough particles and emulsion drops are shown in figure 5.10; the results are barely distinguishable. Similar results were obtained for other values of roughness and viscosity ratios. Moreover, the average particle deficit in the boundary layer compared to the singular outer solution (5.57) is almost constant according to the results shown in figure 5.11. The boundary layer thickness (5.107) is determined by the details of the contact interactions between particles, through their effect on the collision cross-section, but the rescaled particle distribution in the boundary layer is insensitive to these details.

5.6.2 Particle distribution in bidisperse suspension

The stationary particle distributions in a binary mixture are governed by

$$\left(\mathrm{D}_{11}^{(1)}(y)\,\hat{n}_1 + \mathrm{D}_{11}^{(2)}(y)\,\hat{n}_2\right)\hat{n}_1' + \mathrm{D}_{12}(y)\,\hat{n}_1\hat{n}_2' + \left(\mathrm{V}_{11}(y)\,\hat{n}_1 + \mathrm{V}_{12}(y)\,\hat{n}_2\right)\hat{n}_1 = 0\,, \quad (5.109)$$

$$\mathrm{D}_{21}(y)\,\hat{n}_2\hat{n}_1' + \left(\mathrm{D}_{22}^{(1)}(y)\,\hat{n}_1 + \mathrm{D}_{22}^{(2)}(y)\,\hat{n}_2\right)\hat{n}_2' + \left(\mathrm{V}_{21}(y)\,\hat{n}_1 + \mathrm{V}_{22}(y)\,\hat{n}_2\right)\hat{n}_2 = 0\,, \quad (5.110)$$

as obtained from Eq.(5.46) for $m = 2$, where the transport coefficients are given by

$$\mathrm{D}_{ii}^{(i)}(y) = |y| \left(I_{ii}^{(1)}(y) + I_{ii}^{(2)}(y) \right) , \qquad \mathrm{D}_{ii}^{(j)}(y) = |y| I_{ij}^{(1)}(y) , \tag{5.111}$$

$$\mathrm{D}_{ij}(y) = |y| I_{ij}^{(2)}(y) , \qquad \mathrm{V}_{ij}(y) = I_{ij}^{(3)}(y) . \tag{5.112}$$

Here, y is defined by Eq. (5.51 a) with X_c given by Eq. (5.47), and the primes denote derivatives with respect to y. The dimensionless number densities are defined

$$\hat{n}_i = n_i / n_c , \tag{5.113}$$

where n_c is the total number density at $y = 1$, i.e., $n_c = n_{1c} + n_{2c}$, by analogy to Eq. (5.51 b).

Equations (5.109)-(5.110) are nonlinear (quadratic) equations for $\hat{n}_1$ and $\hat{n}_2$ but only ratios of number densities are significant; the total number density is not significant because the suspension volume does not enter. Likewise, only relative volume fractions, $\hat{\phi}_i$ at $y = 1$, not the total volume fraction, ϕ_c, are significant,

$$\hat{\phi}_i = n_{ic} v_i / \phi_c , \qquad \phi_c = \sum_{j=1}^{m} n_{jc} v_j , \tag{5.114}$$

where v_i is volume of a type-i particle. It follows that Eqs. (5.109)-(5.110) can be solved with boundary conditions,

$$\hat{n}_1(1) = \frac{\hat{\phi}_1 \kappa^3}{\hat{\phi}_1 \kappa^3 + \hat{\phi}_2} , \qquad \hat{n}_2(1) = \frac{\hat{\phi}_2}{\hat{\phi}_1 \kappa^3 + \hat{\phi}_2} , \tag{5.115}$$

where $\kappa = a_2/a_1$ is the size ratio. Given the proportionality (5.59) between n_{ic} and the average number densities, $n_{i\infty}$, the foregoing normalization is equivalent to using the average number densities and volume fractions instead of the values at $y = 1$.

Particle distributions were obtained by numerical integration of the system (5.109)-

(5.110) with boundary conditions (5.115) from $y = 1$ to $y = 0$, evaluating the integrals (D.1.9)-(D.1.11) that enter the transport coefficients (5.111)-(5.112) with ΔX_2^{ij} obtained by quadratures of mobility functions.

For the purposes of presentation and discussion, it is convenient to define number densities normalized by their individual values, rather than the total number density, at the edge of the outer region, i.e.,

$$\bar{n}_i = \frac{\hat{n}_i}{\hat{n}_i(1)} = \frac{n_i}{n_{ic}} \,. \tag{5.116}$$

For $y > 1$, we have

$$\bar{n}_i(y) = y^{-1/2} \,, \tag{5.117}$$

according to Eq. (5.48).

The relative enrichment of type-i particles in a polydisperse suspension at the center of Poiseuille flow is defined,

$$\Delta\bar{n}_i = \int_0^1 \left[\bar{n}_i(y) - \bar{n}(y)\right] dy \,, \tag{5.118}$$

where $\bar{n}$ is the distribution in a monodisperse suspension (5.52). Note that for $y > 1$, $\bar{n}_i(y) - \bar{n}(y) = 0$ by Eqs. (5.54) and (5.117).

Figure 5.12 shows results for particle distributions in a bidisperse system of rough particles and emulsion drops, including the predictions of separate, non-interacting monodisperse distributions (5.52).

Figures 5.13-5.14 provide a parametric study of the relative enrichment at the center of planar Poiseuille flow for bidisperse suspensions. Enrichment of larger particles is seen for rough particles at all size ratios in part (a) of both figures, whereas smaller particles are enriched for small size ratios and depleted for larger; the particle distributions in figures 5.12a-b illustrate each regime. These predictions concur with

experimental observations that generally show enrichment of larger particles [167,168] but also enrichment of smaller particles in some systems [169]. By contrast, emulsions show a depletion of larger drops and an enhancement of smaller drops for most of the parameter range, as seen in part (b) of figures 5.13-5.14. Figure 5.12c illustrates a typical drop distribution.

The relative volume fraction, $\hat{\phi}_2$, modulates the magnitude of enrichment and depletion in suspensions of particles and drops but has less effect on selection, i.e., which particle is enriched, according to the results shown in figure 5.13.

The particle roughness parameter, $\delta_1 = d/a_1$, and the viscosity ratio, λ, determine the collision cross-section and thus the critical size ratio, κ^*, below which no contact interactions occur. Accordingly, $\Delta\bar{n}_i = 0$ for $\kappa < \kappa^*$, as seen in figure 5.14. The viscosity ratio λ also modulates the magnitude of enrichment and depletion as seen in part (b) of this figure. Particle roughness has a weaker effect on the magnitude of enrichment and depletion; figure 5.14a shows that the enrichment of large particles is almost independent of roughness. This finding may explain the consistency of reports on the enrichment of large particles in bidisperse suspensions [163–169].

5.7 Conclusions

In this chapter we present a pairwise theory for particle distributions in suspensions undergoing 2d unidirectional flows, including planar Poiseuille and shear flows. General results from our analysis include a steady-state solution for the particle distribution in a polydisperse suspension subjected to a power-law shear-rate profile, and a boundary layer analysis for regions where the shear rate vanishes. A power-law particle distribution is attained in a power-law shear rate with an exponent equal to half of the shear-rate exponent and the distribution for each particle species is unaffected by the presence of the others. The treatment of the boundary layer avoids

the singular distribution that is usually predicted. The radius of the collision cross-section emerges as the relevant length scale, and a local analysis of particle transport is valid immediately outside this region. These results hold for systems with arbitrary symmetry-breaking pair interactions between particles.

Pair displacements for hydrodynamically-interacting particles that undergo short-range interactions were reduced to quadratures of mobility functions for spherical particles or drops. This result qualitatively advances the computational efficiency of these calculations, making feasible computations that explore the three-dimension parameter space that quantitatively describes relative enrichment in bidisperse suspensions, albeit for particles with comparatively simple pair interactions. The computations for each point in figures 5.13-5.14 require approximately 10^6 particle trajectories each.

The scale of the particle distribution in monodisperse suspensions is set by the collision cross-section of particles but its shape, i.e., the rescaled distribution, is almost independent of particle roughness, permeability, or drop viscosity ratio.

Results for bidisperse suspensions show that the enrichment of the larger particles at the center of Poiseuille flow is a robust result, holding for the entire parameter space, including particle size ratio, relative volume fraction, and surface roughness. Small particles are enriched for smaller size ratios and depleted for larger. These findings are in agreement with the available data [167–169]. Permeable particles can be expected to follow the same trends through the established equivalence of permeability and surface roughness [191]. By contrast, drops with mobile interfaces show robust enrichment of smaller drops and depletion of larger ones at the center of the flow with the exception of high-viscosity, nearly-equal-size drops that reverse this trend.

The magnitudes of enrichment and depletion of particle species in bidisperse suspensions are small in most cases, especially for rough particles. This observation suggests that a perturbation analysis may be useful with number densities of particle

species expressed as $\bar{n}_i = \bar{n}_i^{(0)} + \bar{n}_i^{(1)}$ $(i = 1, 2)$, where $\bar{n}_i^{(0)}$ is the number densities in a monodisperse suspension of type-i particles and $\bar{n}_i^{(1)}$ is the perturbation resulting from heterogeneous ij pair interactions with $\bar{n}_i^{(1)} \ll \bar{n}_i^{(0)}$ assumed. The simpler linear system governing the perturbations $\bar{n}_i^{(1)}$ may help to explain the observed trends of relative enrichment and depletion discussed above.

The time evolution of particle distributions and the possible effect of initial conditions [169] on the resulting stationary particle distributions, and the effect of cross-streamline trajectories [171, 206] induced by wall interactions in smaller channels are other phenomena that remain to be explored.

Note

The authors are grateful to Dr. A. Z. Zinchenko [63] for the use of his bispherical coordinate code for computing pair mobilities of impermeable spheres.

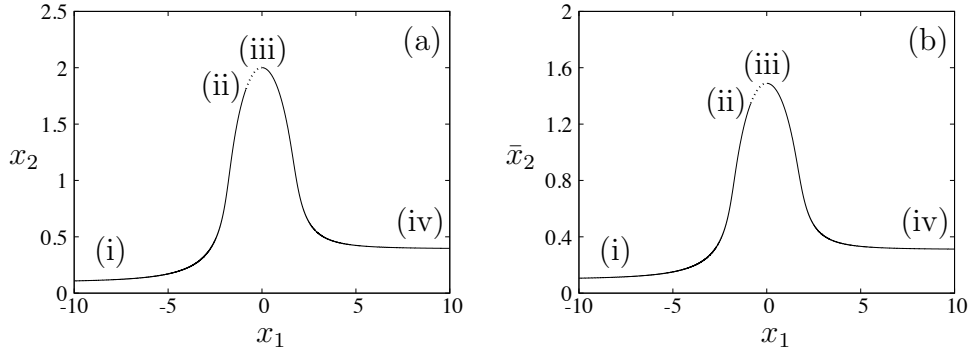

Figure 5.3: Relative (a) and pair (b) particle trajectories; $\kappa = a_2/a_1 = 1/2$, $\bar{\delta} = 10^{-3}$, $\mathbf{x}^{(-\infty)} = (0.1, 0)$ (solid lines); initial positions (i), contact surface (ii)-(iii) (dotted lines), final positions (iv).

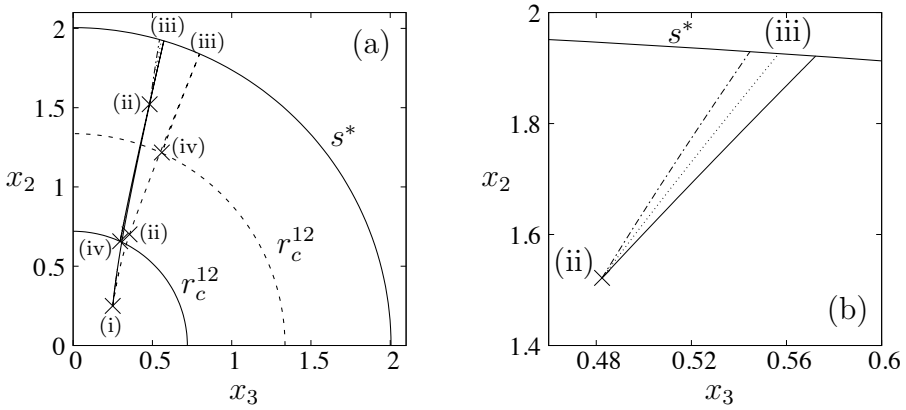

Figure 5.4: (a) Relative trajectory $\mathbf{x}^{(-\infty)} = (.25, .25)$, $\kappa = 1/2$; rough particles $\bar{\delta} = 5 \times 10^{-3}$, zero contact friction (solid lines), infinite contact friction coefficient (dash-dotted lines); permeable particles $\bar{K} = 6 \times 10^{-6}$ from Eq.(5.91) (dotted lines); drops $\lambda = 1$ (dashed lines); initial offset (i), contact surface (ii)-(iii), final offset (iv); collision surface $s = s^*$ (large circle), collision cross-sections r_c^{12} particles (small circle), drops (dashed circle). (b) Enlargement of particle trajectories on contact surface.

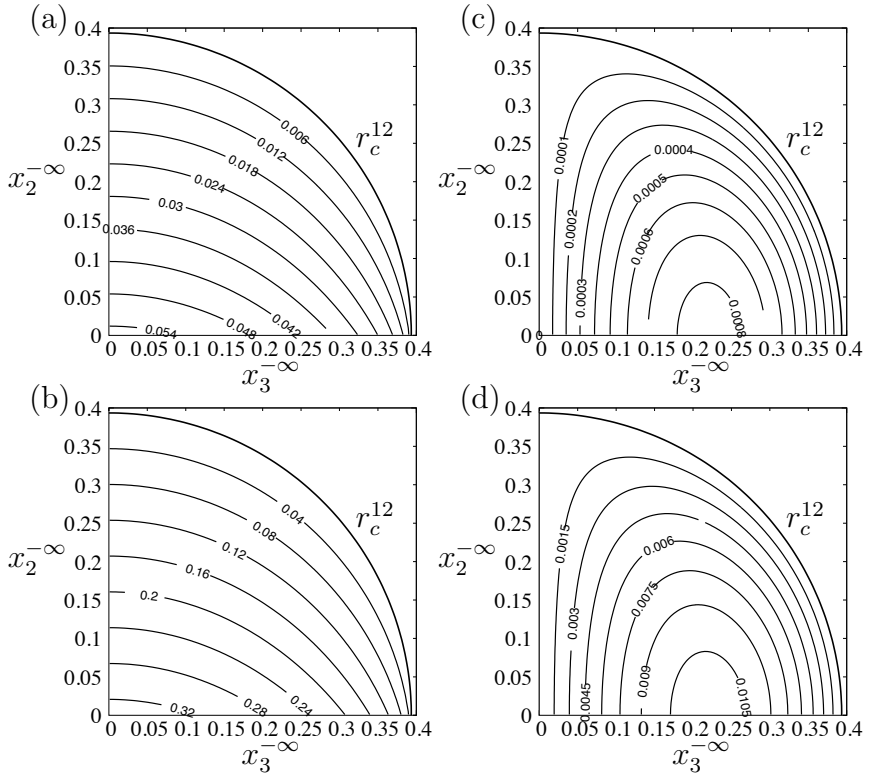

Figure 5.5: Displacement magnitudes of (a) larger and (b) smaller particles in velocity gradient direction, and (c) larger and (d) smaller particles in vorticity direction; $\kappa = 1/2$, $\bar{\delta} = d/\bar{a} = 10^{-3}$. Displacements and cross-flow coordinates nondimensionalized by the average radius; radius of collision cross-section, r_c^{12}, indicated by outermost quarter circle.

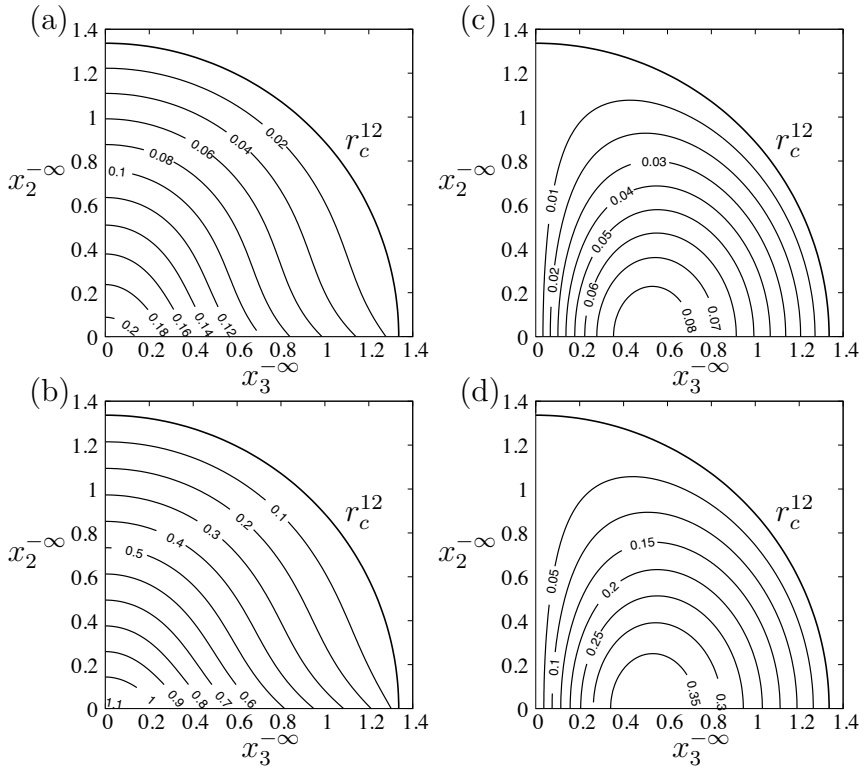

Figure 5.6: Same as figure 5.5, except for drops, $\lambda = 1$.

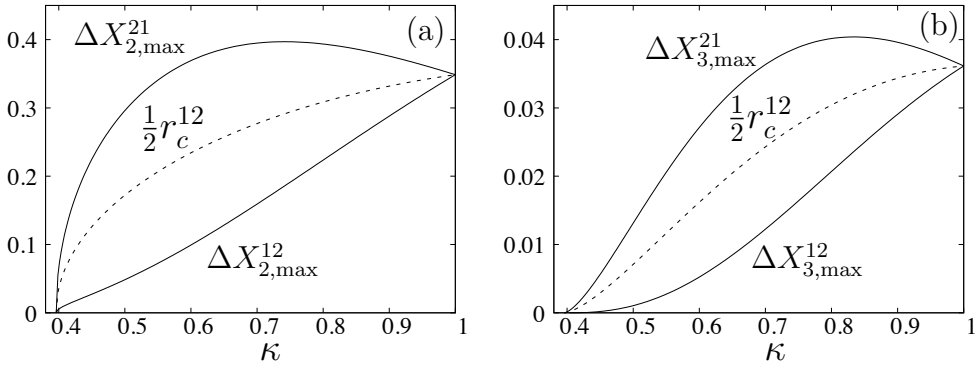

Figure 5.7: Maximum particle displacement magnitudes (solid lines) for rough particles, $\delta_1 = d/a_1 = 10^{-3}$, versus size ratio, $\kappa = a_2/a_1$, (a) in the velocity gradient direction and (b) in the vorticity direction; average of maximum displacement magnitudes (dashed lines); particle displacements and collision cross-section nondimensionalized by radius of larger particle a_1.

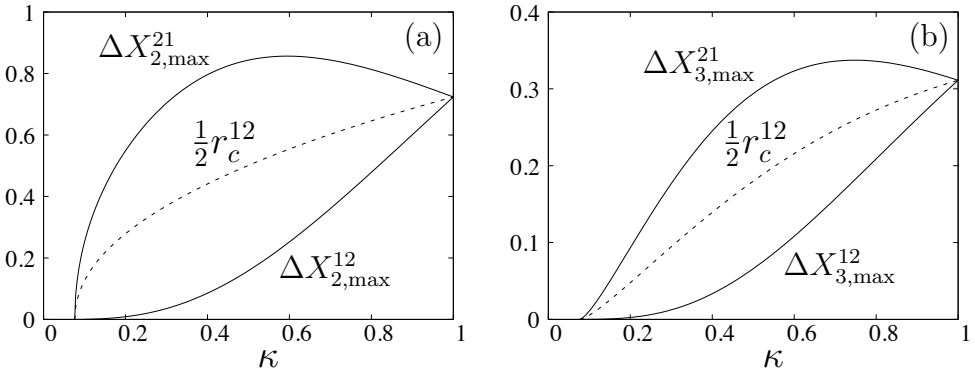

Figure 5.8: Same as figure 5.7, except for drops, $\lambda = 1$.

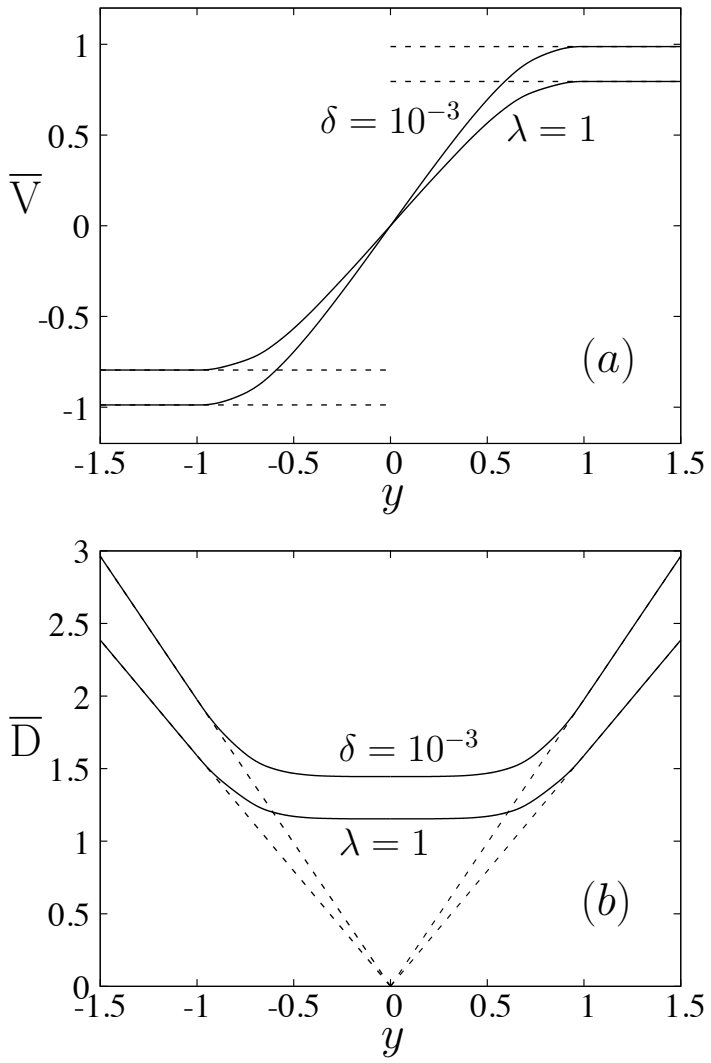

Figure 5.9: Dimensionless drift (a) and diffusive (b) transport coefficients $\overline{\mathrm{D}} = DX_c^{-6}$ and $\overline{\mathrm{V}} = VX_c^{-5}$ (5.50) for monodisperse suspensions of particles with roughness $\delta = d/a$ and drops with viscosity ratio λ, as indicated (solid lines); outer forms of transport coefficients (5.53) (dashed lines).

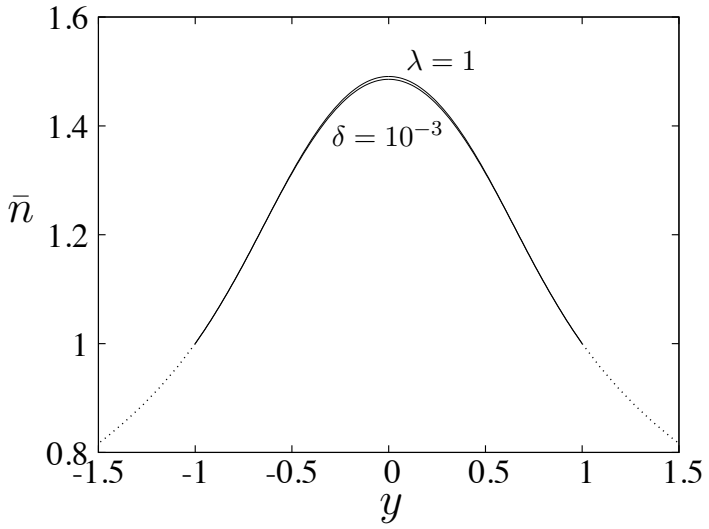

Figure 5.10: Particle distribution (5.52) for monodisperse suspension of particles with roughness $\delta = d/a$ and drops with viscosity ratio, λ, as indicated (solid lines); outer form given by Eq. (5.54) (dotted lines).

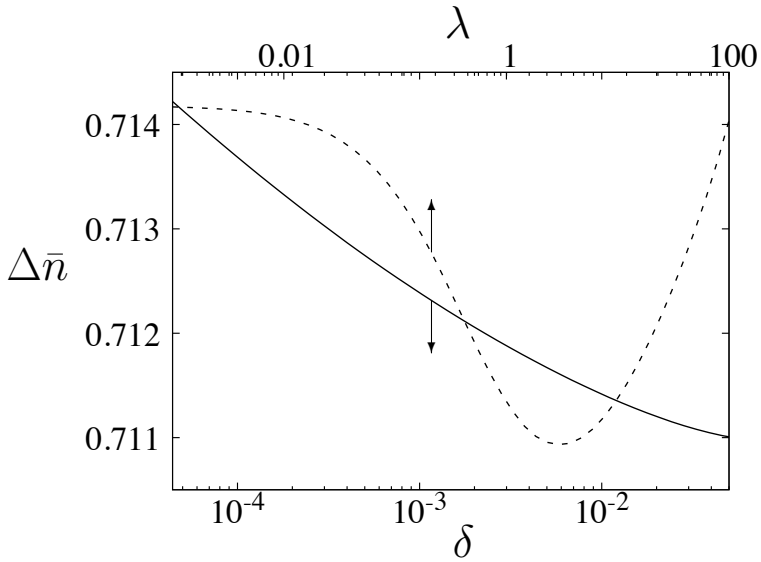

Figure 5.11: Average deficit of particles in the boundary layer (5.57) for monodisperse suspensions of particles with roughness $\delta = d/a$ (solid line) and drops with viscosity ratio λ (dashed line).

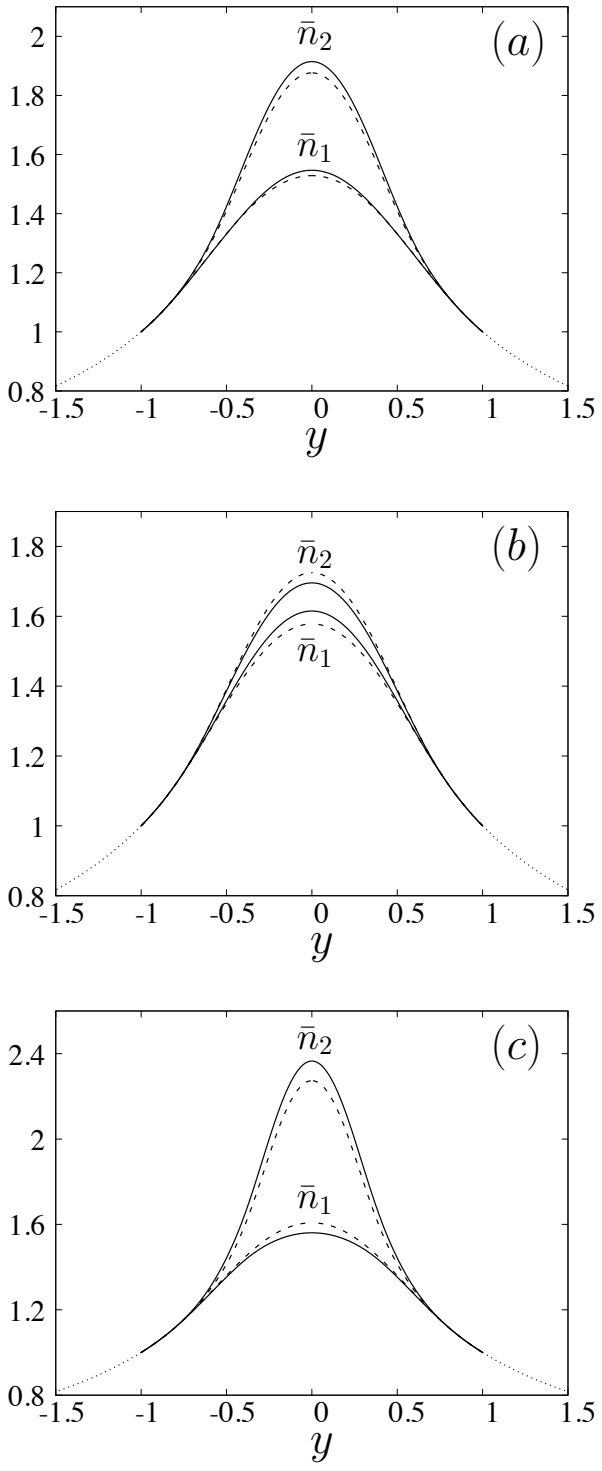

Figure 5.12: Bidisperse particle distributions with equal relative volume fractions, $\hat{\phi}_2 = 1/2$ (solid lines); rough particles, $\delta_1 = d/a_1 = 10^{-3}$, (a) $\kappa = .6$, (b) $\kappa = .8$; (c) drops, $\kappa = 1/2$, $\lambda = 1$; monodisperse solutions (5.52) (dashed lines), outer solution (5.54) (dotted lines).

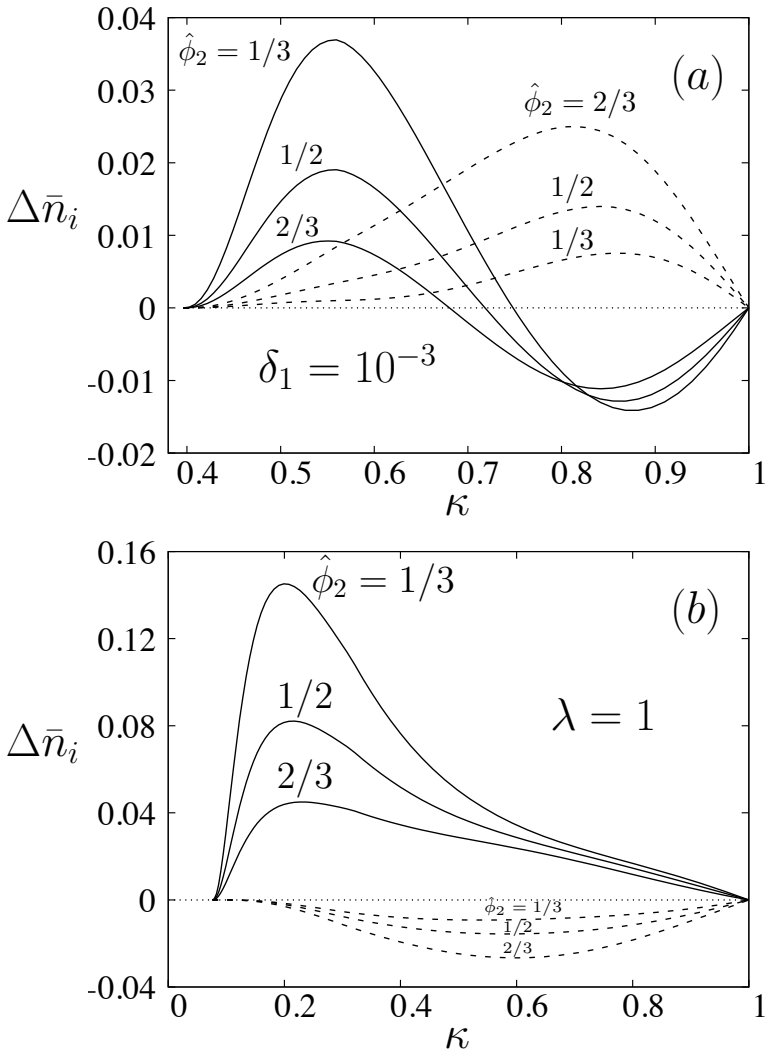

Figure 5.13: Relative enrichment (5.118) for large (dashed lines) and small (solid lines) particles, $\hat{\phi}_2$ as indicated; (a) particles, $\delta_1 = d/a_1 = 10^{-3}$, (b) drops, $\lambda = 1$.

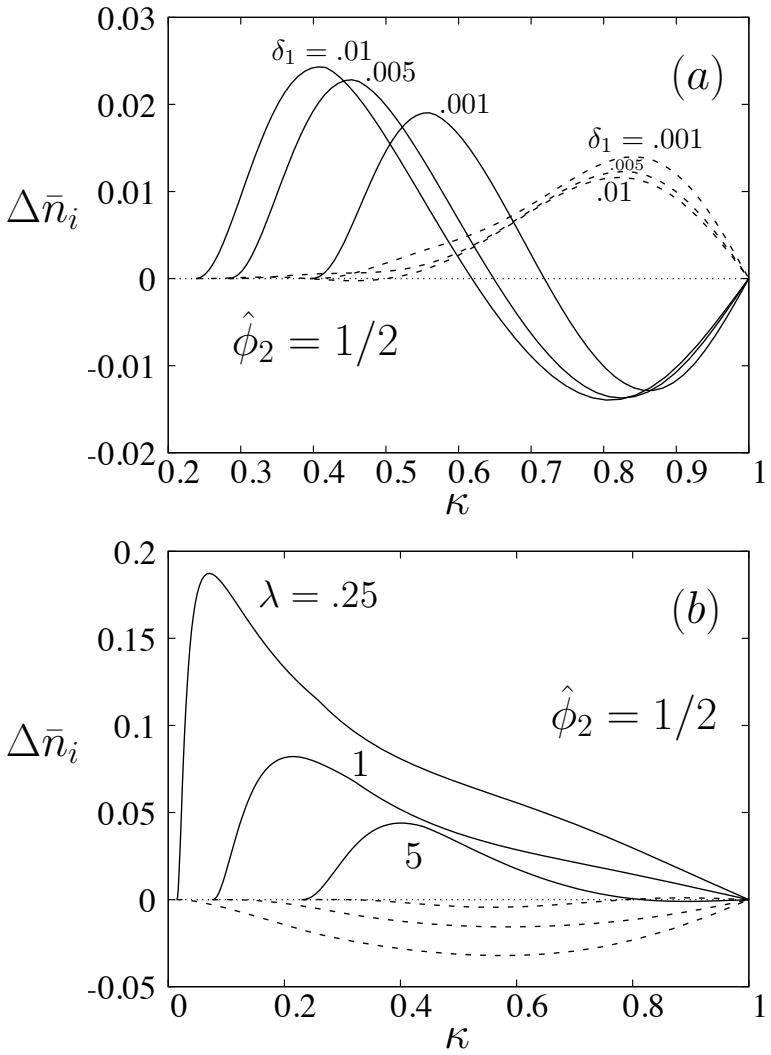

Figure 5.14: Relative enrichment (5.118) for large (dashed lines) and small (solid lines) particles, $\hat{\phi}_2 = 1/2$; (a) particles, roughness $\delta_1 = d/a_1$ as indicated; (b) drops, λ as indicated.

Appendix A

Support material Chapter 2

A.1 Solution of intraparticle pressure in the lubrication region

Here, the normal derivative of the intrapartricle pressure on the boundary of the particle surface is expressed as a boundary integral of the pressure distribution in the near-contact region. Dimensional variables are used. By the disparity of the length scales, $L \ll a$, the intraparticle pressure $\hat{p}(r,z)$ obeys Laplace's equation

$$\nabla^2 \hat{p} = 0 \tag{A.1.1}$$

in a semi-infinite region, vanishes for $z \to -\infty$, and matches the pressure, $p(r)$, in the lubrication gap on the boundary at $z = 0$.

Hankel transformation of Eq. (A.1.1) and boundary conditions yields

$$\frac{d^2\hat{P}}{dz^2} - \omega^2 \hat{P} = 0\,; \qquad \hat{P}(\omega,0) = \int_0^\infty J_0(\omega r) p(r) r dr\,, \qquad \hat{P}(\omega,-\infty) = 0\,, \tag{A.1.2 a, b, c}$$

where $\hat{P}(\omega,z) = \int_0^\infty J_0(\omega r)\hat{p}(r,z) r dr$ is the Hankel-transformed pressure. The solu-

tion of the transformed problem is

$$\hat{P}(\omega, z) = \hat{P}(\omega, 0) e^{\omega z} \,, \tag{A.1.3}$$

where $\hat{P}(\omega, 0)$ is the Hankel-transformed pressure distribution in the gap between the particles (B.1.5b); by the inverse Hankel transform, the intraparticle pressure is given by

$$\hat{p}(r, z) = \int_0^\infty \hat{P}(\omega, 0) e^{\omega z} J_0(\omega r) \omega d\omega \,. \tag{A.1.4}$$

For $-z \gg L$,

$$\hat{p}(r, z) = \frac{F}{2\pi} \frac{z}{\left(r^2 + z^2\right)^{3/2}} \,, \tag{A.1.5}$$

where L is the lateral length scale imposed by the pressure distribution in the near-contact region. The limiting result is obtained using $\hat{P}(\omega, 0) \approx F/(2\pi)$ for $\omega L \ll 1$, where $F = 2\pi \int_0^\infty prdr$ is the lubrication force due to the pressure in the near-contact region.

From Eq. (A.1.4), the normal derivative of pressure on the particle surface is

$$\left.\frac{\partial \hat{p}}{\partial z}\right|_{z=0} = \int_0^\infty \omega^2 \hat{P}(\omega, 0) J_0(\omega r) d\omega \,. \tag{A.1.6}$$

Rewriting this result using the identity

$$-\omega^2 \hat{P}(\omega, 0) = \int_0^\infty \frac{1}{r'} \frac{d}{dr'} \left(r' \frac{dp}{dr'} \right) J_0(\omega r') r' dr' \,, \tag{A.1.7}$$

yields

$$\left.\frac{\partial \hat{p}}{\partial z}\right|_{z=0} = -\int_0^\infty \frac{1}{r'} \frac{d}{dr'} \left(r' \frac{dp}{dr'} \right) \phi\left(r'/r\right) dr' \,, \tag{A.1.8}$$

where

$$\phi\left(r'/r\right) = r' \int_0^\infty J_0(\omega r') J_0(\omega r) \, d\omega \tag{A.1.9}$$

is the Green's function. Rewriting the Bessel function integral in Eq. (A.1.9) yields

$$\phi(x) = \frac{2}{\pi}\,\frac{x}{1+x}\,\mathrm{K}\left(\frac{2\sqrt{x}}{1+x}\right)\,, \tag{A.1.10}$$

where $x = r'/r$, and K is the first-kind elliptic integral,

$$\mathrm{K}(t) = \int_0^{\frac{\pi}{2}} \frac{d\theta}{\sqrt{1-t^2\sin^2\theta}}\,. \tag{A.1.11}$$

Accordingly, the Green's function obeys the reciprocal relation

$$\phi(1/x) = \frac{\phi(x)}{x}\,. \tag{A.1.12}$$

A series expansion of Eq.(B.1.13) for $x \ll 1$ is given by

$$\phi(x) = x + \frac{x^3}{4} + \frac{9x^5}{64} + O(x^7)\,, \tag{A.1.13}$$

and, combining this result with the reciprocal relation (A.1.12), yields

$$\phi(x) = 1 + \frac{1}{4}x^{-2} + \frac{9}{64}x^{-4} + O(x^{-6}) \tag{A.1.14}$$

for $x \gg 1$. At $x = 1$, the Green's function has the following log-singular expansion,

$$\begin{aligned}\phi(x) = &-\frac{1}{\pi}\left[\left(1+\frac{1}{2}(x-1)-\frac{3}{16}(x-1)^2\right)\log\left(\frac{1}{8}|x-1|\right)-\frac{1}{2}(x-1)-\frac{7}{16}(x-1)^2\right]\\ &+O\left[(1-x)^3\log|1-x|\right]+O(1-x)^3\,.\end{aligned} \tag{A.1.15}$$

As a consequence of the intraparticle pressure field obeying Laplace's equation (A.1.1), the integral of the pressure derivative over the surface vanishes, i.e.,

$$\int_0^\infty \left.\frac{\partial\hat{p}}{\partial z}\right|_{z=0} r dr = 0\,. \tag{A.1.16}$$

This result along with Darcy's law (2.24), implies that there is zero net fluid flux into the particles, consistent with the results shown in Fig. 2.3.

A.2 Radial flux with Beavers-Joseph boundary conditions

Here, the radial flux between permeable particles with Beavers-Joseph (Saffman) slip-velocity boundary conditions is calculated, and dimensional variables are used. By conservation of radial momentum the radial velocity is governed by

$$\mu \frac{d^2 v}{dz^2} = \frac{dp}{dr}\,, \tag{A.2.1}$$

and obeys Beavers-Joseph slip-velocity boundary conditions

$$v(0) = \alpha_1 k_1^{1/2} \left.\frac{dv}{dz}\right|_{z=0}\,, \qquad v(h) = -\alpha_2 k_2^{1/2} \left.\frac{dv}{dz}\right|_{z=h}\,, \tag{A.2.2}$$

where k_i and α_i $(i = 1, 2)$ are the permeabilities and slip coefficients for each particle [25, 26].

Solving Eqs. (A.2.1)-(A.2.2) yields

$$v = \frac{1}{2\mu}\frac{dp}{dr} z(z-h) + (v_2 - v_1)\frac{z}{h} + v_1\,, \tag{A.2.3}$$

where v_1 and v_2 are the velocities at $z = 0$ and $z = h$, respectively. Hence,

$$v_1 = -\frac{x_1}{2\mu}\frac{dp}{dr} h^2 \frac{1 + 2x_2}{1 + x_1 + x_2}\,, \qquad v_2 = -\frac{x_2}{2\mu}\frac{dp}{dr} h^2 \frac{1 + 2x_1}{1 + x_1 + x_2}\,, \tag{A.2.4}$$

where $x_i = \alpha_i k_i^{1/2} h^{-1}$ $(i = 1, 2)$. The resulting radial flux is

$$\int_0^h v(z)\, dz = -\frac{1}{12\mu}\frac{dp}{dr} h^3\, g\left(\frac{\alpha_1 k_1^{1/2}}{h}, \frac{\alpha_2 k_2^{1/2}}{h}\right), \tag{A.2.5}$$

and g is a dimensionless function given by Eq. (2.22).

A.3 Far-field pressure distribution

The far-field radial pressure distribution can be obtained from a regular expansion of Eq.(2.19) in powers of $1/\bar{r}$. Inserting the expansion of the Green's function (A.1.13) into the intraparticle flux (2.26) gives

$$\bar{j}[\bar{p}](\bar{r}) = -\frac{1}{\bar{r}}\int_0^\infty \frac{d}{dr'}\left(r'\frac{d\bar{p}}{dr'}\right) dr' - \frac{1}{4\bar{r}^3}\int_0^\infty r'^2 \frac{d}{dr'}\left(r'\frac{d\bar{p}}{dr'}\right) dr' + O(\bar{r}^{-5}). \tag{A.3.1}$$

The first term on the right side vanishes because of the boundary conditions (2.19), and the second term can be integrated by parts to obtain the far-field intraparticle flux (2.46). Inserting Eqs.(2.46) into Eq.(2.19) and integrating, yields the far-field pressure distribution (2.47) for no-slip boundary conditions.

For finite slip on the particle surfaces, the function g must also be expanded for $\bar{r} \gg 1$ recognizing that $x_i = \hat{\alpha}_i q^{-1} \bar{h}^{-1}(\bar{r})$. Expansion of Eq. (2.22) yields

$$g(x) = 1 + 12\, q^{-1} \hat{\alpha}_{\mathrm{m}}\, \bar{r}^{-2} + O(\bar{r}^{-4}), \tag{A.3.2}$$

where $\hat{\alpha}_{\mathrm{m}}$ is the arithmetic mean slip parameter (2.67). Then, inserting this result and Eq. (2.46) into Eq.(2.19) and integrating, yields the modified far-field pressure distribution (2.72).

A similar far-field analysis of Eq.(2.27)-(2.28) leads to the corresponding result in

terms of permeable sphere variables (2.17)

$$\tilde{j}(\tilde{r}) = -3\,\tilde{f}(q,\hat{\alpha}_1,\hat{\alpha}_2)\,\tilde{r}^{-3} + O(\tilde{r}^{-5})\,, \tag{A.3.3}$$

$$\tilde{p} - \tilde{p}^{(0)}(\tilde{r}) = -96\hat{\alpha}_{\rm m}\,\tilde{r}^{-6} - \frac{576}{7}\tilde{f}(q,\hat{\alpha}_1,\hat{\alpha}_2)\,\tilde{r}^{-7} + O(\tilde{r}^{-8})\,. \tag{A.3.4}$$

where $\tilde{p}^{(0)}(\tilde{r})$ is the pressure distribution corresponding to impermeable spheres (2.40) recast in permeable sphere variables.

A.4 Contact Force for Large Slip Limit

Here, the limiting solution for the pressure distribution and force is derived for particles in contact ($q = 0$) with large values of the reduced slip parameter (2.68). Expanding Eq. (2.22) for $x \gg 1$ yields

$$g = 12x + O(1)\,, \tag{A.4.1}$$

where $x = x_1x_2/(x_1+x_2)$. Inserting this result into Eqs. (2.27)-(2.28) yields a differential equation for the leading-order pressure,

$$\frac{1}{\tilde{r}}\frac{d}{d\tilde{r}}\left(\tilde{r}^5\frac{d\tilde{p}}{d\tilde{r}}\right) = -8\hat{\alpha}_{\rm r}^{-1} + O(\hat{\alpha}'^{-2})\,, \tag{A.4.2}$$

where $\hat{\alpha}_{\rm r}$ is the reduced slip parameter (2.68). The solution,

$$\tilde{p} = 2\hat{\alpha}_{\rm r}^{-1}\tilde{r}^{-2} + O(\hat{\alpha}^{-2})\,, \tag{A.4.3}$$

does not satisfy the boundary conditions at $\tilde{r} = 0$ or $\tilde{r} \to \infty$ due to boundary layers that form at $\tilde{r} \sim \hat{\alpha}_{\rm r}^{-1/3}$ where the intraparticle flux balances the flow in the gap, and at $\tilde{r} \sim \hat{\alpha}_{\rm r}^{1/2}$ where the lubrication solution matches to the outer solution

for impermeable particles with slip-velocity boundary conditions. Integrating the leading-order pressure (A.4.3) with the cut-offs resulting from the boundary layers, leads to the resistance formula Eq. (2.77).

A.5 Impermeable spheres with slip-velocity boundary conditions

The axisymmetric lubrication problem for a pair of impermeable spheres with slip-velocity boundary conditions with equal slip coefficients $\alpha_1 = \alpha_2 = \alpha$ is presented here. The first-order lubrication solution, obtained by Hocking (1973) [52] and reproduced below, provides certain limiting behaviors for permeable particles with slip, as discussed in Section 2.4.5. A second-order lubrication solution is available [207] but is not needed because only the leading-order solution is developed in our analysis.

The governing equation for the radial pressure distribution in the gap is

$$-1 = \frac{1}{\bar{r}}\frac{d}{d\bar{r}}\left[\bar{r}\frac{d\bar{p}}{d\bar{r}}\frac{\bar{h}^3}{12}\left(1+\frac{m}{\bar{h}}\right)\right], \qquad \left.\frac{d\bar{p}}{d\bar{r}}\right|_{\bar{r}=0} = 0\,, \quad \lim_{\bar{r}\to\infty}\bar{p}(\bar{r}) = 0\,, \tag{A.5.1}$$

where

$$m = 6\lambda_s/h_0\,, \tag{A.5.2}$$

is the slip parameter, and λ_s is the slip length. The slip length relates the slip-velocity v_s to the tangential stress τ on the particle surfaces, $v_s = \lambda_s\tau/\mu$.

The solution to boundary-value problem (A.5.1) is

$$\bar{p}(\bar{r}, m) = \frac{6}{m}\frac{1}{\bar{h}(\bar{r})} + \frac{6}{m^2}\log\frac{\bar{h}(\bar{r})}{\bar{h}(\bar{r})+m}\,. \tag{A.5.3}$$

Expanding for large $\bar{r}$ yields the far-field pressure,

$$\bar{p}(\bar{r}, m) - \bar{p}^{(0)}(\bar{r}) = -16m\,\bar{r}^{-6} + O(\bar{r}^{-8})\,. \tag{A.5.4}$$

Inserting this pressure distribution into Eq. (2.51a) yields the hydrodynamic resistance

$$\bar{f}(m) = \frac{2}{m^2}\left[(1+m)\log(1+m) - m\right]\,. \tag{A.5.5}$$

For $m \gg 1$, this result yields

$$\bar{f} = \frac{2}{m}(\log m - 1)\,, \tag{A.5.6}$$

indicating that the lubrication force is log-singular at contact, according to Eq. (2.50). Expanding the resistance (A.5.5) for $m \ll 1$, yields

$$\bar{f} = 1 - \frac{m}{3} + \frac{m^2}{6} - \frac{m^3}{10} + O(m^4)\,. \tag{A.5.7}$$

A.5.1 Contact time

Here, the contact time is calculated for impermeable particles with slip-velocity boundary conditions. The contact time is given by Eq. (2.56) with $\bar{t}_\infty$ defined by Eq. (2.58) and

$$\bar{t}_0(m_0) = \int_\infty^{m_0} \frac{\bar{f}(m)}{m}\,dm\,. \tag{A.5.8}$$

Taking

$$\frac{\lambda_s}{a} \ll \frac{h_0}{a} \ll 1 \tag{A.5.9}$$

ensures that $\bar{t}_\infty$ is independent of slip and implies that $m_0 \ll 1$ so that

$$\bar{t}_0(m_0) = \frac{3}{2} - \log m_0 + O(m_0)\,. \tag{A.5.10}$$

Combining this result with Eqs. (2.56), (2.58), and (A.5.2) yields

$$\bar{t}_c = C_\infty - \log 6e^{-\frac{3}{2}} \frac{\lambda_s}{a} \,. \tag{A.5.11}$$

The result indicates that the contact time between impermeable particles with slip-velocity boundary conditions is finite for $\lambda_s > 0$.

Appendix B

Support material Chapter 3

B.1 Derivation of intraparticle flux

In this Appendix, we derive the combined intraparticle flux as a boundary integral of the pressure distribution in the near-contact region. By Darcy's law (3.1), the combined flux is

$$2j = \frac{k_1}{\mu}\frac{\partial p_1}{\partial n} + \frac{k_2}{\mu}\frac{\partial p_2}{\partial n}\,, \tag{B.1.1}$$

where p_1 and p_2 are the intraparticle pressure fields, pressure gradients are evaluated on the particle surfaces, and $\mathbf{n}$ is the outward normal vector. By continuity of pressure across the particle surfaces, the length scale L and angular dependence (3.8) of the pressure distribution in the lubrication gap are imposed on the intraparticle pressure fields. The intraparticle pressure fields satisfy Laplace's equation and, as shown below, decay to zero away from the near-contact region inside the particles on the length scale L. A semi-infinite intraparticle domain can be considered given that $L/a \ll 1$, where a is the reduced radius. Moreover, the intraparticle pressure fields are the same in each particle because they are forced only by the pressure distributions on their surfaces in the near-contact region, which are the same because pressure variations across the gap are negligible according to the leading-order lubrication equations

(3.2). Accordingly, Eq. (B.1.1) simplifies to

$$j = \frac{k}{\mu}\frac{\partial p_i}{\partial n}\,, \tag{B.1.2}$$

where p_i denotes the intraparticle pressure. The result indicates that the total intraparticle flux depends only on the mean permeability (3.37).

According to the foregoing discussion, the intraparticle pressure field has the angular dependence

$$p_i(r,\theta,z) = P_i(r,z)\cos\theta\,, \tag{B.1.3}$$

and satisfies Laplace's equation. Hence, $P_i(r,z)$ satisfies

$$\frac{1}{r}\frac{\partial}{\partial r}\left[\frac{1}{r}\frac{\partial}{\partial r}\left(rP_i\right)\right] + \frac{\partial^2 P_i}{\partial z^2} = 0 \tag{B.1.4}$$

in a semi-infinite region, vanishes for $z \to -\infty$, and matches the pressure, $p(r,\theta)$, in the lubrication gap at $z = 0$.

A first-order Hankel transform of this equation with the prescribed boundary conditions yields

$$\frac{d^2Q_i}{dz^2} - \omega^2 Q_i = 0\,; \qquad Q_i(\omega,0) = \int_0^\infty J_1(\omega r)P(r)r\,dr\,, \qquad Q_i(\omega,-\infty) = 0\,, \tag{B.1.5 a, b, c}$$

where $Q_i(\omega,z) = \int_0^\infty J_1(\omega r)P_i(r,z)r\,dr$ is the Hankel-transformed intraparticle pressure, and $P(r)$ is the pressure in the lubrication gap. The solution of the transformed problem is

$$Q_i(\omega,z) = Q_i(\omega,0)e^{\omega z}\,, \tag{B.1.6}$$

where $Q_i(\omega,0)$ is the Hankel-transformed pressure distribution in the gap between the particles (B.1.5b); by the inverse Hankel transform, the intraparticle pressure is

given by

$$P_i(r,z) = \int_0^\infty Q_i(\omega,0) e^{\omega z} J_1(\omega r)\omega d\omega \,. \tag{B.1.7}$$

For $-z \gg 1$,

$$P_i(r,z) = \frac{3rz\,I}{\left(r^2+z^2\right)^{5/2}}\,, \tag{B.1.8}$$

which is obtained using $P(\omega,0) \approx \omega I$ for $\omega L_0 \ll 1$, where $I = \int_0^\infty Pr^2 dr$. This result confirms the decay of pressure away from the near-contact region.

From Eq. (B.1.7), the normal derivative of pressure on the particle surface is

$$\left.\frac{\partial P_i}{\partial z}\right|_{z=0} = \int_0^\infty \omega^2 Q(\omega,0) J_1(\omega r) d\omega \,. \tag{B.1.9}$$

Rewriting this result using the identity

$$-\omega^2 Q(\omega,0) = \int_0^\infty \frac{1}{r'}\frac{d}{dr'}\left[\frac{1}{r'}\frac{d}{dr'}\left(r'P\right)\right] J_1(\omega r') r' dr' \,, \tag{B.1.10}$$

yields

$$\left.\frac{\partial P_i}{\partial z}\right|_{z=0} = -\int_0^\infty \frac{1}{r'}\frac{d}{dr'}\left[\frac{1}{r'}\frac{d}{dr'}\left(r'P\right)\right] \phi\left(r'/r\right) dr' \,, \tag{B.1.11}$$

where

$$\phi\left(r'/r\right) = r' \int_0^\infty J_1(\omega r') J_1(\omega r)\, d\omega \tag{B.1.12}$$

is the Green's function. Then, rewriting the Bessel function integral in Eq. (B.1.12) yields

$$\phi(x) = \frac{1}{\pi}\left[\frac{1+x^2}{1+x}\mathrm{K}\left(\frac{2\sqrt{x}}{1+x}\right) - (1+x)\mathrm{E}\left(\frac{2\sqrt{x}}{1+x}\right)\right] \,, \tag{B.1.13}$$

where $x = r'/r$, and K and E are elliptic integrals of the first- and second-kind,

$$\mathrm{K}(t) = \int_0^{\frac{\pi}{2}} \frac{d\theta}{\sqrt{1-t^2\sin^2\theta}}\,, \qquad \mathrm{E}(t) = \int_0^{\frac{\pi}{2}} \sqrt{1-t^2\sin^2\theta}\, d\theta \,. \tag{$B.1.14a,b$}$$

Combining Eqs.(B.1.2)-(B.1.3) and (B.1.11) and rescaling the flux according to Eq. (3.38)

yields the intraparticle flux (3.44)

The Green's function is seen to satisfy the reciprocal relation,

$$\phi\left(1/x\right) = \frac{\phi(x)}{x}\,. \tag{B.1.15}$$

A series expansion of Eq.(B.1.13) for $x \ll 1$ yields

$$\phi(x) = \frac{1}{2}x^2 + \frac{3}{16}x^4 + O(x^6)\,. \tag{B.1.16}$$

Combining this result with the reciprocal relation (B.1.15) gives

$$\phi(x) = \frac{1}{2}x^{-1} + \frac{3}{16}x^{-3} + O(x^{-5}) \tag{B.1.17}$$

for $x \gg 1$. The Green's function has the log singular expansion at $x = 1$,

$$\begin{aligned}\phi(x) = &-\frac{1}{\pi}\left[\left(1 + \frac{1}{2}(x-1) + \frac{1}{16}(x-1)^2\right)\log\left(\frac{1}{8}|x-1|\right) + 2 + \frac{1}{2}(x-1) - \frac{3}{16}(x-1)^2\right] \\ &+ O\left[(1-x)^3\log|1-x|\right] + O(1-x)^3\,. \end{aligned}\tag{B.1.18}$$

B.2 Analysis of permeability integral for large and small q

Here, the permeability integral $g(q)$ is analyzed for the limits small and large values of the parameter q.

B.2.1 Small q limit

The Reynolds equation (3.40) is singular for $q \to 0$ (i.e., $h_0 \to 0$) but a solution for $q = 0$ is possible by introducing variables rescaled by a length scale related to the

permeability rather than the gap width. The parameter q can be written as the ratio of length scales,

$$q = (L_0/L_k)^2 \,, \tag{B.2.1}$$

where L_0 is the geometric length scale (3.39), and

$$L_k = K^{1/5} a \tag{B.2.2}$$

is a length scale set by the permeability.

The singularity at $q = 0$ is removed by recasting the problem in terms of dimensionless variables defined using the permeability length L_k,

$$\tilde{r} = \frac{r}{L_k} \,, \quad \tilde{z} = \frac{za}{L_k^2} \,, \quad \tilde{P}^* = \frac{pL_k^3}{\mu U_0 a^2} \,, \quad \tilde{J} = \frac{Ja}{U_0 L_k} \,. \tag{B.2.3}$$

In these variables, Eqs. (3.40)-(3.43) become

$$\frac{1}{12\,\tilde{r}} \left(\tilde{r} \tilde{P}' \, \tilde{h}^3 \right)' - \frac{1}{12\,\tilde{r}^2} \tilde{P} \tilde{h}^3 - 2\tilde{J} = -\frac{\tilde{r}}{2} \,, \qquad \tilde{P}^*(0) = \tilde{P}^*(\infty) = 0 \,, \tag{B.2.4}$$

$$\tilde{h}(\tilde{r}) = q + \frac{1}{2}\tilde{r}^2 \,, \tag{B.2.5}$$

$$g(q) = \int_0^\infty (\tilde{P}_0^* - \tilde{P}^*) r^2 dr \,, \tag{B.2.6}$$

and

$$\tilde{P}_0^*(\tilde{r}) = \frac{6}{5} \frac{\tilde{r}}{\tilde{h}^2} \,. \tag{B.2.7}$$

The permeability-scaled Reynolds equation (B.2.4) has regular perturbation solution for $q \ll 1$,

$$\tilde{P}^*(\tilde{r}, q) = \tilde{p}_0^*(\tilde{r}) + O(q) \,, \tag{B.2.8}$$

where $\tilde{p}_0^*(\tilde{r})$ is the solution with $q = 0$, corresponding to a contact configuration of the

particles. Inserting this expansion into Eq. (B.2.9) yields the leading-order behavior,

$$g(q) = \int_0^\infty (\tilde{P}_0^* - \tilde{p}_0^*) r^2 dr + O(q)\,. \tag{B.2.9}$$

For convenience, this is rewritten as,

$$g(q) = \int_0^1 \tilde{P}_0^* r^2 dr - \int_0^1 \tilde{p}_0^* r^2 dr + \int_1^\infty (\tilde{P}_0^* - \tilde{p}_0^*) r^2 dr + O(q)\,, \tag{B.2.10}$$

to isolate the log-singular behavior resulting from the integration of $\tilde{P}_0^*(\tilde{r})$ at $r = 0$. Formula (3.46) was obtained by a numerical solution of $\tilde{p}_0^*$ and evaluation of integrals in Eq. (B.2.10), except for the coefficient of the $O(q)$ term, c_2, which was obtained by fitting to the solution at finite q.

B.2.2 Large q limit

For $q \gg 1$, the solution of Eq. (3.40) has the form of a regular perturbation,

$$\hat{P}^*(\hat{r}, q) = \hat{P}_0^*(\hat{r}) + q^{-5/2} \hat{P}_1^*(\hat{r}) + O(q^{-5})\,, \tag{B.2.11}$$

where $\hat{P}_0^*(\hat{r})$ is given by Eq. (3.43). At leading-order for large q, the permeability integral (3.42) is given by

$$g(q) = -q^{-5/2} \int_0^\infty \hat{P}_1^* r^2 dr + O(q^{-5})\,, \tag{B.2.12}$$

where the first-order correction field, $\hat{P}_1^*(\hat{r})$, satisfies

$$\frac{1}{12\,\hat{r}} \left(\hat{r} \hat{P}_1^{*\prime} \hat{h}^3 \right)' - \frac{1}{12\,\hat{r}^2} \hat{P}_1^* \hat{h}^3 = 2\, q^{-5/2} \hat{J} \left[\hat{P}_0^* \right], \qquad \hat{P}_1^*(0) = \hat{P}_1^*(\infty) = 0\,. \tag{B.2.13}$$

Formula (3.47) was obtained by a numerical solution of this equation and evaluation of the integral (B.2.12).

B.3 Resistance functions

A brief summary of the equations needed for the full description of the resistance problem is presented in this Appendix. Due to the linearity of the Stokes equations, forces, $\mathbf{F}_\alpha$, torques, $\mathbf{T}_\alpha$, and stresslets, $\mathbf{S}_\alpha$, exerted by a particle $\alpha = 1, 2$ on the surrounding fluid are related to its imposed motion through a resistance matrix [57, 58],

$$\begin{pmatrix} \mathbf{F}_1 \\ \mathbf{F}_2 \\ \mathbf{T}_1 \\ \mathbf{T}_2 \\ \mathbf{S}_1 \\ \mathbf{S}_2 \end{pmatrix} = \mu \begin{pmatrix} \mathbf{A}_{11} & \mathbf{A}_{12} & \widetilde{\mathbf{B}}_{11} & \widetilde{\mathbf{B}}_{12} & \widetilde{\mathbf{G}}_{11} & \widetilde{\mathbf{G}}_{12} \\ \mathbf{A}_{21} & \mathbf{A}_{22} & \widetilde{\mathbf{B}}_{21} & \widetilde{\mathbf{B}}_{22} & \widetilde{\mathbf{G}}_{21} & \widetilde{\mathbf{G}}_{22} \\ \mathbf{B}_{11} & \mathbf{B}_{12} & \mathbf{C}_{11} & \mathbf{C}_{12} & \widetilde{\mathbf{H}}_{11} & \widetilde{\mathbf{H}}_{12} \\ \mathbf{B}_{21} & \mathbf{B}_{12} & \mathbf{C}_{21} & \mathbf{C}_{22} & \widetilde{\mathbf{H}}_{21} & \widetilde{\mathbf{H}}_{22} \\ \mathbf{G}_{11} & \mathbf{G}_{12} & \mathbf{H}_{11} & \mathbf{H}_{12} & \mathbf{M}_{11} & \mathbf{M}_{12} \\ \mathbf{G}_{21} & \mathbf{G}_{22} & \mathbf{H}_{21} & \mathbf{H}_{22} & \mathbf{M}_{21} & \mathbf{M}_{22} \end{pmatrix} \begin{pmatrix} \mathbf{U}_1 - \mathbf{U}_\infty(\mathbf{r_1}) \\ \mathbf{U}_2 - \mathbf{U}_\infty(\mathbf{r_2}) \\ \boldsymbol{\omega}_1 - \boldsymbol{\omega}_\infty \\ \boldsymbol{\omega}_2 - \boldsymbol{\omega}_\infty \\ -\mathbf{E}_\infty \\ -\mathbf{E}_\infty \end{pmatrix}, \tag{B.3.1}$$

where $\mathbf{A}$, $\mathbf{B}$, $\widetilde{\mathbf{B}}$, and $\mathbf{C}$ are second-order tensors; $\mathbf{G}$, $\widetilde{\mathbf{G}}$, $\mathbf{H}$, and $\widetilde{\mathbf{H}}$ are third-order tensors; and $\mathbf{M}$ is a fourth-order tensor that is irrelevant for rigid particles; μ is the fluid viscosity. The spheres have linear and angular velocities $\mathbf{U}_\alpha$ and $\boldsymbol{\omega}_\alpha$, respectively, and are immersed in a linear ambient flow field,

$$\mathbf{U}_\infty(\mathbf{r}) = \mathbf{U}_0 + \mathbf{E}_\infty \cdot \mathbf{r} + \boldsymbol{\omega}_\infty \times \mathbf{r}\,, \tag{B.3.2}$$

where $\mathbf{r}$ is the position vector and the centers of the spheres are at $\mathbf{r}_\alpha$. The quantities $\mathbf{E}_\infty$, $\boldsymbol{\omega}_\infty$, and $\mathbf{U}_0$ are, respectively, the rate-of-strain and vorticity in the fluid, and the velocity at $\mathbf{r} = 0$. The resistance matrix is symmetric and positive definite by the Lorentz reciprocal theorem.

Dimensionless resistance tensors, denoted with a hat, are defined [57, 58]

$$\mathbf{A}_{\alpha\beta} = 3\pi(a_\alpha + a_\beta)\hat{\mathbf{A}}_{\alpha\beta}\,, \tag{$B.3.3a$}$$

$$\mathbf{B}_{\alpha\beta} = \pi(a_\alpha + a_\beta)^2\hat{\mathbf{B}}_{\alpha\beta}\,, \tag{$B.3.3b$}$$

$$\mathbf{C}_{\alpha\beta} = \pi(a_\alpha + a_\beta)^3\hat{\mathbf{C}}_{\alpha\beta}\,, \tag{$B.3.3c$}$$

$$\mathbf{G}_{\alpha\beta} = \pi(a_\alpha + a_\beta)^2\hat{\mathbf{G}}_{\alpha\beta}\,, \tag{$B.3.3d$}$$

$$\mathbf{H}_{\alpha\beta} = \pi(a_\alpha + a_\beta)^3\hat{\mathbf{H}}_{\alpha\beta}\,, \tag{$B.3.3e$}$$

$$\mathbf{M}_{\alpha\beta} = (5/6)\pi(a_\alpha + a_\beta)^3\hat{\mathbf{M}}_{\alpha\beta}\,, \tag{$B.3.3f$}$$

where $\alpha, \beta = 1$ or 2 indicates particle labelling. The tensors obey symmetry relations that are inherent to the geometry of the two-sphere configuration. For spherical particles, the resistance tensors can be decomposed into, at most, two scalar functions $X^R_{\alpha\beta}$ and $Y^R_{\alpha\beta}$ that denote particle resistances parallel and perpendicular to the line-of-centers of the pair. By symmetry, only two resistance functions, i.e. X^R_{11} and X^R_{21} or Y^R_{11} and Y^R_{21}, are needed (cf., [57, Eq.(1.9)] and [58, Eq.(5)]). Here, R refers to one of the resistance tensors.

B.3.1 Transverse resistance functions

The individual resistance functions for impermeable spheres shown in Eq.(3.54) are [11]:

$$Y^{A,0}_{11} = -\frac{1}{12}\frac{(\kappa-1)^2}{\kappa(\kappa+1)}I'_1 - \frac{I'_2}{3} + A^Y_{11}(\kappa)\,, \tag{B.3.4}$$

$$Y^{A,0}_{21} = \frac{1}{6}\frac{(\kappa-1)^2}{\kappa(\kappa+1)}I'_1 + \frac{2}{3(1+\kappa)}I'_2 + A^Y_{21}(\kappa)\,, \tag{B.3.5}$$

$$Y^{B,0}_{11} = \frac{\kappa^{-1}-1}{8}I'_1 + \frac{I'_2}{2} + B^Y_{11}(\kappa)\,, \tag{B.3.6}$$

$$Y_{21}^{B,0} = \frac{\kappa - 1}{2(1+\kappa)^2} I_1' + \frac{2\,\kappa}{(1+\kappa)^2} I_2' + B_{21}^{Y}(\kappa)\,, \tag{B.3.7}$$

$$Y_{11}^{C,0} = -\frac{1+\kappa^{-1}}{16} I_1' - \frac{I_2'}{4} + C_{11}^{Y}(\kappa)\,, \tag{B.3.8}$$

$$Y_{21}^{C,0} = \frac{I_1'}{2(1+\kappa)^2} - \frac{2\kappa}{(1+\kappa)^3} I_2' + C_{21}^{Y}(\kappa)\,, \tag{B.3.9}$$

$$Y_{11}^{G,0} = -\frac{(3\kappa - 1)(\kappa - 1)}{16\kappa(1+\kappa)} I_1' - \frac{I_2'}{4} + G_{11}^{Y}(\kappa)\,, \tag{B.3.10}$$

$$Y_{21}^{G,0} = -\frac{(\kappa - 3)(\kappa - 1)}{4(1+\kappa)^3} I_1' - \frac{\kappa}{(1+\kappa)^2} I_2' + G_{21}^{Y}(\kappa)\,, \tag{B.3.11}$$

$$Y_{11}^{H,0} = \frac{3 - \kappa^{-1}}{32} I_1' - \frac{I_2'}{8} + H_{11}^{Y}(\kappa)\,, \tag{B.3.12}$$

$$Y_{21}^{H,0} = \frac{\kappa - 3}{4(1+\kappa)^3} I_1' - \frac{\kappa}{(1+\kappa)^3} I_2' + H_{21}^{Y}(\kappa)\,, \tag{B.3.13}$$

where

$$I_1' = \frac{24}{5}(1+\kappa^{-1})^{-2} \log \xi^{-1}\,, \qquad I_2' = \frac{2}{1+\kappa^{-1}} \log \xi^{-1}\,, \tag{B.3.14}$$

are obtained from integrals (3.31), absorbing all non-singular terms into the matching constants $R_{\alpha\beta}^{Y}$. These constants depend on size-ratio only and are tabulated in the literature [11]. In this work, we used the code available online and developed by D.J. Jeffrey to generate the matching constants for impermeable spheres with finite size ratio [67] .

B.4 Near-contact axisymmetric mobility functions

In the near-contact regime, the axisymmetric mobility functions L and A are proportional to the G mobility function for permeable spheres (3.63), as indicated by Eq. (3.66). Here, the calculation of the contact forces is described and a table of values is provided.

The contact forces are made dimensionless as

$$\hat{F}_c^{(g)} = \frac{F_c^{(g)}}{6\pi\mu a\, U_{12,g}^{\infty}}\,, \qquad \hat{F}_c^{(E)} = \frac{F_c^{(E)}}{6\pi\mu a\, U_{12,E}^{\infty}}\,, \tag{B.4.1}$$

where $U_{12,g}^{\infty}$ is defined by Eq. (3.61), and

$$U_{12,E}^{\infty} = E\bar{a}\,(1-A)\,, \tag{B.4.2}$$

is the relative velocity along the line-of-centers of two spheres in a extensional flow, where $\bar{a}$ is the average radius and E is the rate-of-strain.

The contact forces are obtained from a force balance on the particles, taking account of the drag forces due to pair migration, gravity forces or forces exerted by the axisymmetric straining flow, and a contact force. The results are [208, 209]

$$\hat{F}_c^{(g)} = \frac{\kappa^{-1}+1}{\kappa^2\gamma - 1}\left[\frac{R_2 - R_1\kappa^3\gamma}{R_1+R_2}\right] \tag{B.4.3}$$

and

$$\hat{F}_c^{(E)} = \frac{1}{\kappa}\frac{R_2^{(E)}R_1 - R_1^{(E)}R_2}{R_1+R_2}\,, \tag{B.4.4}$$

where,

$$R_1 = A_{11}^X(\kappa) + \frac{1+\kappa}{2}A_{12}^X(\kappa)\,, \tag{B.4.5}$$

$$R_2 = \kappa A_{22}^X(\kappa) + \frac{1+\kappa}{2}A_{12}^X(\kappa)\,, \tag{B.4.6}$$

$$R_1^{(E)} = A_{11}^X - \frac{\kappa(1+\kappa)}{2}A_{12}^X - \frac{2}{3}G_{11}^X - \frac{(1+\kappa)^2}{6}G_{21}^X + (1+\kappa^{-1})^{-2}\,, \tag{B.4.7}$$

and

$$R_2^{(E)} = \frac{1+\kappa}{2}A_{12}^X - \kappa^2 A_{22}^X - \frac{(1+\kappa)^2}{6}G_{12}^X + \frac{2}{3}\kappa^2 G_{22}^X - (1+\kappa^{-1})^{-2}\,. \tag{B.4.8}$$

In Eqs.(B.4.5)-(B.4.8), $R^X_{\alpha\beta}$ are matching constants for the axisymmetric resistance functions, $X^A_{\alpha\beta}$ and $X^G_{\alpha\beta}$, obtained from the resistance matrix (B.3.1). Below, a table of values for the contact forces is provided for convenience.

κ	1	.9	.75	.6	.5	.4	.3	.25	.125
$\hat{F}_c^{(g)}$	-	.3862	.3673	.3256	.2825	.2270	.1611	.1260	.04296
$\hat{F}_c^{(E)}$	2.038	2.024	1.933	1.730	1.518	1.238	.8982	.7123	.2538

Table B.1: Contact forces for particles migrating in gravity ($\gamma = 1$) and in axisymmetric straining flow.

Appendix C

Support material Chapter 4

C.1 Asymptotic Evaluation of Collision Efficiency Integrals

In this Appendix, the collision efficiency integrals (4.26b)-(4.29b) are simplified for the case of weakly permeable particles and for particles with small-amplitude surface roughness.

C.1.1 Collision efficiency integrals for weakly permeable particles

The general approach to simplifying the evaluation of the integrals $I_x^{(k)}$ $(x = B, g, st, sh)$ on the contact surface, $s_c = 2$, for weakly permeable particles, $K \ll 1$, is to decompose the efficiency integrals into four parts and perform the near-contact integrations in the gap-width variable ξ,

$$I^{(k)}(s_c) = \int_2^\infty \frac{P(s,q)}{Q(s,q)} ds = I^{(1)} + I^{(2)} + I^{(3)} + I^{(4)}\,, \tag{C.1.1}$$

where the integrals are defined,

$$I^{(1)} = \int_{\xi_2}^{\infty} \frac{P_0(\xi)}{Q_0(\xi)} d\xi \,, \tag{C.1.2}$$

$$I^{(2)} = \int_{\xi_1}^{\xi_2} \frac{P_{\xi,0}(\xi)}{Q_{\xi,0}(\xi)} d\xi \,, \tag{C.1.3}$$

$$I^{(3)} = \int_{\xi_1}^{\xi_2} \left[\frac{P_\xi(\xi, q)}{Q_\xi(\xi, q)} - \frac{P_{\xi,0}(\xi)}{Q_{\xi,0}(\xi)} \right] d\xi \,, \tag{C.1.4}$$

$$I^{(4)} = \int_{0}^{\xi_1} \frac{P_\xi(\xi, q)}{Q_\xi(\xi, q)} d\xi \,. \tag{C.1.5}$$

Here, ξ_1 and ξ_2 satisfy

$$K^{2/5} \ll \xi_2 \ll 1 \,, \qquad \xi_1 = d_1 K^{2/5} \,, \tag{C.1.6}$$

where d_1 is an arbitrary constant. Note that the variable q in integrals $I^{(3)}$ and $I^{(4)}$ is related to the integration variable, ξ, by Eq. (4.30).

The function Q in the above integrals is one of the axisymmetric mobility functions, G, L, or $1 - A$, and P is the non-singular remainder of the collision efficiency integrand, i.e., combinations of the mobility functions as they appear in Eqs. (4.26b)-(4.29b), including factors of s (and the exponential of the van der Waals potential in Eq. (4.26b)). The functions P_0 and Q_0 correspond to the mobility functions for impermeable particles appropriate for $q \gg 1$. The functions P_ξ and Q_ξ are the near-contact, lubrication forms of P and Q, and $P_{\xi,0}$ and $Q_{\xi,0}$ are the near-contact forms of P_0 and Q_0. The integrands for the collision efficiency integrals of impermeable spheres have non-integrable singularities, $Q_{\xi,0} \sim \xi$, at contact, leading to the divergence of the collision efficiency integrals (and vanishing of collision efficiencies) for

impermeable spheres. Accordingly, $\xi_1 > 0$ is required for the integration limits of I_2 and I_3 above.

In the near-contact regime,

$$Q_\xi = R\frac{\xi}{f(q)}\,, \qquad Q_{\xi,0} = R\,\xi\,, \tag{C.1.7a, b}$$

according to Eqs. (4.31) and (4.35), where R is the size-ratio-dependent contact resistance for the axisymmetric mobility function L or $1 - A$; for G, $R = \nu^{-1}$. Here, the function $f(q)$ has asymptotic properties given by Eq. (4.32). The near-contact form P_ξ corresponds to the lubrication approximation of the integrands, obtained from Eqs. (4.31) and (4.33) (and Eq.(4.17) for integral (4.26b)).

Inserting Eq. (C.1.7) into integrals (C.1.3)-(C.1.5) and taking account of the assumed orders of magnitude (C.1.6) yields

$$I^{(2)} = \frac{1}{R}\int_{\xi_1}^{\xi_2} P_{\xi,0}(\xi)\frac{d\xi}{\xi} = F(\xi_2) - F(d_1K^{2/5})\,, \tag{C.1.8}$$

$$I^{(3)} = \frac{1}{R}\int_{d_1\nu^{-1}}^{\infty} \left[P_\xi(\xi,q)f(q) - P_{\xi,0}(\xi)\right]\frac{dq}{q}\,, \tag{C.1.9}$$

$$I^{(4)} = \frac{1}{R}\int_{0}^{d_1\nu^{-1}} P_\xi(\xi,q)f(q)\frac{dq}{q}\,, \tag{C.1.10}$$

where F is the indefinite integral

$$F(x) = \frac{1}{R}\int^{x} P_{\xi,0}(t)\frac{dt}{t}\,. \tag{C.1.11}$$

Combining the above integrals and integral (C.1.2), taking the limit $\xi_2 \to 0$, and

arbitrarily assigning $d_1 = \nu$, yields the desired result,

$$I^{(k)}(s_c) = \Gamma + \Lambda^{(0)} - F(\nu K^{2/5}) \,, \tag{C.1.12}$$

where

$$\Gamma = \lim_{\xi \to 0} \left[I_0(\xi) + F(\xi) \right] \,, \tag{C.1.13}$$

$$\Lambda^{(0)} = \frac{1}{R} \left[\int_1^\infty \left[P_\xi(\xi, q) f(q) - P_{\xi,0}(\xi) \right] \frac{dq}{q} + \int_0^1 P_\xi(\xi, q) f(q) \frac{dq}{q} \right] \,. \tag{C.1.14}$$

Here, the quantity I_0 in Eq. (C.1.13) is the collision efficiency integral for impermeable particles,

$$I_0(\xi) = \int_\xi^\infty \frac{P_0(t)}{Q_0(t)} dt \,. \tag{C.1.15}$$

Recall that ξ and q in the integrand of Eq. (C.1.14) are related by Eq. (4.30).

C.1.2 Collision efficiency integrals for particles with small-amplitude roughness

The corresponding analysis for the evaluation of the integrals integrals $I_x^{(\delta)}$ ($x = B, g, st, sh$) on the contact surface, $s_c = 2 + \nu\delta$, for small-amplitude surface roughness, $\delta \ll 1$, is similar to the foregoing analysis for weakly permeable particles but the situation is simpler because only impermeable sphere mobility functions are required. In this case, the integrals are decomposed into two parts,

$$I^{(\delta)}(s_c) = \int_{\nu\delta}^\infty \frac{P_0(s)}{Q_0(s)} ds = I^{(1)} + I^{(2)} \,, \tag{C.1.16}$$

$$I^{(1)} = I_0(\xi_1)\,, \tag{C.1.17}$$

$$I^{(2)} = \int_{\nu\delta}^{\xi_1} \frac{P_{\xi,0}(\xi)}{Q_{\xi,0}(\xi)} d\xi\,, \tag{C.1.18}$$

where I_0 is the collision efficiency integral for impermable spheres (C.1.15). Inserting Eq. (C.1.7b) into the second integral yields

$$I^{(2)} = \frac{1}{R}\int_{\nu\delta}^{\xi_1} P_{\xi,0}(\xi)\frac{d\xi}{\xi} = F(\xi_1) - F(\nu\delta)\,, \tag{C.1.19}$$

where $F(x)$ is the indefinite integral (C.1.11). Here again, $\xi_1 > 0$ is required to avoid the singularity of $Q_{\xi,0}$ at contact. Rearranging these integrals and taking the limit, $\xi_1 \to 0$ yields the desired result,

$$I^{(\delta)}(s_c) = \Gamma - F(\nu\delta)\,, \tag{C.1.20}$$

where Γ is given by Eq. (C.1.13).

Note that the contact value of the collision efficiency integrals for particles with surface roughness can be derived from the result for permeable particles by the substitution (4.76) in Eq. (C.1.12). This result is justified below.

C.1.3 Evaluation of collision efficiency integral away from contact surface

Results for the evaluation of collision efficiency integrals off the contact surface are provided here. This is required for the evaluation of collision efficiencies in shear flow.

Outside of the near-contact region, the collision efficiency integral is given by the

corresponding integral for impermeable particles (C.1.15),

$$I(\xi) = I_0(\xi)\,, \qquad \xi = O(1)\,. \tag{C.1.21}$$

Two distinct cases arise for the evaluation of collision efficiency integrals in the near-contact region,

$$I(q) = \Gamma + \Lambda(q) - F(\nu K^{2/5})\,, \qquad \xi = O(K^{2/5})\,, \tag{C.1.22}$$

$$I(\xi) = \Gamma - F(\xi)\,, \qquad K^{2/5} \ll \xi \ll 1\,. \tag{C.1.23}$$

Here, $F(x)$ is the integral defined by Eq. (C.1.11), Γ is given by Eq. (C.1.13), and $\Lambda(q)$ is the extension of Eq. (C.1.14) for evaluation off of the contact surface,

$$\Lambda(q) = \frac{1}{R}\left[\int_1^\infty \left[P_\xi(\xi,q')f(q') - P_{\xi,0}(\xi)\right]\frac{dq'}{q'} + \int_q^1 P_\xi(\xi,q')f(q')\frac{dq'}{q'}\right]\,. \tag{C.1.24}$$

Note that Eq. (C.1.23) is actually equivalent to Eq. (C.1.21) according to definition (C.1.13).

The result for evaluation on the contact surface, (C.1.12), is recovered from Eq. (C.1.22) for $q \to 0$ given that Eq. (C.1.24) reduces to Eq. (C.1.14). Equation (C.1.22) reduces to Eq. (C.1.23) for large q, given that

$$\lim_{q\to\infty} \Lambda(q) = F(\nu K^{2/5}) - F(\xi)\,. \tag{C.1.25}$$

Eq. (C.1.23) corresponds to the formula for rough spheres (C.1.20) with roughness $\nu\delta = \xi$. This result justifies Eq. (4.76) because $q \to \infty$ corresponds to $K \to 0$ for $\xi > 0$.

C.1.4 Two indefinite integrals

The two closely-related indefinite integrals, F_g and F_{st}, defined by Eqs. (4.53) and (4.61), and needed, respectively, for calculating collision efficiencies in sedimentation and uniaxial straining flow, are evaluated here. The derivation is similar to that presented in Davis (1984) [90, Eq.(3.6)]. Both integrals have the form,

$$F(x) = \log f(x)\,, \tag{C.1.26}$$

where

$$f(x) = \frac{x^{\alpha_1}}{(\log^2 x^{-1} + d_5 \log x^{-1} + d_4)^{\alpha_2}} \left(\frac{2\log x^{-1} + d_5 - \Delta}{2\log x^{-1} + d_5 + \Delta} \right)^{\alpha_3}\,, \tag{C.1.27}$$

$$\alpha_1 = -\frac{d_3}{2R}\,, \qquad \alpha_2 = \frac{d_3 d_5 - d_2}{4R}\,, \qquad \alpha_3 = \frac{2d_1 - d_2 d_5 + d_3(d_5^2 - 2d_4)}{4R\Delta}\,, \tag{C.1.28}$$

and

$$\Delta = (d_5^2 - 4d_4)^{1/2}\,. \tag{C.1.29}$$

The arbitrary constant associated with the indefinite integral, $F(x)$, indicates that $cf(x)$ can also be used, where c is an arbitrary constant; herein, we take $c = 1$.

For $F_g(x)$, defined by Eq. (4.53),

$$f_g(x) = f(x)\,, \tag{C.1.30}$$

with $f(x)$ defined by (C.1.27)-(C.1.29), coefficients given by $d_i = m_i$ (i = 1-5) in Eq. (4.36a), and $R = R_g$. For F_{st}, defined by Eq. (4.61),

$$f_{st}(x) = x^{1/(2R_{st})} f(x) \tag{C.1.31}$$

with $f(x)$ as defined above, $d_i = b_i$ (i = 1-5) in Eq. (4.36b), and $R = R_{st}$.

C.2 Numerical Evaluation of Collision Efficiency Formulas

Here, we describe the parameters needed to evaluate the collision efficiency formulas derived in Chapter 4 and where to find them.

The size-ratio-dependent parameters R and Γ defined by Eqs. (C.1.7) and (C.1.13), respectively, depend on hard-sphere mobility functions G_0, L_0, M_0, A_0, and B_0. The axisymmetric contact resistances, R, were evaluated using the resistance function code of D.J. Jeffrey [67] by the procedure described in Appendix D of Ref. [116]. The parameters Γ were evaluated using a bispherical coordinate code provided by A.Z. Zinchenko [63, 64]. Values of these parameters for several size ratios are provided in Tables C.1 and C.2 below.

The functions $F(x)$, defined by Eq. (C.1.11) require the size-ratio-dependent coefficients for the near-contact lubrication forms (4.36) of the standard hard-sphere mobility functions $M_{\xi,0}$ and $B_{\xi,0}$ which can be found in a text book [11]. For Brownian motion, $F(x)$ does not require these coefficients.

Collision efficiency formulas for permeable particles also require the functions $f(q)$ and $g(q)$ that enter the lubrication forms (4.31) and (4.33) and the coefficients for M_ξ and B_ξ in Eqs. (4.33a,b). The coefficients are provided in Tables 2-3 of Ref. [116] and tabulations of $f(q)$ and $g(q)$ are provided online [116]. These parameters are needed for the functions $\Lambda^{(0)}$ defined by Eq. (C.1.14).

κ	1	.9	.75	.6	.5	.4	.3	.25	.125
R_g	-	.7745	.7500	.6947	.6357	.5561	.4538	.3939	.2175
R_{st}	4.077	4.059	3.947	3.691	3.415	3.034	2.530	2.226	1.285

Table C.1: Contact forces for particles migrating in gravity ($\gamma = 1$) and in axisymmetric straining flow.

κ	1	.9	.75	.6	.5	.4	.3	.25	.125
$\Gamma_{B,0}$	1.528	1.526	1.513	1.482	1.449	1.403	1.341	1.301	1.156
Γ_g	-	-.080	.0042	.202	.413	.674	.889	.916	.410
Γ_{st}	-.038	-.045	-.086	-.186	-.299	-.446	-.585	-.618	-.359
Γ_{sh}	.6099	.6148	.6462	.7228	.8139	.9551	1.173	1.324	1.917

Table C.2: Coefficients Γ for collision efficiencies of particles in Brownian motion, gravity sedimentation, straining flow and shear flow. Here, Γ_{sh} is obtained with F_{sh} defined by integral (4.70) with $\xi_0 = \nu 10^{-5}$.

Appendix D

Support material Chapter 5

D.1 Derivation of transport coefficients in planar Poiseuille flows

In this section, we present a derivation of the transport coefficients in the velocity gradient direction in regions where the shear-rate vanishes. Inserting the relative particle velocity magnitude (5.28) into the particle flux integral (5.4), and transforming to the cylindrical coordinate system shown in figure 5.1, yields

$$F_{i2}(X_2) = \dot{\gamma}_2' \int_0^{2\pi} \int_0^{r_c} r^{-\infty} |\sin\theta| \left[\int_{-\Delta X_2^{ij}}^{0} n_i(X_2^{i,-\infty}) n_j(r^{-\infty}, \theta, X_2^{i,-\infty}) \right. \\ \left. \left| X_2 + X_2^{i,-\infty} + \frac{1}{2} r^{-\infty} \sin\theta \right| dX_2^{i,-\infty} \right] r^{-\infty} dr^{-\infty} d\theta \,, \tag{D.1.1}$$

where $X_2^{i,-\infty}$ is the distance of particle-i from the plane X_2 where the flux is measured.

The intermediate result, given by Eqs. (5.38)-(5.40), is obtained by splitting the angular θ-integration in Eq. (D.1.1) into two ranges: $0 \leq \theta < \pi$ and $\pi \leq \theta < 2\pi$, then using the symmetry relation (5.5) to consolidate integration to the range $0 \leq \theta < \pi$.

Accordingly, $X_2^{i,-\infty}$ is restricted to the range

$$0 < X_2^{i,-\infty} < -\Delta X_2^{ij} \tag{D.1.2}$$

to ensure that type-i particles cross the X_2 plane, where $-\Delta X_2^{ij} \geq 0$ by the restriction to $0 \leq \theta < \pi$. Linear variations in number density (5.9) are inserted but the complete velocity field is used here, not a linearized approximation, because the latter is inconsistent in the region where the shear-rate vanishes.

In order to we carry out the $X_2^{i,-\infty}$ integration in Eqs. (5.38)-(5.40) and avoid integrating over the absolute values, we exploit the symmetry of the problem about the centerline of the flow, and, without loss of generality, restrict our attention to $X_2 \geq 0$. The second absolute value in each integrand is a positive quantity.

Removing the absolute value of the first term of each integrand in Eqs. (5.38)-(5.39) and the last term of the integrand in Eq. (5.40) requires splitting the range of the $X_2^{i,-\infty}$ integration,

$$0 < X_2^{i,-\infty} < X_2' \,, \quad \text{and} \qquad X_2' < X_2^{i,-\infty} < -\Delta X_2^{ij} \,, \tag{D.1.3}$$

where

$$X_2' = X_2 - \frac{1}{2} r^{-\infty} \sin\theta \tag{D.1.4}$$

with the stipulation

$$0 \leq X_2' \leq -\Delta X_2^{ij} \,, \tag{D.1.5}$$

as required by Eq. (D.1.2). Splitting the $X_2^{i,-\infty}$ integrals accordingly yields

$$\begin{aligned} I_{ij}^{(1)}(X_2) = \frac{1}{X_2} \int_0^{\pi} \int_0^{r_c} r^{-\infty} \sin\theta \Bigg[& \int_0^{X_2'} X_2 X_2^{i,-\infty} dX_2^{i,-\infty} \\ & + \int_{X_2'}^{-\Delta X_2^{ij}} (X_2^{i,-\infty} + \frac{1}{2} r^{-\infty} \sin\theta) X_2^{i,-\infty} dX_2^{i,-\infty} \Bigg] r^{-\infty} dr^{-\infty} d\theta \,. \end{aligned} \tag{D.1.6}$$

$$I_{ij}^{(2)}(X_2) = \frac{1}{X_2}\int_0^{\pi}\int_0^{r_c} r^{-\infty}\sin\theta\left[\int_0^{X_2'} X_2(X_2^{i,-\infty}+r^{-\infty}\sin\theta)dX_2^{i,-\infty} + \int_{X_2'}^{-\Delta X_2^{ij}}(X_2^{i,-\infty}+\frac{1}{2}r^{-\infty}\sin\theta)(X_2^{i,-\infty}+r^{-\infty}\sin\theta)dX_2^{i,-\infty}\right] r^{-\infty}dr^{-\infty}d\theta\,, \tag{D.1.7}$$

$$I_{ij}^{(3)}(X_2) = \int_0^{\pi}\int_0^{r_c} r^{-\infty}\sin\theta\left[\int_0^{X_2'}(X_2^{i,-\infty}+\frac{1}{2}r^{-\infty}\sin\theta)dX_2^{i,-\infty} + \int_{X_2'}^{-\Delta X_2^{ij}} X_2\, dX_2^{i,-\infty}\right] r^{-\infty}dr^{-\infty}d\theta\,. \tag{D.1.8}$$

In this form, the equations can be integrating in $X_2^{i,-\infty}$ to obtain

$$I_{ij}^{(1)}(X_2) = \frac{1}{X_2}\left[\int_0^{\pi}\int_0^{r_c} r^{-\infty}\sin\theta\left[\frac{1}{2}X_2(X_2')^2 - \frac{1}{3}\left((\Delta X_2^{ij})^3+(X_2')^3\right) + \frac{1}{4}r^{-\infty}\sin\theta\left((\Delta X_2^{ij})^2-(X_2')^2\right)\right] r^{-\infty}dr^{-\infty}d\theta\,, \tag{D.1.9}$$

$$I_{ij}^{(2)}(X_2) = \frac{1}{X_2}\left[\int_0^{\pi}\int_0^{r_c} r^{-\infty}\sin\theta\left[(r^{-\infty}\sin\theta)X_2X_2' + \frac{1}{2}X_2(X_2')^2 - \frac{1}{3}\left((\Delta X_2^{ij})^3+(X_2')^3\right) + \frac{3}{4}r^{-\infty}\sin\theta\left((\Delta X_2^{ij})^2-(X_2')^2\right) - \frac{1}{2}(r^{-\infty}\sin\theta)^2\left(\Delta X_2^{ij}+X_2'\right)\right] dr^{-\infty}d\theta\,, \tag{D.1.10}$$

$$I_{ij}^{(3)} = \int_0^{\pi}\int_0^{r_c} r^{-\infty}\sin\theta\left[\frac{1}{2}(X_2')^2 + \frac{1}{2}(r^{-\infty}\sin\theta)X_2' - X_2(\Delta X_2^{ij}+X_2')\right] dr^{-\infty}d\theta\,. \tag{D.1.11}$$

For $X_2 > X_c^{ij}$, $X_2' \to -\Delta X_2^{ij}$, reducing these integrals to their local forms (5.41), and by symmetry with respect to X_2, the same holds also for $X_2 < -X_c^{ij}$. Equation (5.41) is thereby established.

Bibliography

[1] T. W. Secomb. Blood flow in the microcirculation. *Annual Review of Fluid Mechanics*, 49:443–461, 2017.

[2] R. G. Lentle and P. W. M. Janssen. Manipulating digestion with foods designed to change the physical characteristics of digesta. *Critical reviews in food science and nutrition*, 50(2):130–145, 2010.

[3] K. Schroën, J. de Ruiter, and C. C. Berton-Carabin. Microtechnological tools to achieve sustainable food processes, products, and ingredients. *Food Engineering Reviews*, pages 1–20, 2020.

[4] S. Bandyopadhyay, J. R. Peralta-Videa, and J. L. Gardea-Torresdey. Advanced analytical techniques for the measurement of nanomaterials in food and agricultural samples: a review. *Environmental Engineering Science*, 30(3):118–125, 2013.

[5] K. Schroen, A. van Dinther, and R. Stockmann. Particle migration in laminar shear fields: A new basis for large scale separation technology? *Separation and Purification Technology*, 174:372–388, 2017.

[6] M. Elimelech. Predicting collision efficiencies of colloidal particles in porous media. *Water Research*, 26(1):1 – 8, 1992.

[7] P. Le-Clech, V. Chen, and T.A.G. Fane. Fouling in membrane bioreactors used in wastewater treatment. *Journal of Membrane Science*, 284:17–53, 2006.

[8] J. Wang, A. Cahyadi, B. Wu, W. Pee, A. G. Fane, and J. W. Chew. The roles of particles in enhancing membrane filtration: A review. *Journal of Membrane Science*, 595:117570, 2020.

[9] J. Słomka and R. Stocker. Bursts characterize coagulation of rods in a quiescent fluid. *Phys. Rev. Lett.*, 124:258001, Jun 2020.

[10] J. Happel and H. Brenner. *Low Reynolds number hydrodynamics*. Martinus Nijhoff Publishers, 1983.

[11] S. Kim and S. J. Karrila. *Microhydrodynamics: principles and selected applications*. Dover Publications, Inc., 2005.

[12] G. Belfort, R. H. Davis, and A. L. Zydney. The behavior of suspensions and macromolecular solutions in crossflow microfiltration. *Journal of Membrane Science*, 96:1–58, 1994.

[13] F. Civan. *Reservoir Formation Damage*. Elsevier Inc., 2 edition, 2007. Chapter 18.

[14] KJ. Hwang and PY. Sz. Membrane fouling mechanism and concentration effect in cross-flow microfiltration of BSA/dextran mixtures. *Chemical Engineering Journal*, 166:669–677, 2011.

[15] A. E. Rodrigues, B. J. Ahn, and A. Zoulalian. Intraparticle-forced convection effect in catalyst diffusivity measurements and reactor design. *AIChE Journal*, 28(4):541–546, 1982.

[16] R. H. Davis and H. A. Stone. Flow through beds of porous particles. *Chemical Engineering Science*, 48(23):3993 – 4005, 1993.

[17] A. I. Liapis and M. A. McCoy. Perfusion chromatography: Effect of micropore diffusion on column performance in systems utilizing perfusive adsorbent particles with a bidisperse porous structure. *Journal of Chromatography A*, 660(1):85 – 96, 1994. 17th International Symposium on Column Liquid Chromatography.

[18] L.E. Blue and J.W. Jorgenson. 1.1μm superficially porous particles for liquid chromatography: Part ii: Column packing and chromatographic performance. *Journal of Chromatography A*, 1380:71 – 80, 2015.

[19] H. Darcy. *Les Fontaines Publiques de la Ville de Dijon*. Dalmont, 1856.

[20] D. F. James and A. M. J. Davis. Flow at the interface of a model fibrous porous medium. *Journal of Fluid Mechanics*, 426:47–72, 2001.

[21] JL. Auriault. On the domain of validity of Brinkman's equation. *Transport in Porous Media*, 79:215–223, 2009.

[22] D. A. Nield and A. Bejan. *Convection in Porous Media*. Springer, 4 edition, 2013.

[23] I. Gheorghitza. La formule de Stokes pour les enveloppes sphériques poreuses. *Archive for Rational Mechanics and Analysis*, 12:52–57, 1963.

[24] D.D. Joseph and L.N. Tao. The effect of permeability on the slow motion of a porous sphere in a viscous fluid. *Journal of Applied Mathematics and Mechanics*, 44:361–364, 1964.

[25] G. S. Beavers and D. D. Joseph. Boundary conditions at a naturally permeable wall. *Journal of Fluid Mechanics*, 30:197–207, 1967.

[26] P. G. Saffman. On the boundary condition at the surface of a porous medium. *Studies in Applied Mathematics*, 50:93–101, 1971.

[27] G. Neale and W. Nader. Practical significance of Brinkman's extension of Darcy's law: Coupled parallel flows within a channel and a bounding porous medium. *The Canadian Journal of Chemical Engineering*, 52:475–478, 1974.

[28] Y. Cao, M. Gunzburger, F. Hua, and X. Wang. Coupled Stokes-Darcy model with Beavers-Joseph interface boundary condition. *Communications in Mathematical Sciences*, 8:1–25, 2010.

[29] J. A. Ochoa-Tapia and S. Whitaker. Momentum transfer at the boundary between a porous medium and a homogeneous fluid - i. theoretical development. *International Journal of Heat and Mass Transfer*, 38:2635–2646, 1995.

[30] M.L. Bars and M.G. Woster. Interfacial conditions between a pure fluid and a porous medium: implications for binary alloy solidification. *Journal of Fluid Mechanics*, 550:149–173, 2006.

[31] S. L. Goren. The hydrodynamic force resisting the approach of a sphere to a plane permeable wall. *Journal of Colloid and Interface Science*, 69:78–85, 1979.

[32] A. Nir. On the departure of a sphere from contact with a permeable membrane. *Journal of Engineering Mathematics*, 15:65–75, 1981.

[33] G.Z. Ramon and E.M.V. Hoek. On the enhanced drag force induced by permeation through a filtration membrane. *Journal of Membrane Science*, 392-393:1–8, 2012.

[34] A. Debbech, L. Elasmi, and F. Feuillebois. The method of fundamental solution for the creeping flow around a sphere close to a membrane. *ZAMM - Journal of Applied Mathematics and Mechanics / Zeitschrift für Angewandte Mathematik und Mechanik*, 90(12):920–928, 2010.

[35] G.Z. Ramon, H.E. Huppert, J.R. Lister, and H.A. Stone. On the hydrodynamic interaction between a particle and a permeable surface. *Physics of Fluids*, 25:073103, 2013.

[36] S. Khabthani, A. Sellier, and F. Feuillebois. Lubricating motion of a sphere towards a thin porous slab with Saffman slip condition. *Journal of Fluid Mechanics*, 867:949–968, 2019.

[37] J. D. Sherwood. The force on a sphere pulled away from a permeable half-space. *PhysicoChemical Hydrodynamics*, 10:3–12, 1988.

[38] A. C. Michalopoulou, V. N. Burganos, and A. C. Payatakes. Creeping axisymmetric flow around a solid particle near a permeable obstacle. *AIChE Journal*, 38:1213–1228, 1992.

[39] A. M. J. Davis. Axisymmetric flow due to a porous sphere sedimenting towards a solid sphere or a solid wall: Application to scavanging of small particles. *Physics of Fluids*, 13:3126, 2001.

[40] A. C. Payatakes and G. Dassios. Creeping flow around and through a permeable sphere moving with constant velocity towards a solid wall. *Chemical Engineering Communications*, 58:119–138, 1987.

[41] V. N. Burganos, A. C. Michalopoulou, G. Dassios, and A.C. Payatakes. Creeping flow around and through a permeable sphere moving with constant velocity towards a solid wall: a revision. *Chemical Engineering Communications*, 117:85–88, 1992.

[42] R. B. Jones. Hydrodynamic interactions of two permeable spheres i: the method of reflections. *Physica A: Statistical Mechanics and its Applications*, 92:545–556, 1978.

[43] A. C. Michalopoulou, V. N. Burganos, and A. C. Payatakes. Hydrodynamic interactions of two permeable particles moving slowly along their centerline. *Chemical Engineering Science*, 48:2889–2900, 1993.

[44] M.U. Bäbler, J. Sefcik, M. Morbidelli, and J. Baldyga. Hydrodynamic interactions and orthokinetic collisions of porous aggregates in the Stokes regime. *Physics of Fluids*, 18:013302, 2006.

[45] S.B. Chen. Axisymmetric motion of multiple composite spheres: Solid core with permeable shell, under creeping flow conditions. *Physics of Fluids*, 10:1150, 1998.

[46] S. B. Chen and A. Cai. Hydrodynamic interactions and mean settling velocity of porous particles in a dilute suspension. *Journal of Colloid and Interface Science*, 217:328–340, 1999.

[47] G. Barnocky and R. H. Davis. The lubrication force between spherical drops, bubbles and rigid particles in a viscous fluid. *International Journal of Multiphase Flow*, 15:627–638, 1989.

[48] D.J. Knox, B.R. Duffy, S. McKee, and S.K. Wilson. Squeeze-film flow between a curved impermeable bearing and a flat porous bed. *Physics of Fluids*, 29:023101, 2017.

[49] J. R. Smart and D. T. Leighton. Measurement of the hydrodynamic surface roughness of noncolloidal spheres. *Physics of Fluids A: Fluid Dynamics*, 1(1):52–60, 1989.

[50] F. R. Da Cunha and E. J. Hinch. Shear-induced dispersion in a dilute suspension of rough spheres. *Journal of Fluid Mechanics*, 309:211–223, 1996.

[51] J. T. Jenkins and M. A. Koenders. Hydrodynamic interaction of rough spheres. *Granular Matter*, 7:13–18, 2005.

[52] L. M. Hocking. The effect of slip on the motion of a sphere close to a wall and of two adjacent spheres. *Journal of Engineering Mathematics*, 7:207–221, 1973.

[53] M. E. O'Neill and D. S. Bhatt. Slow motion of a solid sphere in the presence of a naturally permeable surface. *The Quarterly Journal of Mechanics and Applied Mathematics*, 44:91–104, 1991.

[54] H.C. Brinkman. A calculation of the viscous force exerted by a flowing fluid on a dense swarm of particles. *Appl. Sci. Res. A*, 1:27–34, 1949.

[55] R. B. Reboucas and M. Loewenberg. Near-contact approach of two permeable spheres. *J. Fluid Mech.*, 2021. in press.

[56] H. Brenner and M. E. O'Neill. On the Stokes resistance of multiparticle systems in a linear shear field. *Chemical Engineering Science*, 27(7):1421–1439, 1972.

[57] D. J. Jeffrey and Y. Onishi. The forces and couples acting on two nearly touching spheres in low-Reynolds-number flow. *Z. angew. Math. Phys.*, 35:634–641, 1988.

[58] D. J. Jeffrey. The calculation of the low reynolds number resistance functions for two unequal spheres. *Physics of Fluids A: Fluid Dynamics*, 4(1):16–29, 1992.

[59] M. E. O'Neill and R. Majumdar. Asymmetrical slow viscous fluid motions caused by the translation or rotation of two spheres. Part ii: Asymptotic forms of the solutions when the minimum clearance between the spheres approaches zero. *Journal of Applied Mathematics and Physics (ZAMP)*, 21:180–187, 1970.

[60] R. M. Corless and D. J. Jeffrey. Stress moments of nearly touching spheres in low Reynolds number flow. *Z. angew. Math. Phys.*, 39:874–884, 1988.

[61] G. K. Batchelor and J. T. Green. The hydrodynamic interaction of two small freely-moving spheres in a linear flow field. *Journal of Fluid Mechanics*, 56(2):375–400, 1972.

[62] G. K. Batchelor. Sedimentation in a dilute polydisperse system of interacting spheres. Part 1. General theory. *Journal of Fluid Mechanics*, 119:379–408, 1982.

[63] A. Z. Zinchenko. personal communication.

[64] M.S. Ingber and A. Zinchenko. Semi-analytic solution of the motion of two spheres in arbitrary shear flow. *International Journal of Multiphase Flow*, 42:152–163, 2012.

[65] A. J. Goldman, R. G. Cox, and H. Brenner. Slow viscous motion of a sphere parallel to a plane wall—i Motion through a quiescent fluid. *Chemical Engineering Science*, 22(4):637–651, 1967.

[66] A. J. Goldman, R. G. Cox, and H. Brenner. Slow viscous motion of a sphere parallel to a plane wall—ii Couette flow. *Chemical Engineering Science*, 22(4):653–660, 1967.

[67] D.J. Jeffrey. Programs for Stokes resistance functions (`https://www.uwo.ca/apmaths/faculty/jeffrey/`).

[68] P. G. Saffman and J. S. Turner. On the collision of drops in turbulent clouds. *Journal of Fluid Mechanics*, 1(1):16–30, 1956.

[69] R. A. Shaw. Particle-turbulence interactions in atmospheric clouds. *Annual Review of Fluid Mechanics*, 35(1):183–227, 2003.

[70] G. A. Jackson. Effect of coagulation on a model planktonic food web. *Deep Sea Research Part I: Oceanographic Research Papers*, 48(1):95 – 123, 2001.

[71] J. Słomka and R. Stocker. On the collision of rods in a quiescent fluid. *Proceedings of the National Academy of Sciences*, 117(7):3372–3374, 2020.

[72] M. V. Smoluchowski. Versuch einer mathematischen theorie der koagulationskinetik kolloider losungen. *Zeitschrift f. Physik. Chemie. XCII*, 92:129–168, 1917.

[73] N. Fuchs. Über die stabilität und aufladung der aerosole. *Z. Physik*, 89:736–743, 1934.

[74] L. A. Spielman. Viscous interactions in Brownian coagulation. *Journal of Colloid and Interface Science*, 33(4):562 – 571, 1970.

[75] I. A. Valioulis and E. J. List. Collision efficiencies of diffusing spherical-particles: hydrodynamic, van der Waals and electrostatic forces. *Adv. Colloid & Interface Sci.*, 20:1–20, 1984.

[76] S. Kim and C. F. Zukoski. A model of growth by heterocoagulation in seeded colloidal dispersions. *J. Colloid & Interface Sci.*, 139:198–212, 1990.

[77] A. S. G. Curtis and L. M. Hocking. Collision efficiency of equal spherical particles in a shear flow. the influence of London-van der Waals forces. *Trans. Faraday Soc.*, 66:1381–1390, 1970.

[78] P. A. Arp and S. G. Mason. Orthokinetic collisions of hard spheres in simple shear flow. *Canadian Journal of Chemistry*, 54(23):3769–3774, 1976.

[79] G. R. Zeichner and W. R. Schowalter. Use of trajectory analysis to study stability of colloidal dispersions in flow fields. *AIChE Journal*, 23(3):243–254, 1977.

[80] T. G. M. van de Ven and S. G. Mason. The microrheology of colloidal dispersions VII. Orthokinetic doublet formation of spheres. *Colloid Polymer Sci*, 255:468–479, 1977.

[81] P. M. Adler. Heterocoagulation in shear flow. *Journal of Colloid and Interface Science*, 83(1):106 – 115, 1981.

[82] M. R. Greene, P. A. Hammer, and W. L. Olbricht. The effect of hydrodynamic flow field on colloidal stability. *Journal of Colloid and Interface Science*, 167(2):232 – 246, 1994.

[83] S. Melis, M. Verduyn, G. Storti, M. Morbidelli, and J. Bałdyga. Effect of fluid motion on the aggregation of small particles subject to interaction forces. *AIChE Journal*, 45(7):1383–1393, 1999.

[84] M. Vanni and G. Baldi. Coagulation efficiency of colloidal particles in shear flow. *Advances in Colloid and Interface Science*, 97(1):151 – 177, 2002.

[85] E. J. Verway and J. Th. Overbeek. *Theory of Stability of Lyophobic Colloids*. Elsevier, 1948.

[86] C. J. Lin, K. J. Lee, and N. F. Sather. Slow motion of two spheres in a shear field. *Journal of Fluid Mechanics*, 43(1):35–47, 1970.

[87] G. K. Batchelor and J. T. Green. The determination of the bulk stress in a suspension of spherical particles to order c2. *Journal of Fluid Mechanics*, 56(2):401–427, 1972.

[88] P. A. Arp and S. G. Mason. The kinetics of flowing dispersions: VIII. Doublets of rigid spheres (theoretical). *Journal of Colloid and Interface Science*, 61(1):21 – 43, 1977.

[89] J. D. Klett and M. H. Davis. Theoretical Collision Efficiencies of Cloud Droplets at Small Reynolds Numbers. *Journal of the Atmospheric Sciences*, 30(1):107–117, 01 1973.

[90] R. H. Davis. The rate of coagulation of a dilute polydisperse system of sedimenting spheres. *Journal of Fluid Mechanics*, 145:179–199, 1984.

[91] D. H. Melik and H. S. Fogler. Gravity-induced flocculation. *Journal of Colloid and Interface Science*, 101(1):72–83, 1984.

[92] M. Han and D. F. Lawler. The (relative) insignificance of g in flocculation. *Journal AWWA*, 84(10):79–91, 1992.

[93] X. Zhang and R. H. Davis. The rate of collisions due to Brownian or gravitational motion of small drops. *Journal of Fluid Mechanics*, 230:479–504, 1991.

[94] A. Z. Zinchenko. Effect of hydrodynamic interactions between the particles on the rheological properties of dilute emulsions. *PMM U.S.S.R.*, 48:282–292, 1984.

[95] H. Wang, A. Z. Zinchenko, and R. H. Davis. The collision rate of small drops in linear flow fields. *Journal of Fluid Mechanics*, 265:161–188, 1994.

[96] M. Loewenberg and R. H. Davis. Flotation rates of fine, spherical particles and droplets. *Chemical Engineering Science*, 49(23):3923 – 3941, 1994.

[97] A. Z. Zinchenko and R. H. Davis. Collision rates of spherical drops or particles in a shear flow at arbitrary Péclet numbers. *Physics of Fluids*, 7(10):2310–2327, 1995.

[98] V. Bal. Stability characteristics of nanoparticles in a laminar linear shear flow in the presence of DLVO and non-DLVO forces. *Langmuir*, 35:11175–11187, 2019.

[99] V. Bal. Coagulation behavior of spherical particles embedded in laminar shear flow in presence of DLVO-and non-DLVO forces. *Journal of Colloid and Interface Science*, 564:170 – 181, 2020.

[100] A. Z. Zinchenko and R. H. Davis. Gravity-induced coalescence of drops at arbitrary péclet numbers. *J. Fluid Mech.*, 280:119–148, 1994.

[101] J. A. Ramirez, A. Z Zinchenko, M. Loewenberg, and R. H. Davis. The flotation rates of fine spherical particles under brownian and convective motion. *Chem. Eng. Sci.*, 54:149–157, 1999.

[102] J. R. Smart, S. Beimfohr, and D. T. Leighton. Measurement of the translational and rotational velocities of a noncolloidal sphere rolling down a smooth inclined place at low reynolds number. *Phys. Fluids A*, 5:13–24, 1993.

[103] I. Rampall, J. R. Smart, and D. T. Leighton. The influence of surface roughness on the particle-pair distribution function of dilute suspensions of non-colloidal spheres in simple shear flow. *J. Fluid Mech.*, 339:1–24, 1997.

[104] D. N. Sutherland. A theoretical model of floc structure. *Journal of Colloid and Interface Science*, 25(3):373 – 380, 1967.

[105] G. Neale, N. Epstein, and W. Nader. Creeping flow relative to permeable spheres. *Chemical Engineering Science*, 28:1865–1874, 1973.

[106] D. N. Sutherland and C. T. Tan. Sedimentation of a porous sphere. *Chemical Engineering Science*, 25(12):1948 – 1950, 1970.

[107] P. M. Adler. Streamlines in and around porous particles. *Journal of Colloid and Interface Science*, 81(2):531 – 535, 1981.

[108] S. Veerapaneni and M. R. Wiesner. Hydrodynamics of fractal aggregates with radially varying permeability. *Journal of Colloid and Interface Science*, 177(1):45 – 57, 1996.

[109] X. Li and B. E. Logan. Collision frequencies of fractal aggregates with small particles by differential sedimentation. *Environ. Sci. Technol.*, 31:1229–1236, 1987.

[110] Xiao-Yan Li and Bruce E. Logan. Permeability of fractal aggregates. *Water Research*, 35(14):3373 – 3380, 2001.

[111] A. Thill, S. Moustier, J. Aziz, M. R. Wiesner, and J.Y. Bottero. Flocs restructuring during aggregation: Experimental evidence and numerical simulation. *Journal of Colloid and Interface Science*, 243(1):171 – 182, 2001.

[112] M. U. Bäbler. A collision efficiency model for flow-induced coagulation of fractal aggregates. *AIChE Journal*, 54(7):1748–1760, 2008.

[113] L. Elasmi and F. Feuillebois. Integral equation method for creeping flow around a solid body near a porous slab. *The Quarterly Journal of Mechanics and Applied Mathematics*, 56:163–185, 2003.

[114] R.H. Davis and A.Z. Zinchenko. Particle collection by permeable drops. *Phys. Rev. Fluids*, 3:113601, Nov 2018.

[115] K. A. Kusters, J. G. Wijers, and D. Thoenes. Aggregation kinetics of small particles in agitated vessels. *Chemical Engineering Science*, 52(1):107 – 121, 1997.

[116] R. B. Reboucas and M. Loewenberg. Resistance and mobility functions for the near-contact of permeable particles. *J. Fluid Mech.*, 2021. in review.

[117] J. Blawzdziewicz, E. Wajnryb, and M. Loewenberg. Hydrodynamic interactions and collision efficiencies of spherical drops covered with an incompressible surfactant film. *Journal of Fluid Mechanics*, 395:29–59, 1999.

[118] H. C. Hamaker. The London-van der waals attraction between spherical particles. *Physica*, 4:1058, 1937.

[119] J. J. Stickel and R. L. Powell. Fluid mechanics and rheology of dense suspensions. *Annu. Rev. Fluid Mech.*, 37:129–149, 2005.

[120] R. G. M. Van der Sman. Simulations of confined suspension flow at multiple length scales. *Soft Matter*, 5(22):4376–4387, 2009.

[121] M. M. Denn and J. F. Morris. Rheology of non-brownian suspensions. *Annual review of chemical and biomolecular engineering*, 5:203–228, 2014.

[122] R. I. Tanner. Aspects of non-colloidal suspension rheology. *Physics of Fluids*, 30(10):101301, 2018.

[123] C. Carotenuto, G. Rexha, R. Martone, and M. Minale. The microstructural change causing the failure of the cox-merz rule in newtonian suspensions: experiments and simulations. *Rheologica Acta*, pages 1–17, 2021.

[124] K. B. Migler. String formation in sheared polymer blends: Coalescence, breakup, and finite size effects. *Phys. Rev. Lett.*, 86:1023–1026, Feb 2001.

[125] L. Elias, F. Fenouillot, JC. Majesté, G. Martin, and P. Cassagnau. Migration of nanosilica particles in polymer blends. *Journal of Polymer Science Part B: Polymer Physics*, 46(18):1976–1983, 2008.

[126] J. L. Colón Quintana, T. Heckner, A. Chrupala, J. Pollock, S. Goris, and T. Osswald. Experimental study of particle migration in polymer processing. *Polymer Composites*, 40(6):2165–2177, 2019.

[127] M. Jabbari, R. Bulatova, A. I. Y. Tok, C. R. H. Bahl, E. Mitsoulis, and J. H. Hattel. Ceramic tape casting: a review of current methods and trends with emphasis on rheological behaviour and flow analysis. *Materials Science and Engineering: B*, 212:39–61, 2016.

[128] A.M.C. Van Dinther, C.G.P.H. Schroën, F.J. Vergeldt, R.G.M. Van der Sman, and R.M. Boom. Suspension flow in microfluidic devices—a review of experimental techniques focussing on concentration and velocity gradients. *Advances in colloid and interface science*, 173:23–34, 2012.

[129] J. B. Dahl, JM. G. Lin, S. J. Muller, and S. Kumar. Microfluidic strategies for understanding the mechanics of cells and cell-mimetic systems. *Annual review of chemical and biomolecular engineering*, 6:293–317, 2015.

[130] S. Singha, A. R. Malipeddi, M. Zurita-Gotor, K. Sarkar, K. Shen, M. Loewenberg, K. B. Migler, and J. Blawzdziewicz. Mechanisms of spontaneous chain formation and subsequent microstructural evolution in shear-driven strongly confined drop monolayers. *Soft matter*, 15(24):4873–4889, 2019.

[131] K. Sarkar and R. K. Singh. Spatial ordering due to hydrodynamic interactions between a pair of colliding drops in a confined shear. *Physics of Fluids*, 25:051702, 2013.

[132] A. C. Barbati, J. Desroches, A. Robisson, and G. H. McKinley. Complex fluids and hydraulic fracturing. *Annual review of chemical and biomolecular engineering*, 7:415–453, 2016.

[133] A. A. Osiptsov. Fluid mechanics of hydraulic fracturing: a review. *Journal of petroleum science and engineering*, 156:513–535, 2017.

[134] R. Fahraeaus and T. Lindqvist. The viscosity of the blood in narrow capillary tubes. *American Journal of Physiology*, 96:562–568, 1931.

[135] J.M. Higgins, D.T. Eddington, S.N. Bhatia, and L. Mahadevan. Sickle cell vasoocclusion and rescue in a microfluidic device. *Proceedings of the National Academy of Sciences*, 104(51):20496–20500, 2007.

[136] M. Diez-Silva, M. Dao, J. Han, CT. Lim, and S. Suresh. Shape and biomechanical characteristics of human red blood cells in health and disease. *MRS bulletin*, 35(5):382–388, 2010.

[137] W. Chien, G. Gompper, and D. A. Fedosov. Effect of cytosol viscosity on the flow behavior of red blood cell suspensions in microvessels. *Microcirculation*, 28(2):e12668, 2021.

[138] A. R. Pries, D. Neuhaus, and P. Gaehtgens. Blood viscosity in tube flow: dependence on diameter and hematocrit. *American Journal of Physiology-Heart and Circulatory Physiology*, 263(6):H1770–H1778, 1992.

[139] A. Tokarev, G. Panasenko, and F. Ataullakhanov. Segregation of flowing blood: mathematical description. *Mathematical modelling of natural phenomena*, 6(5):281–319, 2011.

[140] T. W. Secomb and A. R. Pries. Blood viscosity in microvessels: experiment and theory. *Comptes Rendus Physique*, 14(6):470–478, 2013.

[141] C. Duprat and H. A. Stone. *Low-Reynolds-Number Flows: Fluid Structure Interactions*. Royal Society of Chemistry's series RSC Soft Matter, 2015.

[142] E. Eckstein, D. Bailey, and A. Shapiro. Self-diffusion of particles in shear flow of a suspension. *Journal of Fluid Mechanics*, 79:191–208, 1977.

[143] D. T. Leighton and A. Acrivos. Measurement of shear-induced self-diffusion in concentrated suspensions of spheres. *Journal of Fluid Mechanics*, 177:109–131, 1987.

[144] G. Bossis and J. F. Brady. Self-diffusion of brownian particles in concentrated suspensions under shear. *Journal of Chemical Physics*, 87:5437, 1987.

[145] C. Chang and R. L. Powell. Self-diffusion of bimodal suspensions under shear. *Journal of Fluid Mechanics*, 281:51, 1994.

[146] D. T. Leighton and A. Acrivos. The shear-induced migration of particles in concentrated suspensions. *Journal of Fluid Mechanics*, 181:415–439, 1987.

[147] D. L. Koch. On hydrodynamic diffusion and drift in sheared suspensions. *Phys. Fluids A*, 1:1742–1745, 1989.

[148] F. Gadala-Maria and A. Acrivos. Shear-induced structure in a concentrated suspension of solid spheres. *Journal of Rheology*, 24(6):799–814, 1980.

[149] R. J. Phillips, R. C. Armstrong, R. A. Brown, A. L. Graham, and J. R. Abbott. A constitutive equation for concentrated suspensions that accounts for shear-induced particle migration. *Physics of Fluids A: Fluid Dynamics*, 4:30, 1992.

[150] M. R. King and D. T. Leighton. Measurement of shear-induced dispersion in a dilute suspension. *Physics of Fluids*, 13:397, 2001.

[151] A. Ramachandran, M. Loewenberg, and D. T. Leighton. A constitutive equation for droplet distribution in unidirectional flows for low capillary numbers. *Physics of Fluids*, 22:083301, 2010.

[152] R. B. Reboucas, I. R. Siqueira, P. R. D. Mendes, and M. S. Carvalho. On the pressure-driven flow of suspensions: Particle migration in shear sensitive liquids. *Journal of Non-Newtonian Fluid Mechanics*, 234:178–187, 2016.

[153] P. R. Nott and J. F. Brady. Pressure-driven flow of suspensions: simulation and theory. *Journal of Fluid Mechanics*, 275:157–199, 1994.

[154] J. F. Morris. A review of microstructure in concentrated suspensions and its implications for rheology and bulk flow. *Rheologica acta*, 48(8):909–923, 2009.

[155] J. F. Brady and J. F. Morris. Microstructure of strongly sheared suspensions and its impact on rheology and diffusion. *Journal of Fluid Mechanics*, 348:103–139, 1997.

[156] J. F. Morris and J. F. Brady. Pressure-driven flow of a suspension: buoyancy effects. *International Journal of Multiphase Flow*, 24:105–130, 1998.

[157] A. Sierou and J.F. Brady. Rheology and microstructure in concentrated noncolloidal suspensions. *Journal of Rheology*, 46(5):1031–1056, 2002.

[158] J. F. Morris and F. Boulay. Curvilinear flows of noncolloidal suspensions: The role of normal stresses. *Journal of rheology*, 43(5):1213–1237, 1999.

[159] E. Brown and H. M. Jaeger. Shear thickening in concentrated suspensions: phenomenology, mechanisms and relations to jamming. *Reports on Progress in Physics*, 77(4):046602, 2014.

[160] P. R. Nott, E. Guazzelli, and O. Pouliquen. The suspension balance model revisited. *Physics of Fluids*, 23(4):043304, 2011.

[161] M. Frank, D. Anderson, E. R. Weeks, and J. F. Morris. Particle migration in pressure-driven flow of a brownian suspension. *Journal of Fluid Mechanics*, 493:363–378, 2003.

[162] R. M. Miller and J. F. Morris. Normal stress-driven migration and axial development in pressure-driven flow of concentrated suspensions. *Journal of Fluid Mechanics*, 493:363–378, 2006.

[163] M Mallikarjuna Reddy and Anugrah Singh. Shear-induced particle migration and size segregation in bidisperse suspension flowing through symmetric t-shaped channel. *Physics of Fluids*, 31(5):053305, 2019.

[164] H. M. Vollebregt, R. G. M. Van der Sman, and R. M. Boom. Model for particle migration in bidisperse suspensions by use of effective temperature. *Faraday discussions*, 158(1):89–103, 2012.

[165] P. Kanehl and H. Stark. Hydrodynamic segregation in a bidisperse colloidal suspension in microchannel flow: A theoretical study. *The Journal of chemical physics*, 142(21):214901, 2015.

[166] B. Chun, J. S. Park, H. W. Jung, and YY. Won. Shear-induced particle migration and segregation in non-brownian bidisperse suspensions under planar poiseuille flow. *Journal of Rheology*, 63(3):437–453, 2019.

[167] D. M. Husband, L. A. Mondy, E. Ganani, and A. L. Graham. Direct measurements of shear-induced particle migration in suspensions of bimodal spheres. *Rheologica acta*, 33(3):185–192, 1994.

[168] M. K. Lyon and L. G. Leal. An experimental study of the motion of concentrated suspensions in two-dimensional channel flow. part 2. bidisperse systems. *Journal of Fluid Mechanics*, 363:57–77, 1998.

[169] D. Semwogerere and E. R. Weeks. Shear-induced particle migration in binary colloidal suspensions. *Physics of Fluids*, 20:043306, 2008.

[170] H. Zhao and E. S. G. Shaqfeh. Shear-induced platelet margination in a microchannel. *Physical Review E*, 83:061924, 2011.

[171] M. Zurita-Gotor, J. Bławzdziewicz, and E. Wajnryb. Layering instability in a confined suspension flow. *Physical review letters*, 108(6):068301, 2012.

[172] H. Zhao, E. S. G. Shaqfeh, and V. Narsimhan. Shear-induced particle migration and margination in a cellular suspension. *Physics of Fluids*, 24(1):011902, 2012.

[173] Amit Kumar and Michael D Graham. Margination and segregation in confined flows of blood and other multicomponent suspensions. *Soft Matter*, 8(41):10536–10548, 2012.

[174] A. Kumar and M. D. Graham. Mechanism of margination in confined flows of blood and other multicomponent suspensions. *Physical review letters*, 109(10):108102, 2012.

[175] V. Narsimham, H. Zhao, and E. S. G. Shaqfeh. Coarse-grained theory to predict the concentration distribution of red blood cells in wall-bounded couette flow at zero reynolds number. *Physics of Fluids*, 25:061901, 2013.

[176] A. Kumar, R. G. H. Rivera, and M. D. Graham. Flow-induced segregation in confined multicomponent suspensions: Effects of particle size and rigidity. *Journal of Fluid Mechanics*, 738:423, 2014.

[177] R. G. H. Rivera, X. Zhang, and M. D. Graham. Mechanistic theory of margination and flow-induced segregation in confined multicomponent suspensions: Simple shear and poiseuille flows. *Physical Review Fluids*, 1:060501, 2016.

[178] R. K. Singh and K. Sarkar. Hydrodynamic interactions between pairs of capsules and drops in a simple shear: Effects of viscosity ratio and heterogeneous collision. *Physical Review E*, 92:063029, 2015.

[179] G. J. Tangelder, H. C. Teirlinck, D. W. Slaaf, and R. S. Reneman. Distribution of blood platelets flowing in arterioles. *American Journal of Physiology-Heart and Circulatory Physiology*, 248(3):H318–H323, 1985.

[180] P. A. Aarts, S. A. Van Den Broek, G. W. Prins, G. D. Kuiken, J. J. Sixma, and R. M. Heethaar. Blood platelets are concentrated near the wall and red blood cells, in the center in flowing blood. *Arteriosclerosis: An Official Journal of the American Heart Association, Inc.*, 8(6):819–824, 1988.

[181] T. Omori, T. Ishikawa, Y. Imai, and T. Yamaguchi. Shear-induced diffusion of red blood cells in a semi-dilute suspension. *Journal of Fluid Mechanics*, 724:154–174, 2013.

[182] V. Narsimham, H. Zhao, and E. S. G. Shaqfeh. Coarse-grained theory to predict the concentration distribution of red blood cells in a wall-bounded couetter flow at zero reynolds number. *Physics of Fluids*, 25:061901, 2013.

[183] Q. M. Qi and E. S. G. Shaqfeh. Theory to predict particle migration and margination in the pressure-driven channel flow of blood. *Physical Review Fluids*, 2(9):093102, 2017.

[184] Q. M. Qi and E. S. G. Shaqfeh. Time-dependent particle migration and margination in the pressure-driven channel flow of blood. *Physical Review Fluids*, 3(3):034302, 2018.

[185] C. J. Lin, K. J. Lee, and N. F. Sather. Slow motion of two spheres in a shear field. *Journal of Fluid Mechanics*, 43:35–47, 1970.

[186] G. K. Batchelor and J. T. Green. The hydrodynamic interaction of two small freely-moving spheres in a linear flow field. *Journal of Fluid Mechanics*, 56:375–400, 1972.

[187] A. Z. Zinchenko. Calculation of hydrodynamic interaction between drops at low reynolds numbers. *PMM U.S.S.R.*, 42:955–959, 1978.

[188] A. Z. Zinchenko. The slow asymmetric motion of two drops in a viscous medium. *PMM U.S.S.R.*, 44:49–59, 1980.

[189] F. R. da Cunha and E. J. Hinch. Shear-induced dispersion in a dilute suspension of rough spheres. *Journal of Fluid Mechanics*, 309:211–223, 1996.

[190] M. S. Ingber and A. Z. Zinchenko. Semi-analytic solution of the motion of two spheres in arbitrary shear flow. *International Journal of Multiphase Flow*, 42:152–163, 2012.

[191] R.B. Reboucas and M. Loewenberg. Collision rates of permeable particles in creeping flows. *Phys. Fluids*, 2021. in press.

[192] K. Kremer, M. O. Robbins, and G. S. Grest. Phase diagram of yukawa systems: model for charge-stabilized colloids. *Phys. Rev. Lett.*, 57:2694–2697, 1986.

[193] M. Loewenberg and E. J. Hinch. Collision of two deformable drops in shear flow. *Journal of Fluid Mechanics*, 338:299–315, 1997.

[194] M. Lopez and M. D. Graham. Shear-induced diffusion in dilute suspensions of spherical or nonspherical particles: Effects of irreversibility and symmetry breaking. *Physics of Fluids*, 19:073602, 2007.

[195] E. Lac and D. Barthès-Biesel. Pairwise interaction of capsules in simple shear flow: Three-dimensional effects. *Physics of Fluids*, 20:040801, 2008.

[196] A. R. Malipeddi and K. Sarkar. Shear-induced collective diffusivity down a concentration gradient in a viscous emulsion of drops. *Journal of Fluid Mechanics*, 868:5–25, 2019.

[197] A. R. Malipeddi and K. Sarkar. Collective diffusivity in a sheared viscous emulsion: Effects of viscosity ratio. *Physical Review Fluids*, 4(9):093603, 2019.

[198] I. E. Zarraga and D. T. Leighton. Shear-induced diffusivity on a dilute bidisperse suspension of hard spheres. *Journal of Colloid and Interface Science*, 243:503–514, 2001.

[199] A. Z. Zinchenko. Calculation of the effectiveness of gravitational coagulation of drops with allowance for internal circulation. *PMM U.S.S.R.*, 46:72–82, 1982.

[200] H. Wang, A. Z. Zinchenko, and R. H. Davis. The collision rate of small drops in linear flow fields. *Journal of Fluid Mechanics*, 265:161–188, 1994.

[201] M. B. Nemer, X. Chen, D. H. Papadopoulos, J. Blawzdziewicz, and M. Loewenberg. Comment on "hindered and enhanced coalescence of drops in stokes flows". *Phys. Rev. Lett.*, 92, 2004. Art. 114501.

[202] M.B. Nemer, X. Chen, D.H. Papadopoulos, J. Blawzdziewicz, and M. Loewenberg. Two touching spherical drops in uniaxial extensional flow: analytical solution to the creeping flow problem. *J. Colloid Interface Sci.*, 308:1–3, 2007.

[203] M.B. Nemer, P. Santoro, X. Chen, J. Blawzdziewicz, and M. Loewenberg. Coalescence of drops with mobile interfaces in a quiescent fluid. *J. Fluuid Mech.*, 728:471–500, 2013.

[204] P. A. Arp and S. G. Mason. The kinetics of flowing dispersions. *Journal of Colloid and Interface Science*, 61:44–61, 1977.

[205] Michael A Rother and Robert H Davis. The effect of slight deformation on droplet coalescence in linear flows. *Physics of Fluids*, 13(5):1178–1190, 2001.

[206] S. Reddig and H. Stark. Nonlinear dynamics of spherical particles in poiseuille flow under creeping-flow condition. *The Journal of Chemical Physics*, 138:234902, 2013.

[207] J. Blawzdziewicz, E. Wajnryb, and M. Loewenberg. Hydrodynamic interactions and collision efficiencies of spherical drops covered with an incompressible surfactant film. *Journal of Fluid Mechanics*, 395:29–59, 1999.

[208] M.B.A. Cooley and M.E. O'Neill. On the slow motion of two spheres in contact along their line of centres through a viscous fluid. *Mathematical Proceedings of the Cambridge Philosophical Society*, 66(2):407–415, 1969.

[209] A. Nir and A. Acrivos. On the creeping motion of two arbitrary-sized touching spheres in a linear shear field. *Journal of Fluid Mechanics*, 59(2):209–223, 1973.